The Impact of Stable Water Isotopic Information on Parameter Calibration in a Land Surface Model

by

T.E. Wong

B.A., Ohio Wesleyan University, 2010

M.S., University of Colorado at Boulder, 2012

A thesis submitted to the

Faculty of the Graduate School of the

University of Colorado in partial fulfillment

of the requirements for the degree of

Doctor of Philosophy

Department of Applied Mathematics

2016

This thesis entitled:
The Impact of Stable Water Isotopic Information on
Parameter Calibration in a Land Surface Model
written by T.E. Wong
has been approved for the Department of Applied Mathematics

Assistant Professor William Kleiber

Associate Professor David Noone

Date

The final copy of this thesis has been examined by the signatories, and we find that both the content and the form meet acceptable presentation standards of scholarly work in the above mentioned discipline.

Wong, T.E. (Ph.D., Applied Mathematics)

The Impact of Stable Water Isotopic Information on
Parameter Calibration in a Land Surface Model

Thesis directed by Assistant Professor William Kleiber

The single largest uncertainty in climate model energy balance is the surface latent heating over tropical land. Furthermore, the partitioning of the total latent heat flux into contributions from surface evaporation and plant transpiration offers acute insight into the hydrological and biogeochemical behaviors of an ecosystem, but is notoriously difficult to establish directly. Evapotranspiration (ET) partitioning relies heavily on knowledge of the relative pathways by which water moves from the soil to the atmosphere. These pathways are parameterized by ecosystem resistances, which may not be known with great certainty in practical situations. Resolving these issues requires the development of statistical methods to maximize the use of limited information to best improve models. First, we introduce a commonly-used land surface model, the Community Land Model version 4 (CLM4). We describe an approach to calibrating select model parameters to observational data in a Bayesian estimation framework, requiring Markov chain Monte Carlo sampling of the posterior distribution. We demonstrate the ability of this Bayesian framework to constrain land-atmosphere exchanges of moisture and heat in CLM4, and yield an estimate of ET partitioning which is informed by data. Next, an isotopically-enabled version of CLM4 (iCLM4) is described in detail and validated using site-level and global observations. By leveraging the unique signatures of evaporation and transpiration on the ratios of stable water isotopes, additional constraint on the ET partitioning may be obtained. Finally, an extensive set of isotopic, meteorological and hydrological data from Erie, Colorado, USA is assimilated to calibrate land-atmosphere fluxes and state variables in iCLM4. It is demonstrated that the inclusion of water isotopic data in the assimilation step provides additional constraint on the estimated ET partitioning, and the benefits of these water isotopic datasets relative to common, non-isotopic datasets is quantified.

Acknowledgements

This research is supported by the NSF Paleo Perspectives and Climate Change program (AGS-1203928) and Climate and Large-scale Dynamics (AGS-0955841) as part of the CAREER program. Kleiber's portion was supported by NSF DMS-1417724.

We thank: David Gochis, Andrew Turnipseed and Peter Harley (NCAR), and Max Berkelhammer (U. of Illinois) for assistance in interpreting the meteorological, soil moisture and vegetation data from Manitou Experimental Forest; Aleya Kaushik (CU-Boulder) for assistance in interpreting data from Boulder Atmospheric Observatory.

Contents

Chapter

Tables

Table

Figures

Figure

Chapter 1

Introduction

All physical models and observational data have inherent uncertainty, but are essential tools for the testing of hypotheses using the scientific method [72]. Thus, it is critically important to ensure any model is producing an accurate representation of not only the physical process it is designed to replicate, but also an accurate representation of the uncertainty in the model and data. Statistical science provides a framework in which both of these requirements may be satisfied. In particular, the future climate of Earth depends on the balance and exchange of moisture and heat between the land surface and atmosphere, and climate projections rely heavily on how these are represented in land surface models [37]. As noted in the IPCC Fifth Assessment Report, many improvements in land surface schemes have resulted recently in more detailed descriptions of complex physical processes, but come at the cost of increasing the number of uncertain model parameters [37]. In a model intercomparison study, *Henderson-Sellers et al.* [54] found that their model simulations were sensitive to different hydrological parameterizations, subject to the same surface properties and forcing data. Specifically, the land surface schemes displayed about 70 W m^{-2} variation in the annual cycle surface latent heating over the tropical evergreen forest (Manaus), indicating significant model uncertainty (c.f. [54], their Figures 1 and 2). Therefore, the present study aims to improve the performance of climate models via an evaluation of critical parameters which control the exchange of water and energy between the land and atmosphere.

1.1 ET partitioning

The partitioning of total evapotranspiration (ET) into contributions from surface evaporation (E) and plant transpiration (T) can provide acute insight into the hydrological and biogeochemical coupling and behavior of ecosystems, but is notoriously difficult to constrain. In the climate model energy balance, it has been noted that total ET and precipitation are often unstable or unreliable, and must be treated with great care in model-data comparisons [124]. In the face of these modeling difficulties, there is a pressing need for accurate simulation: a recent global increase in transpiration has been noted, implying that the sensitivity of ET in the hydrological cycle to global change is already perceptible [38]. Several methods exist for ET partitioning, but can be challenging to implement in the field. Total ET is most commonly determined via micrometeorological methods, such as eddy covariance [4]. Transpiration may be determined by chamber gas exchange or sap flow methods, then divided by total ET to obtain the transpiration fraction, f_T. In practice, however, these methods are applied on plant- or plot-level scales, so obtaining results representative of the ecosystem as a whole is limited by surface and vegetation heterogeneity [114, 64, 31]. Soil evaporation can be measured using soil weighing lysimeters, but limitations include difficult implementation and potentially poor spatial representation [30]. Furthermore, estimates of transpiration fraction of total ET for a region may be inconsistent and poorly constrained; for similar sites in the Sonoran desert, estimates of transpiration fraction range from 7 to 80% [113, 90].

Models driven by meteorological fields can simulate latent heat flux and estimate f_T, but depend on parameterizations that are not easily validated or calibrated beyond a small number of idealized cases. Therefore, the difficulty in acquiring direct measurements of f_T places high demand on developing model calibration frameworks through which limited observations may be combined with physical models. ET partitioning quantifies the relative use of the pathways moisture may follow from the soil water to above-canopy water vapor, which is directly related to the surface fluxes. These fluxes, in turn, draw from and contribute to the model state variables, the temperature and moisture content of soil, vegetation and air. The transport of moisture and heat

throughout an ecosystem is commonly modeled analogously to a series of electrical conductors, which encapsulate the efficiency of mass transport between model compartments [103]. In light of the known uncertainty in parameterizations for these resistances, it has been hypothesized that model realizations which best match observations of surface fluxes and state variables are those where the conductance terms (which can be thought inversely as resistances) are correctly modeled [81, 3, 26, 89].

1.2 Stable water isotopes

Stable isotope ratios in water are calculated as the ratio of the molar abundance of the heavy isotopologue (^{18}O and D (^{2}H)) to the more common, lighter, isotopologue (^{16}O and ^{1}H). When a sample of water undergoes a phase change, its isotopic composition changes due to the differing thermodynamic properties of the different isotopologues. Thus, measurements of stable water isotope ratios offer a means to constrain fluxes between ecosystem water pools. Recent years have seen the proliferation of field deployable instruments capable of making measurements of stable water isotope ratios, as well as the wide availability of the computational power necessary to run model simulations of the ecosystems from which measurements originate. This places great importance on developing tools at the interface of these two scientific advances, specifically for the synthesis of measurements of stable water isotopic ratios and isotopically-enabled model simulations. The availability of water isotopic measurements at high temporal resolution provides an opportunity to validate the land surface schemes [45]. These isotope-enabled land surface models are in high demand in order to gain unique insight into hydrological processes and biogeochemical behaviors of ecosystems, and it has been shown that through proper simulation of the below-canopy isotopic exchanges between surface and canopy air-space, better agreement between model and observations may be achieved [1, 119].

Stable water isotope ratios (^{18}O/^{16}O and ^{2}H/^{1}H) offer another method to partition ET by leveraging the unique signatures of evaporation and transpiration on the isotopic makeup of ET source water [133, 141, 131, 98]. In this way, the isotope ratios of water pools within the canopy

structure offer an instantaneous perspective on the balance of ET between E and T [140]. This partitioning approach is becoming more widespread due to the availability of databases of stable water isotopes and field-deployable laser-based isotope spectrometry instruments, but a number of methodological challenges remain. There are inherent uncertainties in obtaining measurements of water isotope ratios as well as in modeling the isotopic E and T flux streams [119, 44], and in a meta-analysis including both isotopic and non-isotopic partitioning approach, *Schlesinger and Jasechko* [115] found that isotope-based partitioning approaches yielded estimates of global average f_T which were higher than estimates from non-isotopic efforts. Furthermore, there is no standard method for obtaining ET partitioning estimates against which isotope-based partitioning may be compared. The same ecosystem resistances which facilitate the exchange of moisture and heat between land surface and atmosphere control the net ecosystem isotopic kinetic fractionation factor [84]. Thus, it is hypothesized that proper modeling of these resistances is critical for robust isotope-based ET partitioning estimates. In the present study, the fidelity with which stable water isotope ratios may be leveraged to partition ET is investigated in a model experimental setting, using model output as synthetic observations. In this way, isotopically-derived partitioning may be compared to directly-modeled partitioning, and any discrepancy may be attributed to simplications in the offline partitioning method relative to the more detailed physics represented in the model.

1.3 Model calibration

While no model is perfect, it has been shown that by utilizing observations of multiple land surface fluxes and at least one state variable, it is possible to achieve better-constrained and physically plausible parameter sets, as well as more realistic model performance [90, 46, 47]. These data assimilation techniques have been successfully applied to land surface models to improve representation of snowmelt processes [105] and the carbon cycle [51, 138], as well as in the hydrological literature to optimize soil moisture parameters in a soil-vegetation-atmosphere-transfer model [25] and improve streamflow predictions and better explore hydrological parameter-spaces [97]. Recently, these model calibration methods have been used to successfully calibrate ecosystem

resistances in a land surface model [135]. In CLM4, it has been shown that modifications to the formulation of stomatal conductance can lead to better agreement in global average ET and gross primary production, further highlighting the network of ecosystem resistances as a strong candidate for the optimization of surface-atmosphere exchanges of heat and moisture [10]. These examples point to statistical calibration as a desirable method for optimizing the exchanges of water and energy between land surface and atmosphere in a model, and thereby also optimize the isotopic exchanges and yield more robust estimates of ET partitioning.

1.4 Guiding hypotheses and anticipated outcomes

There are several challenges in developing assimilation methods for land surface models due to the large number of parameters, many of which are not well-constrained. The addition of a water isotope hydrological scheme adds constraint, from knowledge of the water isotope ratios of the various water pools, but also adds considerable complexity due to additional parameters relevant to the water isotopic physics processes. Furthermore, the physics captured by the model equations is simplified relative to the true processes at all scales, and may not be representative of the behaviors of the larger region. Similarly, there are distinct limitations in quality and availability of data which can be used to constrain land surface schemes (in particular, soil water isotopic data). Therefore, there is a need to test the feasibility of using limited data sets with an efficient and scalable calibration scheme, which is easily generalized to a wide class of physical models. It is also necessary to verify the ability of this algorithm to constrain the uncertainty inherent in adding a water isotope hydrological scheme to a land surface model, through quantification of the value of assimilating water isotopic data into the calibration framework.

In the present study, it will be shown that:

(1) the assimilation of tower meteorological and hydrological data with model output within a Bayesian calibration framework provides constraint on estimates of ecosystem resistances which facilitate the transport of heat and moisture, although the benefits rely on properly

accounting for the various sources of uncertainty in the model and data;

(2) these benefits are increased as a result of assimilating soil water isotopic data and estimates of ET flux water isotope ratios based on data for a single isotopic species;

(3) when a dataset for a second isotopic species is assimilated, the benefits decrease because of the complicated isotopic kinetic effect, but one full constraint is offered by assimilating two isotopic data sets; and

(4) the ability of an isotope-enabled global climate model to simulate isotope ratios which match a network of observations of isotope ratios in ecosystem water pools and fluxes is sensitive to both the specific parameterization of land surface isotopic fractionation effects as well as bulk soil hydrology.

As a consequence of (1), the informed estimates of the network of resistances lead to an estimate of the modeled ET partitioning, and practical estimates of the posterior uncertainties in model parameters as well as transpiration fraction emerge. As a consequence of (2) and (3), the assimilation of two (or more) isotopic species is the optimal set-up to yield robust model-based estimates of isotopic ET partitioning (to fully account for uncertainty in the isotopic kinetic effect). The greatest promise for reconciling discrepancies between isotope-independent and isotope-based estimates of ET partitioning is the sum of (1)-(4): to assimilate into an isotope-enabled land surface scheme soil moisture and isotopic data, and account for uncertainty in the model parameters which influence both the simulated ET partitioning and the water isotopic kinetic fractionation factor.

1.5 Outline

This work develops and tests a framework for constraining ET partitioning estimates using an isotope-enabled land surface model by leveraging land surface and flux data using a Bayesian calibration approach, and is organized in the following way.

Chapter 2 examines the feasibility of synthesizing limited data sets with a land surface model in order to calibrate uncertain model parameters relevant to the ET partitioning in a Bayesian

setting. For the case of a 145 day field campaign at a site in the central Colorado, USA, a statistical approach is used to combine field observations and land surface models to calibrate uncertain model parameters pertaining to the relative pathways by which moisture and heat are exchanged between land and atmosphere. Section 2.2 describes the calibration data set and land surface model. A general statistical calibration framework and adaptive Metropolis-Hastings algorithm are described in Section 2.3.1, and the relevant model and observational uncertainties are reviewed in Section 2.3.2. It is shown in Section 2.4 that accounting for model biases (structural uncertainty) is critical for obtaining robust posterior parameter estimates, and that parametric uncertainty plays a lesser role than representation and observational uncertainties. Finally, Section 2.5 discusses the practical implications of these results for future applications in land surface modeling.

Stable water isotopes provide a well-established observation-based method for partitioning ET, but no comprehensive evaluation of the method has been conducted, largely due to the prohibitive difficulty in determining a baseline ET partitioning measurement against which others may be compared. Thus, the fidelity with which isotope-based partitioning reproduces isotope-independent partitioning estimates must be studied. In particular, this match/mismatch should be studied in a synthetic observations setting, in which the isotope-independent (directly modeled) transpiration fraction of total ET is the known "truth" for the model simulation from which the synthetic observations are derived. Chapter 3 presents a tracer hydrological scheme, incorporated into the National Center for Atmospheric Research's Community Land Model, Version 4 (CLM4) [103], and examines the shortcomings and strengths of the modeling framework relative to site-level and global networks of water isotopic data. CLM4 is the land surface component of the Community Earth System Model (CESM) [59], which is one of the models considered by the Intergovernmental Panel on Climate Change (IPCC) [37]. The tracer-enabled version of CLM4, iCLM4, closely parallels the native hydrology in CLM4, with several critical additions which enable the modeling of hydrological tracers. These tracers may be temporal (such as tracing summer rainfall through the hydrological cycle), spatial (such as tracing rain reevaporation from the Amazon rainforest), or isotopic (tracing heavy isotopologues of water). The focus of the present work is

on the latter. Chapter 3 is organized as follows. Section 3.2 provides a technical review of the isotope tracer model. Section 3.3 outlines the datasets used for validation of the model results, and Section 3.3.2 details global sensitivity experiments conducted by coupling the isotopic land surface scheme reviewed in the present work with the complementary stable water isotope-enabled atmospheric model. A review of the practical implications of these results and future work is given in Section 3.4.

Chapter 4 presents model calibration results for the case of a 4-year (ongoing) field campaign at a site in central Colorado, USA, and examines the fidelity with which synthetic observations of water isotopic data yields isotope-based ET partitioning estimates which reproduce isotope-independent partitioning (the "truth" for the model simulation from which the synthetic observations are derived). The statistical approach of Chapter 2 is used to combine field observations and an isotopically-enabled land surface model (Chapter 3) to calibrate uncertain model parameters pertaining to the relative pathways by which moisture and heat are exchanged between land and atmosphere. These same parameters control the net ecosystem isotopic kinetic fractionation factor. Experiments are performed to quantify the benefits of calibrating using no isotopic information, as well as adding one or two datasets of stable water isotopic information to the calibration. Section 4.2 describes the calibration data set and stable water isotopically-enabled land surface model. A general statistical calibration framework and adaptive Metropolis-Hastings algorithm are described in Section 4.3.1, and the relevant model and observational uncertainties are reviewed in Section 4.3.2. It is shown in Section 4.4 that calibrating using no water isotopic information is good, calibrating using a single isotopic species is better, but calibrating using two isotopic species is worse. Finally, Section 4.5 discusses the practical implications of these results for future applications in partitioning ecosystem fluxes using water isotopic information.

Chapter 2

Bayesian Error Attribution for Alpine Forest Turbulent Fluxes

2.1 Introduction

The partitioning of total evapotranspiration (ET) into contributions from surface evaporation and plant transpiration provides acute insight into the hydrological and biogeochemical coupling and behavior of ecosystems, but is notoriously difficult to constrain. Several methods exist for ET partitioning, but can be challenging to implement in the field. Total ET is most commonly determined via micrometeorological methods, such as eddy covariance [4]. Transpiration may be determined by chamber gas exchange or sap flow methods, then divided by total ET to obtain the transpiration fraction, f_T. In practice, however, these methods are applied on plant- or plot-level scales, so obtaining results representative of the ecosystem as a whole is limited by surface and vegetation heterogeneity [114, 64, 31]. Soil evaporation can be measured using soil weighing lysimeters, but limitations include difficult implementation and potentially poor spatial representation [30]. Furthermore, estimates of transpiration fraction of total ET for a region may be inconsistent and poorly constrained; for similar sites in the Sonoran desert, estimates of transpiration fraction range from 7 to 80% [113, 90].

Models driven by meteorological fields can simulate latent heat flux and estimate f_T, but depend on parameterizations that are not easily validated or calibrated beyond a small number of idealized cases. Therefore, the difficulty in acquiring direct measurements of f_T places high demand on developing model calibration frameworks through which limited observations may be combined with physical models. ET partitioning quantifies the relative use of the pathways moisture may

follow from the soil water to above-canopy water vapor, which is directly related to the surface fluxes. These, in turn, draw from and contribute to the model state variables, the temperature and water content of soil, vegetation and air. The transport of moisture and heat throughout an ecosystem is commonly modeled as a series of electrical resistors [103]. In light of the known uncertainty in parameterizations for these resistances, it is hypothesized that model realizations which best match observations of surface fluxes and state variables are those where the resistance terms are correctly modeled [81, 3, 26, 89].

Although no model is perfect, it has been shown that by utilizing observations of multiple land surface fluxes and at least one state variable, it is possible to achieve better-constrained and physically plausible parameter sets, as well as more reasonable model performance [90, 46, 47]. These data assimilation techniques have been successfully applied to land surface models to improve representation of snowmelt processes [105] and the carbon cycle [51, 138], as well as in the hydrological literature to optimize soil moisture parameters in a soil-vegetation-atmosphere-transfer model [25] and improve streamflow predictions and better explore hydrological parameter-spaces [97]. These examples point to statistical calibration as a desirable method for optimizing the exchanges of water and energy between land surface and atmosphere in a model.

There are several challenges in developing assimilation methods for land surface models due to the large number of parameters, and many of these parameters are not well-constrained. Furthermore, the physics captured by the model equations is simplified relative to the true processes at all scales, and may not be representative of the behaviors of the larger region. Similarly, there are distinct limitations in quality and availability of data which can be used to constrain land surface schemes. As detailed in the IPCC Fourth Assessment Report, there is a notable lack of data which may be used to validate the land surface component of global models [107]. Therefore, there is a need to test the feasibility of using limited data sets with an efficient and scalable calibration scheme, which is easily generalized to a wide class of physical models. In the present study, it is shown that (1) the assimilation of tower meteorological data with model output within a Bayesian calibration framework provides constraint on the network of ecosystem resistances to

moisture and heat transport, and (2) the efficacy of the calibration approach relies on properly accounting for uncertainties in both the model and observations. As a consequence of (1), the informed estimates of the network of resistances lead to an estimate of the modeled ET partitioning, and practical estimates of the posterior uncertainties in model parameters as well as transpiration fraction emerge.

For the case of a 145 day field campaign at a site in the central Colorado, USA, we propose a statistical approach to combine field observations and land surface models to calibrate uncertain model parameters pertaining to the relative pathways by which moisture and heat are exchanged between land and atmosphere. Section 2.2 describes the calibration data set and land surface model. A general statistical calibration framework and adaptive Metropolis-Hastings algorithm are described in Section 2.3.1, and the relevant model and observational uncertainties are reviewed in Section 2.3.2. It is shown in Section 2.4 that accounting for model biases (structural uncertainty) is critical for obtaining robust posterior parameter estimates, and that parametric uncertainty plays a lesser role than representation and observational uncertainties. Finally, Section 2.5 discusses the practical implications of these results for future applications in land surface modeling. [95, 53, 49, 55].

2.2 Model and observational data

2.2.1 Observational data

The observational data consist of meteorological and hydrological data spanning 145 days from May to September 2011 in an alpine forest northwest of Colorado Springs, Colorado, USA. Measurements were made from a 27.1 m tall tower in the Manitou Experimental Forest (MEF, 39°06′02″ N, 105°06′05″ W, 2286 m elevation). This is a Ponderosa Pine forest with minimal undergrowth, a canopy height of roughly 18.5 m, and leaf area index (LAI) of 1.9 [104, 28, 74]. The MEF site was selected for this study due to the availability of high quality previously validated hydrological and flux data.

Air temperature (°C), humidity (%), and pressure (mbar) were measured by a series of Vaisala HMT337 and WXT520 probes located at each inlet. CO_2 and humidity concentrations (μmol mol^{-1} and mmol mol^{-1}, respectively) were measured using a LiCor Li6262. Wind speed (m s^{-1}) was measured using a Gill® R3-50 Sonic Anemometer. CO_2 and H_2O fluxes (μmol m^{-2} s^{-1} and mmol m^{-2} s^{-1}, respectively) were measured using a LiCor Li7000 infrared gas analyzer and Campbell CSAT-3 sonic anemometer. Eddy covariance methods were used to determine latent and sensible heat fluxes (W m^{-2}). A suite of Kipp and Zonen CNR1 radiometers were used to measure upward and downward longwave and shortwave radiation (W m^{-2}). Observations of soil temperature (K) were made at depths of 5, 50, 70, 100 and 150 cm using Campbell Scientific T107 thermistors. Further information regarding the experimental set-up can be found in [8], [28] and [104].

2.2.2 Land surface model

The model used is the National Center for Atmospheric Research Community Land Model 4.0 (CLM4) [103]. CLM4 is a one-dimensional land surface model of the energy, momentum, water, and CO_2 exchanges between land and atmosphere, and it accounts for ecosystem dynamics, biophysical processes, hydrological processes, and biogeochemical processes. The Community Land Model is the land component of the Community Earth System Model (CESM) [59], which is one of the models utilized by the Intergovernmental Panel on Climate Change (IPCC) [37]. The IPCC has

Data fields needed as inputs to force CLM4 include incident solar and longwave radiation, incident precipitation, atmospheric humidity, wind speed, and pressure and temperature at the surface. Surface data configured for MEF are soil texture, soil color, monthly leaf area index (LAI) and stem area index (SAI), vegetation composition, and albedo [128]. Previous studies suggest that using land surface fluxes and at least one state variable, it is possible to achieve better-constrained and physically plausible parameter sets, as well as more physically reasonable model performance [90, 46, 47]. Following this example, data used for the calibration included daily averages of latent heat flux, sensible heat flux, and top soil layer temperature. Latent and sensible heat flux are key

quantities in the exchange of moisture and heat between the land surface and atmosphere, and are readily observable by eddy covariance techniques [4]. Soil temperature is a widely observed state variable, and characterizes the energy state of the ecosystem, offering an attractive option to calibrate against. It should be noted that the top soil layer temperature is distinct from the radiative temperature of the soil surface. Soil moisture content data are available and could also serve as calibration data, but are not used in the assimilation since an objective of the calibration technique is to improve simulation of soil water by better constraining the fluxes. The focus of this study is to evaluate the importance of the uncertainties inherent in physical models and observations, and serve as a demonstrative example constraining model parameters in light of these uncertainties.

To account for uncertainty in ecosystem turbulence characteristics, parameters selected for calibration are the aerodynamic resistances to moisture and heat transport between surface and vegetation air (f_g), and between vegetation and above-canopy air (f_a), through vegetation stomata (f_s), and through the leaf boundary layer (f_b). The calibration parameters are applied as multiplicative factors in the default resistance parameterizations. Stomatal resistance (m^2 s μmol) is calculated as

$$r_s = f_s \left(m \frac{A}{c_s} \frac{e_s}{e_i} P_{atm} + b \right)^{-1}, \tag{2.1}$$

where m is a parameter which depends on vegetation type, A is leaf photosynthesis (μmol CO_2 m^{-2} s^{-1}), c_s is the CO_2 partial pressure at the leaf surface (Pa), e_s is the vapor pressure at the leaf surface (Pa), e_i is the saturation vapor pressure (Pa) inside the leaf at the temperature of the vegetation, P_{atm} is the atmospheric pressure (Pa), and $b = 2000$ is the minimum stomatal conductance (μmol m^{-2} s^{-1}) when $A = 0$ [23, 103]. While the factors A, c_s, e_s and e_i are all modeled by CLM4, P_{atm} is given as atmospheric forcing and m and b are parameters which depend on vegetation type, and all have associated uncertainties. m and b, in particular, are known from laboratory experiments for various leaf types [5], though it remains less clear how these parameters scale up to the ecosystem scale considered by CLM4. From [23], Figure 2, it can be seen that the overall match is reasonable between measured and modeled stomatal conductance (the inverse of

r_s), but parametric uncertainty in Equation 2.1 persists at the leaf scale, which will aggregate when integrated to ecosystem scale.

Leaf boundary layer resistance (m^2 s μmol) is parameterized as

$$r_b = f_b \frac{1}{C_v} \left(U/d_{leaf}\right)^{-1/2}, \tag{2.2}$$

where $C_v = 0.01$ m $s^{-1/2}$ is the turbulent transfer coefficient between the vegetation surface and canopy air, U (m s^{-1}) is the magnitude of the wind velocity incident on the leaves at a reference level, and d_{leaf} is the characteristic dimension of the leaves in the direction of the wind flow (taken throughout CLM4 to be 0.04 m) [103]. U is modeled by CLM4 and C_v and d_{leaf} are parameters which CLM4 prescribes to all vegetation types, thus it is likely they do not describe any specific plant form particularly well, including those present at MEF.

The aerodynamic resistance to moisture and heat transfer between ground and canopy air (s m^{-1}) is as follows:

$$r_g = f_g \frac{1}{C_s U}, \tag{2.3}$$

where C_s is the turbulent transfer coefficient between the underlying soil and the canopy air, which is interpolated between values for bare soil and for dense canopy [143, 103]. While the formulations from [143] agree with observational data, these authors note that there are few measurements available which can constrain these values.

The aerodynamic resistance between the vegetation canopy and above-canopy air-spaces (s m^{-1}) is given by

$$r_a = f_a \frac{q_{atm} - q_s}{q_* u_*}, \tag{2.4}$$

where u_* (m s^{-1}) is the friction velocity, q_* (kg kg^{-1}) is the moisture scale, q_{atm} (kg kg^{-1}) is the atmospheric specific humidity, and q_s (kg kg^{-1}) is the surface specific humidity [103]. u_* and q_* are derived from Monin-Obukhov similarity theory, and as noted by [144], their parameterizations were developed by separate groups using different data in different parameter regimes, and are intended for global modeling studies, with typical grid spacing much larger than the extent of the MEF tower

footprint. Therefore it is not expected that these gridcell-scale parameters will compare favorably with the site-level data at MEF, further suggesting some tuning or calibration should be done.

These resistances are exchange parameters which define the way in which the energy and water balances at the surface behave, yet the theory behind them is not well-established. [89] showed that realistic errors in the wind speed used to determine the aerodynamic resistances can lead to errors as large as 22% in modeled surface fluxes. Therefore, estimating these parameters is important to accurately model the transfer processes. Simulation using calibrated parameters led to CLM4 simulations which more closely match observations of latent heat flux, sensible heat flux and top soil layer temperature, as measured by the root-mean-squared error (RMSE). This parameter set therefore provides an illustrative demonstration of the benefits of this calibration approach. f_T is a quantity which characterizes the hydrological and biogeochemical behaviors of an ecosystem, and the resistance parameters selected here partly control the balance of two critical moisture fluxes, evaporation and transpiration, in the model. Therefore, the effects of the calibration on the modeled seasonal average transpiration fraction are analyzed.

2.2.3 Model biases and the need for a statistical approach

Figure 2.1 compares CLM4 output for latent heat flux, sensible heat flux, and top soil layer temperature to observational data, averaged on a daily time scale, as well as histograms of the errors. The gray shaded regions denote a ± 1 observational standard error region around the observations. The model represents these physical processes qualitatively well, as peaks and troughs in the data are present in the modeled values. However, the error histograms are not centered at zero, indicative of model bias: distributions of latent and sensible heat flux errors are centered around -25 W m^{-2} and top soil temperature errors are centered around -4.4 K. The low flux bias at MEF is consistent with the generally low bias found in northern mid-latitude sites in a global analysis [11]. It is unclear that these biases are attributable to model parameter choice, or are an inherent limitation of CLM4 that stems from the use of approximate equations, thus motivating the need to account for these model biases. RMSE for the uncalibrated modeled latent heat flux, sensible heat flux,

and soil temperature are 27 W m^{-2}, 36 W m^{-2}, and 4.4 K, respectively.

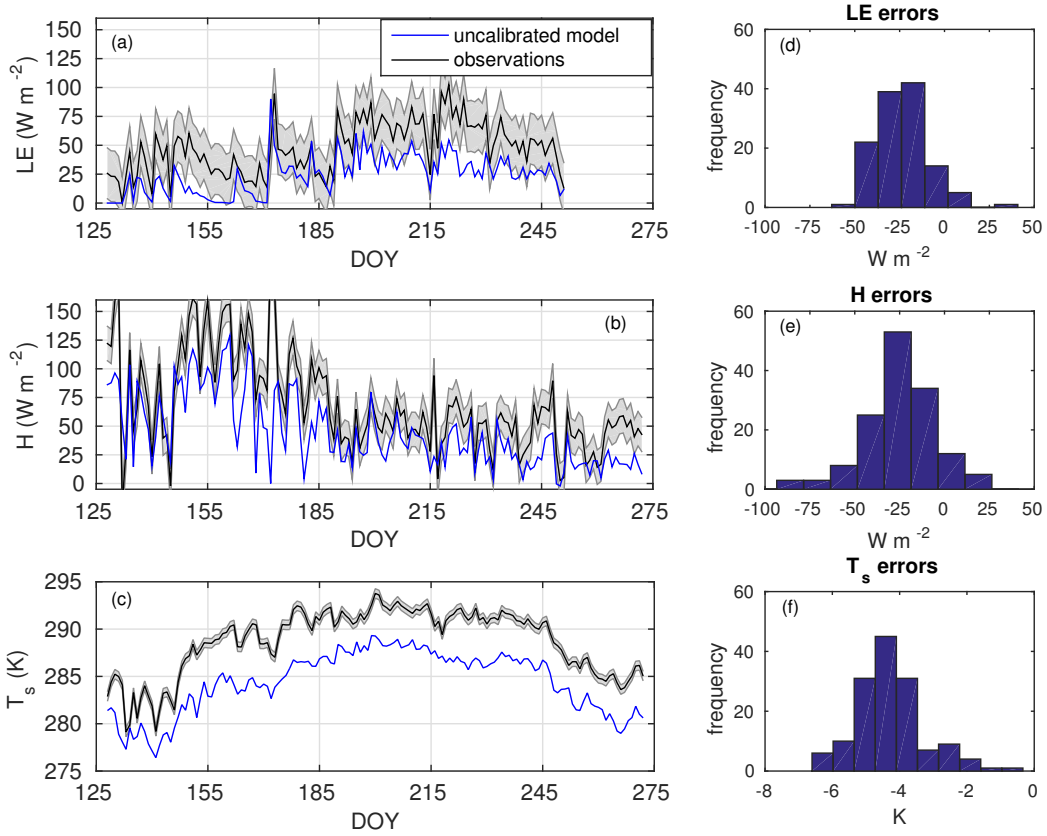

Figure 2.1: Uncalibrated model results, compared to observational data. Left: Time series of (a) latent heat flux, (b) sensible heat flux, and (c) top soil layer temperature. Right: Histograms of the errors in these quantities, reported as *model* − *observations*. The gray shaded region denotes ±1 observational standard error around the observations.

2.3 Calibration framework

2.3.1 Model calibration

Within a statistical framework, the CLM4 model output is related to various types of observational data. Using a Bayesian approach, prior distributions on the model parameters are joined with the CLM4 solution and assimilated field data, leading to posterior distributions that represent

uncertainty in both the model and the statistical parameters. The calibration algorithm proceeds by seeking to maximize the likelihood that the model simulation results match the observational data in light of the model biases and other errors.

Let $\eta(t, \theta) \in \mathbb{R}^3$ refer to the vector of model output for the calibration fields (latent heat flux, sensible heat flux, and top soil temperature) at calibration parameter values $\theta = (f_g, f_s, f_a, f_b)^T$ on day t and let $y(t) \in \mathbb{R}^3$ be the corresponding observations of these fields. Let $\alpha = (\alpha_{LE}, \alpha_H, \alpha_T)^T$ refer to the model additive bias, where α_{LE} is the additive bias in the modeled latent heat flux, α_H is the bias in the sensible heat flux, α_T is the temperature bias, and the simplifying assumption $\alpha_F = \alpha_{LE} = \alpha_H$ is made. In preliminary experiments, the biases in the sensible and latent heat fluxes were similar enough to warrant this assumption, and thereby reduce the size of the parameter-space the calibration approach must explore. α_F is a bias assumed to be present in both the modeled latent and sensible heat fluxes. The bias corrections α_F and α_T may be considered as accounting for model structural error. Finally, denote the optimal, unknown, model parameters by θ^* and let α^* be the additive model bias which optimizes the match between modeled and observed fluxes and soil temperature. The statistical model is

$$y(t) = \alpha^* + \eta(t, \theta^*) + \epsilon(t). \tag{2.5}$$

It is simple to generalize (2.5) to include a multiplicative bias term as well, but based on exploratory analyses such flexibility is neither required nor considered in the present application. For the sake of brevity, throughout the remainder of this paper the term "bias" refers only to the additive bias, α.

It is convenient to think of $\zeta(t) = \alpha^* + \eta(t, \theta^*)$ as representing the physical process the model η seeks to capture. In (2.5), $\epsilon(t) \in \mathbb{R}^3$ accounts for model and observational errors and is modeled as a multivariate mean zero Gaussian process that is independent between components and across time points. Denote by Σ the covariance matrix of $\epsilon(t)$. It is assumed $\Sigma = \text{diag}(\sigma_1^2, \sigma_2^2, \sigma_3^2)$, where σ_k is the empirical standard deviation of the set of observations of field k, $k =$ LE, H, or T_s, for latent heat flux, sensible heat flux, and top soil layer temperature, respectively. The specific form

of Σ is addressed in Section 2.3.2.

The likelihood function $L(y|\theta,\alpha)$ of $y = (y(1),\ldots,y(145))^T$ (where there are 145 days of data) is then a product of univariate normal likelihoods. Given a joint prior distribution $\pi(\theta,\alpha)$ on the calibration parameters and biases, the joint posterior probability is

$$\pi(\theta,\alpha|y) \propto L(y|\theta,\alpha)\pi(\theta,\alpha). \tag{2.6}$$

This posterior density contains all uncertainty information regarding the model parameters and biases, and optimal values can be derived directly from the posterior (e.g., a posterior median minimizes absolute Bayes loss).

Prior distributions are required for the model parameters and bias parameters, and are assumed to be independent between parameters. Each individual component of θ was given a uniform prior with bounds $[1/10, 10]$. These hyperparameters are chosen to allow an order of magnitude deviation above or below the control model behavior and prevent non-physical negative parameter values. The model flux and temperature biases are assigned normal priors with mean zero and standard deviation 100 W m^{-2} for α_F and 100 K for α_T, representing a nearly uninformative prior.

A Markov chain of draws from the joint posterior distribution of θ and α (Equation 2.6) is constructed using the Metropolis-Hastings algorithm [95, 53]. This approach follows the detailed outline presented by [55] for model calibration, and a brief overview of the algorithm is given here.

(1) Initial values for the Monte Carlo iteration are selected (θ_0 and α_0).

(2) The Metropolis-Hastings algorithm (below) is iterated for $j = 2,\ldots,N$:

   (a) θ_{new} is drawn from a normal distribution with mean θ_{j-1} and variance s_θ^2. Similarly, α_{new} is drawn from a normal distribution, $N(\alpha_{j-1}, s_\alpha^2)$.

   (b) The posterior probability of these new iterates, $\pi(\theta_{new},\alpha_{new}|y)$, is calculated according to Equation 2.6.

   (c) The acceptance probability, p, is calculated as $p = \min\left(1, \dfrac{\pi(\theta_j,\alpha_j|y)}{\pi(\theta_{new},\alpha_{new}|y)}\right)$.

(d) Select the next MCMC iterate:

$$\theta_{j+1}, \alpha_{j+1} = \begin{cases} \theta_{new}, \alpha_{new}, & \text{with probability } p \\ \theta_j, \alpha_j, & \text{with probability } 1-p \end{cases} \tag{2.7}$$

The proposal density variances were initialized at $s_\theta^2 = 1$ and $s_\alpha^2 = 1$. After 500 iterations, the adaptive Metropolis algorithm described by [49] is implemented. The covariance matrix used to propose new calibration parameters is the covariance matrix of the previous iterates, scaled by $s_d = 2.38/\sqrt{N}$ to optimally explore the parameter-space, where N is the dimension of the parameter-space [40].

The above Markov chain model generates samples from the posterior distribution of model parameters θ and additive biases α. Initial testing using a Latin hypercube analysis of the six-dimensional parameter-space (four calibration parameters and two additive biases) highlighted a unimodal region of high likelihood near $\theta = (1.50, 0.85, 3.80, 1.00)^T$; Markov chains for the calibration parameters are therefore initialized at these values. The additive biases, α_0^i, are initialized at 24 W m^{-2} and 4.0 K, in light of the biases from the control model behavior (Figure 2.1). Initialization of $\theta_0 = 1$ and $\alpha_0 = 0$, or dispersed initial conditions, are both viable and attractive options, but are not used due to slow convergence to the same posterior modes, based on preliminary experiments. Furthermore, convergence implies that the convergent Markov chain behavior is independent of their initial conditions.

Theoretically, the Metropolis-Hastings algorithm converges to a stationary distribution of the calibration parameters and biases. The Gelman-Rubin diagnostic is used to assess convergence of our sampling chains [41]. Six parallel runs of the adaptive Metropolis-Hastings algorithm outlined above are each iterated 30,000 times. The first half of each run is discarded for burn-in and the remaining values are used for analysis. No thinning is done [86].

2.3.2 Error covariance

Following [72], four distinct error terms compose the total uncertainty: $\sigma_k^2 = \sigma_{str,k}^2 + \sigma_{par,k}^2 + \sigma_{obs,k}^2 + \sigma_{rep,k}^2$. Each of these component uncertainties is described below.

Structural uncertainty ($\sigma_{str,k}$) is the inherent disagreement between any physical model and the process it seeks to model, due to the use of approximate equations of nature. We formally define this as the difference between the model response at the true values of the calibration parameters and the mean of the physical process being modeled [72], and is assumed here to result in a constant bias rather than contribute to random uncertainty. Because these optimal parameters are unknown, structural uncertainty may only be estimated. In the present work, the bias calibration terms account for structural uncertainty, and the biases are obtained from the posterior.

Observational uncertainty ($\sigma_{obs,k}$) is error due to imperfect measurement systems. The values used are $\sigma_{obs,LE} = 22$ W m^{-2} and $\sigma_{obs,H} = 15$ W m^{-2} [126]; and $\sigma_{obs,T_s} = 0.5$ K (supplied by manufacturer). Eddy covariance methods rely on measurements of wind speed, temperature and humidity originating from a MEF tower observatory, which represents the entire tower footprint. Thus, defining the spatial scale of interest to be that represented by eddy covariance fluxes, $\sigma_{obs,H}$ and $\sigma_{obs,LE}$ incorporate representation uncertainty as well.

Representation uncertainty ($\sigma_{rep,k}$) results from heterogeneity in the site or region selected to model. Based on the estimates of sub-grid scale variability in surface temperature found from high-resolution modeling, we set the representation uncertainty for the top soil layer temperature at $\sigma_{rep,T_s} = 2$ K [33]. $\sigma_{rep,LE}$ and $\sigma_{rep,H}$ are incorporated into $\sigma_{obs,LE}$ and $\sigma_{obs,H}$.

Parametric uncertainty ($\sigma_{par,k}$) results from uncertainty in model parameters. While the purpose of this assimilation calculation is to reduce parametric uncertainty (that associated with the ecosystem resistance terms), CLM4 has many other parameters which attempt to best represent the physical attributes and ecosystem behavior of the observation site. Among these parameters are surface albedo, leaf area index (LAI), soil texture (percentage of soil which is sand, silt or clay), and percentages of the vegetation which is bare soil, trees, grass or shrubs. Following [25],

a sensitivity analysis is performed to inform an estimate of parametric error. First, a series of 11 model simulations are produced: (1) a control run, (2-3) ±20% sand fraction, in estimating soil hydraulic conductivity, (4-5) ±20% LAI, (6-7) ±20% albedo, and (8-11) +20% bare soil, trees, grass, shrubs, individually. For each simulation, the RMS deviations between the control modeled and the experiment modeled latent heat flux, sensible heat flux, and top soil layer temperature are calculated. For each of these fields, the parametric uncertainty of the quantity in question is estimated as the Euclidean distance of the 10-dimensional RMS deviation point from the sensitivity tests to the origin. These result in parametric uncertainty estimates of $\sigma_{par,LE} = 3.86$ W m^{-2}, $\sigma_{par,H} = 3.09$ W m^{-2} and $\sigma_{par,T_s} = 0.15$ K. These estimates are the maximum deviation considering fairly large (20%) perturbations on each parameter. Thus, the true uncertainty due to these parameters is likely lower than these estimates. Conversely, uncertainty due to feedbacks when multiple parameters are perturbed simulataneously and uncertainty due to parameters not considered here conspire to increase the parametric uncertainty beyond this estimate. While CLM4 has other parameters and parameterizations which would need to be accounted for to fully quantify parametric uncertainty, these experiments provide a sufficient estimate of $\sigma_{par,k}$. Furthermore, the contribution of $\sigma_{obs,k}$ to σ_k is much larger than any reasonable estimate of $\sigma_{par,k}$.

A series of three experiments is conducted to assess the importance of accounting for different uncertainty terms in this land surface model calibration. In the first experiment, herein referred to as "E1", the structural and parametric uncertainies in the statistical model are neglected. Thus, the error covariance matrix Σ has entries given by $\sigma^2_{obs,k}+\sigma^2_{rep,k}$. The second experiment (E2) incorporates the structural uncertainty (additive biases) into the statistical model. The final experiment (E3) makes use of the full uncertainty accounting outlined above, incorporating the additive bias terms into the model calibration, and the entries of the error covariance matrix Σ are given by $\sigma^2_{obs,k} + \sigma^2_{rep,k} + \sigma^2_{par,k}$.

Table 2.1: 95% Credible Intervals

	E1			E2			E3		
	P2.5	**Median**	**P97.5**	**P2.5**	**Median**	**P97.5**	**P2.5**	**Median**	**P97.5**
f_g	9.37	9.88	10.0	2.00	4.74	9.48	1.92	4.49	9.22
f_s	0.85	0.89	1.63	0.52	0.59	0.92	0.52	0.59	0.94
f_a	1.41	3.35	5.23	3.23	6.23	9.37	3.21	6.30	9.37
f_b	0.11	0.29	0.80	0.14	0.90	3.16	0.14	0.92	3.27
α_F	-	-	-	20.20	23.23	26.54	20.14	23.25	26.70
α_T	-	-	-	2.54	3.20	3.87	2.56	3.22	3.93
f_T	65.4	72.2	74.0%	62.6	73.6	80.4%	61.4	73.1	80.1%

2.4 Results

2.4.1 Posterior inference and the importance of uncertainty terms

The calibration technique results in robust constraints on the model parameters, additive biases (Figure 2.2) and the modeled transpiration fraction (f_T, Figure 2.3) for each of the three experiments. The 95% credible intervals and medians for the parameters, biases, and transpiration fraction are given in Table 2.1. The uncalibrated model estimate of f_T was 63.4%, shown as a vertical red line in Figure 2.3. The posterior estimates differ significantly when structural uncertainty is not taken into account (Figure 2.3, E1 versus E2 and E3). Parametric uncertainty plays a minor role in the error covariance matrix, implying that the representation uncertainties in the model (CLM4) and the observational uncertainties in the field data (eddy covariance for fluxes and thermistors for temperature) have greater effects (Figures 2.2 and 2.3, E2 versus E3). The uncalibrated estimate of f_T is within the 95% credible interval for f_T based on the E2 and E3 posterior estimates, but falls 10% lower than the posterior medians of f_T = 73.6 and 73.1% (E2 and E3, respectively). Thus, for the needleleaf evergreen forest site from which these observational data originate, uncalibrated CLM4 produces a transpiration fraction which is biased low by approximately 10% due to the structural and parametric uncertainty, observational uncertainty, and representation uncertainty between the model and observations of soil temperature and latent and sensible heat fluxes.

In experiments E2 and E3, well-defined posterior modes are found for all calibration biases

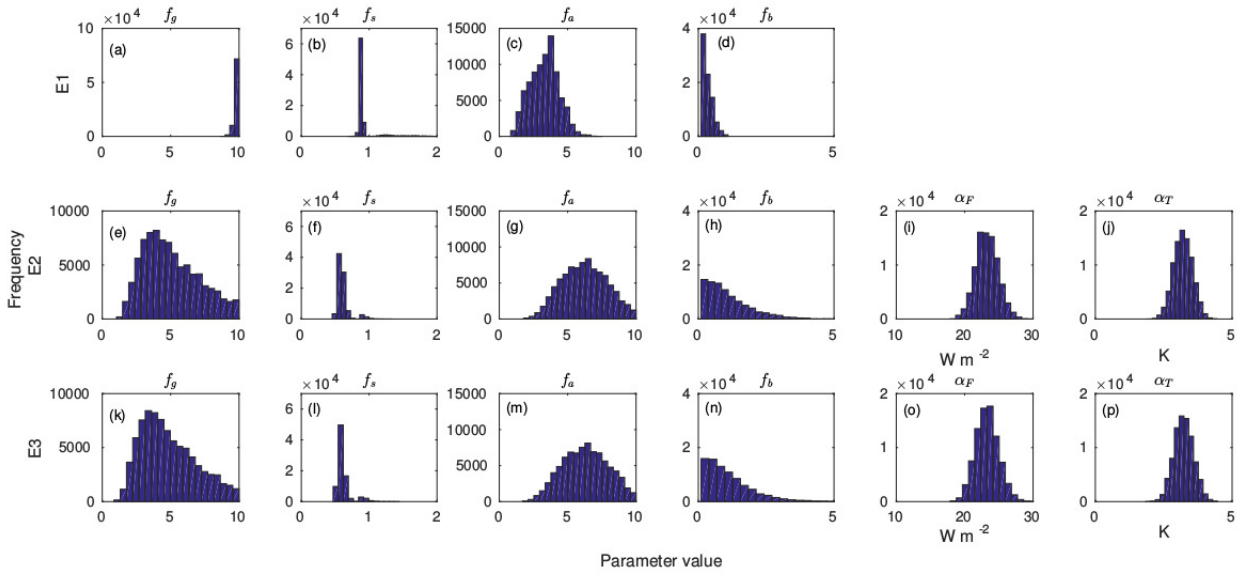

Figure 2.2: Frequency distributions of the calibrated model parameters and biases. Top row (a-d): results for E1; middle row (e-j): results for E2; bottom row (k-p): results for E3.

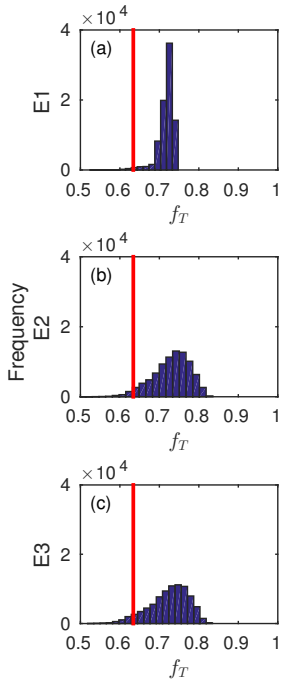

Figure 2.3: Frequency distributions of the calibrated transpiration fraction in (a) E1, (b) E2, and (c) E3. The vertical red lines show the control model ET partitioning.

and parameters except leaf boundary layer resistance (Figure 2.2, panels (h) and (n)). That the posterior distribution fit for f_b is heavily right-skewed and accumulates near the lower boundary at 0 suggests additional data may be required to constrain this parameter. The data constrain the model stomatal resistance parameter strongly (95% credible interval width of 0.42 for E3) and constrain the aerodynamic resistances well (95% credible interval widths of 7.3 for f_g and 6.16 for f_a in E3). The major mode of the posterior distribution for the stomatal resistance parameter ($f_s = 0.6$) is accompanied by small secondary modes at $f_s = 0.9$ for E2 and E3 (Figure 2.2f and l). This secondary mode is coincident with the mode found by E1 in the case where structural uncertainties (additive biases) were neglected (Figure 2.2b). The overwhelmingly higher frequency of posterior draws from the major mode and negligible impact of this secondary mode on the posterior distribution of the quantity of interest (f_T) means this secondary mode may safely be ignored in any practical application. The physical significance of this mode is discussed below.

The surface-to-canopy aerodynamic resistance (f_g) and transpiration fraction (f_T) parameters are positively correlated ($r = 0.76$, $p < 10^{-5}$), and the stomatal resistance (f_s) and f_T are negatively correlated ($r = -0.75$, $p < 10^{-5}$; Figures 2.4d and g). These relationships are due to the physical effect of these resistances: the total evapotranspiration is constrained by observations of latent heat flux, so stronger resistance to moisture transport between surface and canopy air-space (i.e., an increase in f_g) suppresses evaporation, leading to an increase in transpiration fraction. Similarly, higher stomatal resistance suppresses transpiration, leading to a decrease in transpiration fraction. The secondary mode at $f_s = 0.9$ represents model realizations with slightly lower f_T as a result of the increased stomatal resistance relative to the primary mode at $f_s = 0.6$. Additionally, photosynthesis scales inversely with stomatal resistance, so the modeled photosynthesis rate at the secondary mode is higher than the rate at the primary mode (not necessarily 50% higher, due to feedbacks). The success of the calibration approach in E2 and E3 in highlighting the most likely mode over the secondary mode relies on proper accounting of the model bias (structural uncertainty). No substantial correlation is present between any of the other parameters or transpiration fraction (Figure 2.4).

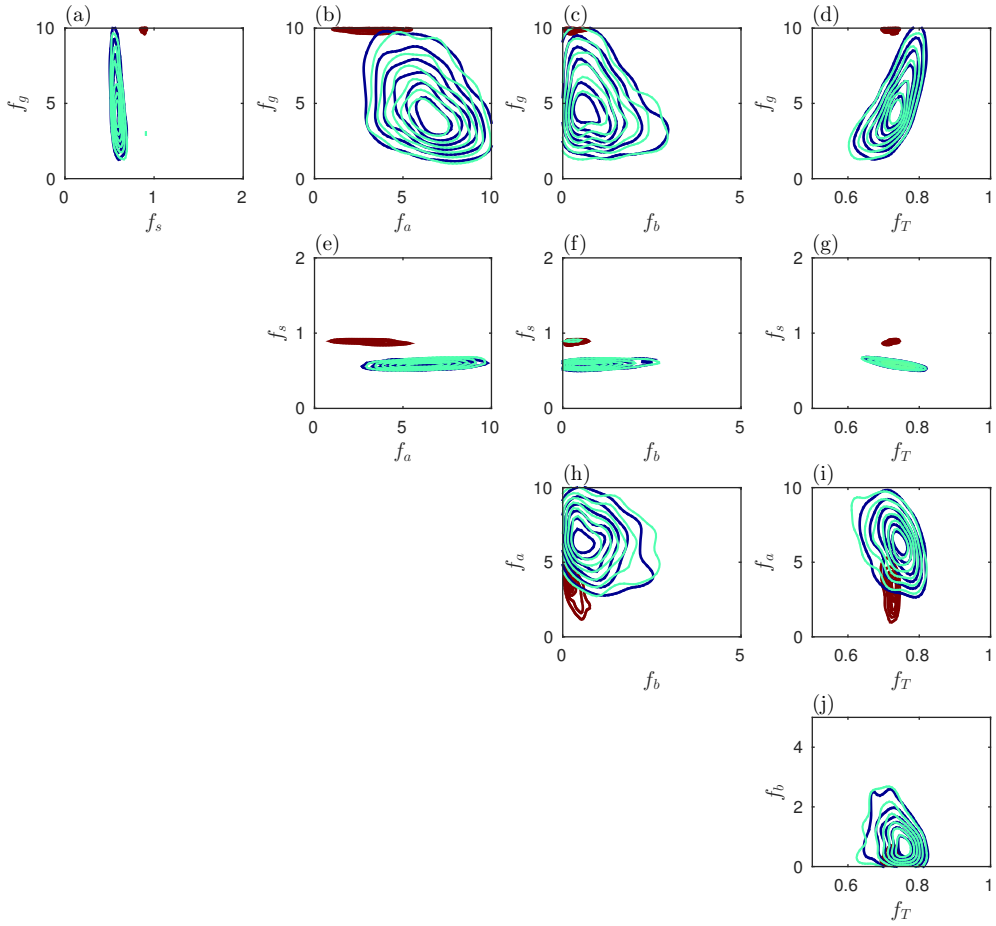

Figure 2.4: Pairwise posterior estimates between calibration parameters and transpiration fraction. These two-dimensional Gaussian kernel density estimates were generated using the results from the E1 (red contours), E2 (teal contours) and E3 (blue contours) simulations. Note that in many cases, the E2 and E3 contours are nearly indistinguishable.

2.4.2 Observationally-constrained model performance

The calibration technique yields considerable improvement in the agreement between the modeled latent heat flux, sensible heat flux, and top soil layer temperature and observations of these quantities (Figure 2.5). A posterior ensemble of model realizations was generated by drawing 100 random samples from the posterior estimates of the resistance parameters and corresponding

additive biases. This was done using the Markov chain results for each of E1, E2 and E3 (first, second and third columns in Figure 2.5, respectively). The results for E1, in which structural uncertainty was omitted, show poor model performance for latent heat flux after calibration, and modest improvement in sensible heat flux and soil temperature (Figure 2.5a-c). Thus, it is of critical importance to ensure the assumption of normally distributed errors is satisfied [55]. The additive bias corrections are used here to satisfy this normal error assumption; by neglecting them, model performance will be poor.

As compared to the uncalibrated model output (Figure 2.1), results for E2 and E3 showed vast improvement, especially in the simulation of latent heat flux (Figure 2.5). When uncertainty in the ecosystem resistance terms is accounted for, modeled top soil layer temperatures and sensible heat fluxes also agree well with observations, given the spread in these ensemble members. Calibration (E3) decreased model bias from -29.4 W m^{-2}, -15.7 W m^{-2} and -2.8 K to -1.5 W m^{-2}, 0.37 W m^{-2} and -0.03 K for latent heat flux, sensible heat flux and top soil layer temperature, respectively. RMSE decreased from 27 W m^{-2}, 36 W m^{-2} and 4.4 K for uncalibrated latent heat flux, sensible heat flux and top soil layer temperature, to 16 W m^{-2}, 26 W m^{-2} and 1.3 K once calibrated in E2 and E3 experiments (Table 2.2). The reductions in RMSE correspond to percent improvements of 42, 27 and 71% for latent heat flux, sensible heat flux and top soil layer temperature, respectively. These posterior RMSE values are calculated as the mean of the RMSE from the ensemble of model runs at parameter values drawn from their posterior distributions. Note that the improvements in RMSE and bias are not only due to the accounting of structural uncertainty (i.e., the model additive bias terms), but also due to providing the calibration approach with the flexibility needed to converge to more realistic posterior parameter estimates (Figure 2.2).

The posterior model ensemble results for latent heat flux agree well with observations for mid- and late-season (DOY 155 and later), but struggle to accurately model early season evapotranspiration (DOY 125-155). This is attributed to an inadequate treatment of snow pack and melt water runoff during that time period, due partially to the increase in soil temperature which was a consequence of the improvement in match between modeled and observed soil temperature,

brought on by the calibration. The distributions of the model errors with respect to the observations are widened by the calibration (Table 2.2). In the table, the parenthetical values give the width between the 2.5 and 97.5% percentiles of the uncalibrated model and calibrated model ensemble errors. These wider distributions of errors are due to model representation, structural, parametric, and observational uncertainties all factoring into these errors. While the distributions are indeed wider, they are also centered closer to zero (lower RMSE and model bias), indicative of the improvement due to refinement of the ecosystem resistance parameterizations.

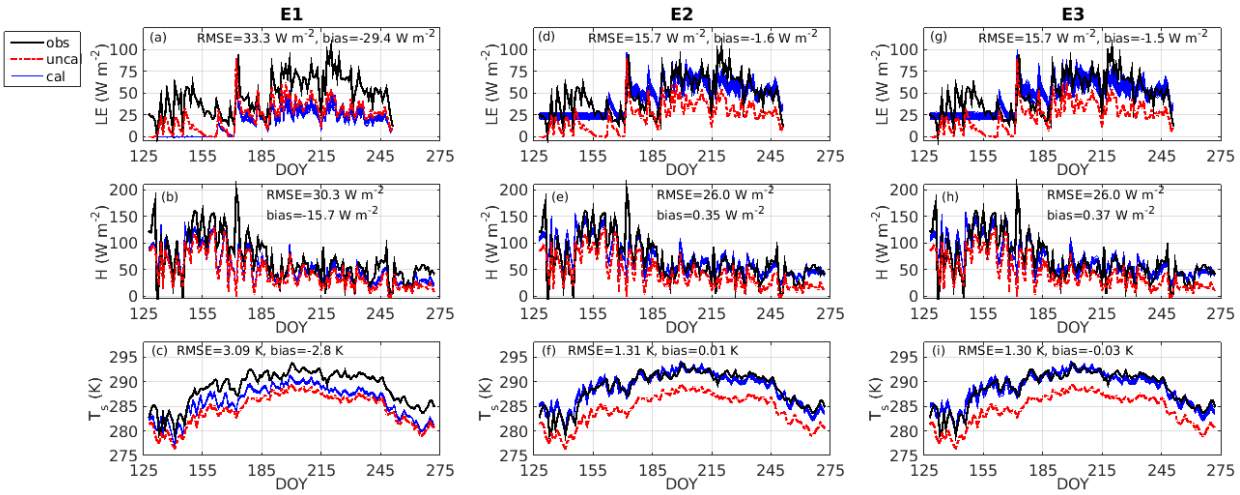

Figure 2.5: Modeled fluxes of latent heat (a, d, g) and sensible heat (b, e, h) and temperature (c, f, i), using calibration parameters drawn from the Markov chain results. Bold black lines are the observations, thin blue lines are the posterior ensemble results and the dot-dash red line is are uncalibrated model results. (a-c) draws from the posterior estimates from E1; (d-f) posterior draws from E2; (g-i) posterior draws from E3.

2.5 Discussion and conclusions

We have outlined and implemented a Bayesian approach for the calibration of land surface model parameters. This calculation demonstrates that the challenges posed by having only data with large total errors and models with large intrinsic biases may be overcome by adequately accounting for all error sources and biases, within the optimization scheme. The approach focused on the goal of improving estimates of the transpiration fraction and therefore emphasized calibration of

Table 2.2: RMSE (and 2.5–97.5 Percentile Range of Errors, in parentheses), Uncalibrated Model and Model Ensembles

	Latent heat flux ($W\ m^{-2}$)	**Sensible heat flux** ($W\ m^{-2}$)	**Soil temperature** (K)
Uncalibrated	27.33 (49.24)	35.91 (99.12)	4.43 (4.19)
E1	33.32 (58.99)	30.34 (106.84)	3.09 (5.62)
E2	15.74 (64.12)	26.01 (107.93)	1.31 (5.83)
E3	15.77 (64.27)	26.03 (108.14)	1.31 (5.78)

aerodynamic and vegetation resistances for heat and moisture which control the exchange between soils, leaves and the overlying atmosphere. We have demonstrated the ability of this calibration approach to constrain the posterior distributions of aerodynamic and vegetation resistance parameters in CLM4. The advantages of this method include (1) quantification of uncertainty in model structure, model parameters and model output (Tables 2.1 and 2.2) and (2) calibrating model parameters such that model output agrees with observational data to within the errors inherent in both the model and observations.

The experiments presented here found that implementing the calibration procedure reduced RMSE for all three sets of observational data. While the calibration improved model performance for latent and sensible heat fluxes and top soil layer temperature, model performance for soil moisture deteriorated only for the early season snow melt (DOY 125-155). E2 and E3 improved the match between modeled top soil layer temperature and observations, which required raising the temperature by several s. This, in turn, likely caused the precipitation which would have formed this snow pack to fall as rain instead of snow. Additionally, this difficulty in simulating the snow pack at MEF is consistent with the results of CLM4 experiments conducted by [82] (cf. Figures 2 and 6), whose global experiments found that CLM4 underestimated snow cover fraction relative to observations in central USA. Explicit calibration of the early season snow pack sublimation and melting, or assimilating soil moisture data are potential avenues to fix this issue. Other model water pools and fluxes were not significantly affected by the calibration.

A soil moisture data assimilation experiment was conducted to assess the extent to which the imperfect simulation of soil moisture in the ensemble affected the modeled latent and sensible

heat fluxes and transpiration fraction. Soil moisture as modeled by CLM4 was "nudged" towards observations of soil moisture such that RMSE in the modeled soil moisture profile was reduced from 0.13 mm^3 mm^{-3} (uncalibrated, unassimilated model) to 0.06 mm^3 mm^{-3} (uncalibrated, assimilated model). This assimilated model, matching the soil moisture data well, yielded only slight changes in the surface fluxes: the mean difference between the control and moisture-assimilated latent and sensible heat fluxes were -1.70 and 1.63 W m^2, respectively, much lower than the uncertainties in these quantities. The deviation in modeled transpiration fraction was imperceptible: the mean transpiration fraction in the control model was 0.622, while the moisture-assimilated f_T value was 0.624. It is therefore unlikely that the results of this study were significantly skewed by an imperfect simulation of soil moisture. Regardless of the soil moisture state, the present study has evaluated the importance of various uncertainties inherent in physical models and the observations used to force and validate them, and provided a practical demonstration of the ability to overcome these uncertainties to obtain useful model results and constraint on model parameters.

The posterior distributions of the aerodynamic and vegetation resistance calibration parameters were not centered at one, implying model tuning should be performed for CLM4 to best match observations of surface fluxes and top soil layer temperature at the semi-arid, needleleaf forest site in central Colorado, USA, studied here. The calibration parameters for the surface-to-canopy and canopy-to-above-canopy aerodynamic resistances had the widest 95% credible interval posterior ranges for E3 (Table 2.1). The stomatal resistance calibration parameter, by contrast, was strongly constrained by the assimilated data. These results suggest significant limitations in the characterization of turbulent regimes within the complex canopy of the MEF site, and is likely a result which is applicable to other types of landscapes. Thus, for any given site, it is reasonable to expect to tune the model to account for this representative discrepancy. Doing so for a network of sites would permit the interpolation of the benefits of this calibration approach to the regions between sites within the network, and cautious extrapolation to the areas outside of the network, where observations are lacking. This is a similar endeavor to that of [25], and offers a method to improve model hydrological performance on a global scale, despite the lack of readily available global data

sets against which to calibrate.

The ecosystem resistance parameters chosen in the present study are clearly not exhaustive, yet serve well to demonstrate the potential for this calibration method to be applied to a wide range of land surface modeling applications. Furthermore, the sensitivity analysis described in Section 2.3.2 was a representative, but not complete, treatment of the parametric uncertainty in CLM4. Possible extensions of the present work include incorporating additional or different model parameters as calibration parameters and assimilating other observational data. Observations of soil moisture or stable water isotope ratios in ecosystem water pools, for example, would offer further constraint on the moisture fluxes, and CO_2 fluxes would offer constraint on stomatal resistance, independent of transpiration rates, and thus encourage a distrinction between the primary and secondary modes in the posterior distribution for f_s. Indeed, this type of statistical approach has been used widely with success in carbon cycle applications [51, 138]. Soil moisture is directly related to evapotranspiration, but high-quality observations are scarce, and modeling small-scale processes (puddles on the land surface, lateral flow within the soil profile, and vapor diffusion, for example) is a formidable task for complex land surface models; large structural and representation errors are present. LAI was considered in the sensitivity analysis presented in Section 2.3.2, but is an attractive parameter to incorporate into the calibration itself. The modeled stomatal resistance scales inversely with photosynthesis, which in turn scales directly with LAI. CLM4 prescribes LAI based on vegetation type and location from a monthly set of average values, interpolated from data, since precise estimates are not known in a routine manner at site to ecosystem scales and phenology is not constant from one year to the next. Surface and vegetation heterogeneity (i.e., model representation error) lead to discrepancy between the observations and model output for the MEF site, which represents an area much larger than the MEF tower footprint [114, 64, 31].

The poor performance of experiment E1 provided the essential result that failure to satisfy the assumption of normally distributed errors with mean zero is detrimental to assimilation techniques [55]. In this application, by including the additive bias terms as additional calibration parameters, the normal error assumption was satisfied, and experiments E2 and E3 performed well. There may

be practical applications which are of such high dimension that adding dimensionality equal to the number of bias terms entertained is an unacceptable increase in the size of the parameter-space to be explored. Therefore, further investigation is needed into alternative methods for fulfilling the assumption of normally-distributed errors with mean zero in cases where it is not satisfied. In the present application, it is clear that accounting for structural uncertainty resulted in the most dramatic improvement in the match between model output and observations; model biases must not be neglected.

The single column land surface model calibration experiment presented here may be reproduced for a representative network of sites scattered on a regional scale, to create calibrated regional surface data sets and calibrated model predictions. With the advent of widely available high quality tower data for validation and calibration of land surface models [71], there are increasing opportunities for assimilating models and hydrological and meteorological data. Tower data, collected at a network of sites representative of the larger regional or global landscape, would permit a large spatial scale model calibration approach at a lower computational cost. It will undoubtedly remain critical to utilize both quality observations and advanced modeling frameworks to the fullest extent of their abilities.

Chapter 3

Evaluation of modeled land-atmosphere exchanges with a comprehensive water isotope fractionation scheme in Version 4 of the Community Land Model

3.1 Introduction

Recent years have seen the proliferation of field deployable instruments capable of making measurements of stable water isotope ratios, as well as the wide availability of the computational power necessary to run model simulations of the ecosystems from which measurements originate. This places great importance on developing tools at the interface of these two scientific advances, specifically for the synthesis of measurements of stable water isotopic ratios and isotopically-enabled model simulations. The availability of water isotopic measurements at high temporal resolution provides an opportunity to validate the land surface schemes [45]. These isotope-enabled land surface models are in high demand in order to gain unique insight into hydrological processes and biogeochemical behaviors of ecyosystems, and it has been shown that through proper simulation of the below-canopy isotopic exchanges between surface and canopy air-space, better agreement between model and observations may be achieved [1, 119].

We present a tracer hydrological scheme, incorporated into the National Center for Atmospheric Research's Community Land Model, Version 4 (CLM4) [103]. CLM4 is the land surface component of the Community Earth System Model (CESM) [59], and was selected for the incorporation of a tracer hydrological model due to the high utility in having a tracer-enabled freely available community climate model such as CESM. The tracer hydrological scheme in iCLM4 closely parallels the native hydrology in CLM4, with several critical additions which enable the modeling

of hydrological tracers. These tracers may be temporal (such as tracing summer rainfall through the hydrological cycle), spatial (such as tracing rain reevaporation from the Amazon rainforest), or isotopic (tracing heavy isotopologues). The focus of the present work is on the latter, and therefore much of the methodological discussion focuses on the effects of isotopic fractionation on the isotopic fluxes of evaporation (from surface and canopy-intercepted water) and transpiration.

This chapter is organized as follows. Section 3.2 provides a technical review of the isotope tracer model. Section 3.3 outlines the datasets used for validation of the model results, and Section 3.3.2 details global sensitivity experiments conducted by coupling the isotopic land surface scheme reviewed in the present work with the complementary stable water isotope-enabled atmospheric model. A review of the practical implications of these results and future work is given in Section 3.4.

3.2 Isotope model for terrestrial water exchange

Figure 3.2 depicts the main iCLM4 isotopic water pools (light blue) and fluxes between them (red arrows). The interested reader is directed to Figure 1.2 in [103] for a more detailed schematic of all water pools and fluxes in CLM. Each water flux in the model is accompanied by an analogous water isotopic flux.

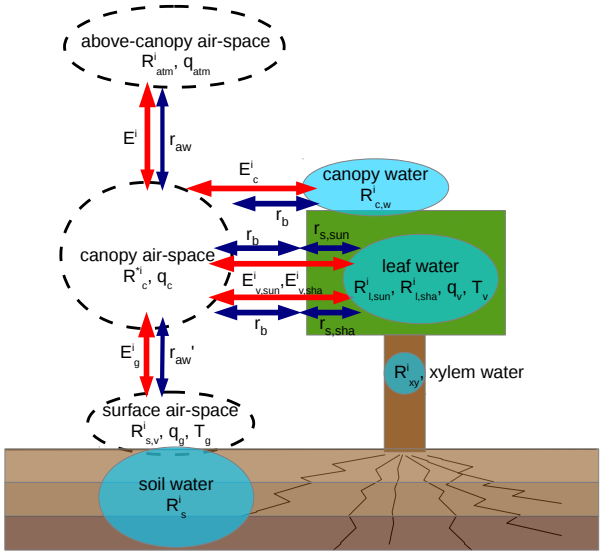

The essence of the isotopic tracer scheme is to estimate these isotopic fluxes between the atmosphere and land surface (evaporation from soil, evaporation of water intercepted by the canopy and transpiration), and in order to do so, predict the isotopic composition of all water pools. At the end of each model time step the mass of all isotope species is checked to ensure the change in storage in soil, snow and canopy intercepted water is equal to the input from rain and snow, minus the output to evapotranspiration (ET) and surface and subsurface runoff.

Let i refer to any specific water isotopologue. Surface evaporation, E_g^i, transports water between the surface soil (or top snow pack layer) and the canopy air-space. Sunlit and shaded leaf transpiration, $E_{v,sun}^i$ and $E_{v,sha}^i$, respectively, transport water from within leaves to the canopy air-space. Evaporation of canopy-intercepted water, E_c^i, moves water between the surface of leaves and the canopy air-space. E^i denotes the transfer of moisture between the canopy air-space and the above-canopy air-space. When coupled to an isotopically-enabled GCM, E^i is the coupling flux to the GCM. The balance of these five fluxes in the canopy air-space is illustrated in Figure 3.2 and may be expressed as

$$E^i = E_g^i + E_{v,sun}^i + E_{v,sha}^i + E_c^i \ . \tag{3.1}$$

CLM stores water on the landscape in three distinct reservoirs: soil water, snow pack and water intercepted by the canopy. Within soil, water may be either liquid or frozen, and while liquid water is considered in the thermodynamics of snow pack a separate liquid mass content is is not tracked. Conservation of mass (Equation 3.2) and Darcy's Law (Equation 3.3) govern the soil moisture parameterization, for both bulk water and isotopic water, and are combined to yield a modified Richards equation for the soil water isotopic fluxes throughout the soil column (Equation 3.4). In Equations 3.2, 3.3 and 3.4, i denotes any water isotopologue; θ^j is the soil water content of the soil layer j ($\mathrm{mm}^3\ \mathrm{mm}^{-3}$); t is time (s); q^j is the water flux from the current soil layer to the one below it ($\mathrm{mm\ s}^{-1}$); z is soil layer depth (mm); Q^j is a soil moisture sink term (e.g., evaporation) ($\mathrm{mm\ s}^{-1}$); k is hydraulic conductivity ($\mathrm{mm\ s}^{-1}$); ψ^j is the soil matric potential (mm); and ψ_E^j is the equilibrium state soil matric potential (mm). These fluxes between soil layers j and

$j+1$ are linearized about the moisture content of those layers to create a tridiagonal system of equations in terms of the soil moisture. This system is solved using the Crank-Nicholson method.

$$\frac{\partial \theta^j}{\partial t} = -\frac{\partial q^j}{\partial z} - Q^j \tag{3.2}$$

$$q^j = -k\left[\frac{\partial(\psi^j + z)}{\partial z}\right] \tag{3.3}$$

$$\frac{\partial \theta^j}{\partial t} = \frac{\partial}{\partial z}\left[k\left(\frac{\partial(\psi^j - \psi_E^j)}{\partial z}\right)\right] - Q^j \tag{3.4}$$

After the bulk soil moisture update (above), the isotope ratios of each layer's soil water are updated. This is done by dividing the model time step into n_{sub} substeps to maintain numerical stability. The total moisture fluxes between all adjacent soil layers are known, from conservation of mass and the surface boundary condition (soil infiltration and evaporation are known). During each time substep, $1/n_{sub}$ of the total moisture fluxes are moved between adjacent soil layers, and each substep interfacial flux carries the isotopic ratios from its layer of origin. After each substep, the isotope ratios of each soil layer are updated. In addition to the isotope ratios of HDO and $H_2^{18}O$ in soil liquid water and soil frozen water, iCLM4 computes the isotope ratios within vertically resolved snow pack, canopy intercepted water, sunlit and shaded leaf water and canopy air-space vapor, and all the fluxes which control the evolution of those reservoirs.

In CLM4, each model gridcell is composed of landunits, which include glacier, lake, wetland, urban and vegetated [103]. Note that vegetated landunits include bare soil, and in the isotope scheme described in the present work, only vegetated landunits incorporate any isotopic fractionation. For the other four landunit types, the tracers of all water species are treated identically, and do not fractionate. Vegetated landunits are divided into 17 "plant functional types," or PFTs. For the remainder of this work, "bare soil" shall refer to the PFT corresponding to bare ground and "vegetated" shall refer to all other PFTs.

3.2.1 Isotopic kinetic fractionation factor

It is useful to define the parameterizations of the isotopic kinetic fractionation factor, α_k, here. Two main formulations are used. The first is:

$$\alpha_k^i = \left(\frac{D_i}{D}\right)^n, n \text{ constant} \tag{M78}$$

In M78, i refers to the isotopic species, D and D_i are the molecular diffusivities in air of the light and heavy isotopologue, respectively [93], and the exponent n is chosen between 0 and 1 to represent the balance of turbulence versus diffusive transport for the water movement between the two isotopic reservoirs in question. [15] gives $n = 1/2$ as appropriate to turbulent conditions, $n = 2/3$ for flow over a smooth surface and evaporation from open bodies of water, and $n = 1$ for static conditions, or pure diffusional transport. [133] use $n = 1$ for evaporation from dry soils, where diffusion through the dry soil matrix is the primary form of moisture transfer, and $n = 1/2$ for evaporation from wet soil. In purely turbulent conditions, $n = 0$ is appropriate, because turbulent mixing treats all isotopic species equally, regardless of differing molecular properties. Although the optimal choice for the exponent n for a given set of environmental conditions is an area of ongoing debate and study, Equation M78 remains a popular choice [17, 111, 139, 133, 110, 131].

The second formulation is applied to surface evaporation only, and is adapted from the parameterization of kinetic fractionation for evaporation from rough ocean surfaces given by [94] (c.f., their Figure 2).

$$\begin{aligned} k^O &= \begin{cases} 8.82u_* + 0.472, & \text{if } R_e \geq 1 \\ 6, & \text{if } R_e < 1 \end{cases} \\ k^H &= 0.88k^O \\ \alpha_k^i &= \frac{1000 - k^i}{1000} \end{aligned} \tag{MJ79}$$

In MJ79, R_e is the Reynolds number, which represents whether the land surface conditions are in the smooth regime ($R_e < 1$) or rough ($R_e \geq 1$), and u_* is the friction velocity (m/s). The equation

given above for k^O (‰) is a linear fit for the results presented in Figure 2 of [94]. The kinetic effect represented by this parameterization acts over the entire evaporation column, from the surface to the above-canopy air space. This is in contrast to the typical evaporation scheme in CLM4, between surface and canopy air spaces. In the present work, MJ79 is only used to parameterize the kinetic fractionation factor for surface evaporation in a particular sensitvity experiment; the formulation of M78 is used by default, with $n = 2/3$.

3.2.2 Isotopic composition of evaporation and transpiration

3.2.2.1 Bare ground fluxes

Let E_g refer to the evaporation flux of $H_2^{16}O$, as calculated by native CLM4. The isotopic evaporation flux (kg m^{-2} s^{-1} is based on the model of [24]:

$$E_g^i = c_g^i \left((f_{s,eq} \frac{R_s^i q_g}{\alpha^i(T_g)} + (1 - f_{s,eq}) R_{atm}^i q_{atm}) - R_{atm}^i q_{atm} \right). \tag{3.5}$$

where

$$f_{s,eq} = \begin{cases} exp\left(-\Delta t \frac{r_{aw} q_{atm}}{\theta_1 - \Delta t E_g} \right), & \text{if } E_g \geq 0 \text{ and} \\ 1, & \text{otherwise} \end{cases} \tag{3.6}$$

$f_{s,eq}$ ranges from 0 to 1 and is the fraction of tracer evaporation source water which is not in equilibrium with the tracer evaporation destination water (atmospheric water vapor); r_{aw} (s m^{-1}) is the aerodynamic resistance to moisture and heat transport from surface to above-canopy air-space (discussed further below); E_g is the bulk water surface evaporation (mm s^{-1}); θ_1 is the volumetric moisture content of the top soil layer (mm^3 H_2O mm^{-3} soil); Δt is the model time step (1800 s); q_g is the specific humidity of the air at the ground surface; q_{atm} is the atmospheric specific humidity; c_g^i is the water isotopic conductance between the evaporating surface and the above-canopy air-space; α^i is the equilibrium fractionation factor at T_g, the temperature of the evaporating surface [56]; R_{atm}^i is the isotope ratio of the atmospheric forcing specific humidity; and R_s^i is the isotope ratio of the total soil water and ice on the evaporating surface. Ice is included in the calculation to account for possible sublimation or dew/frost onto snow or ice. $f_{s,eq}$ takes into account partial

isotopic equilibration between evaporation source water and canopy water vapor. For sublimation ($T_g < T_{frz}$ and $E_g > 0$), no kinetic nor equilibrium fractionation is applied.

The Monin-Obukhov stability iteration used in CLM4 results in an aerodynamic resistance to moisture and heat transport from surface to above-canopy air-space, r_{aw} (s m^{-1}). The water isotopic conductance is then

$$c_g^i = \begin{cases} \dfrac{1}{\frac{r_{aw}}{\alpha_k^i}}, & \text{if } q_{atm} > q_g \\ \dfrac{\beta_{soi}}{\frac{r_{aw}}{\alpha_k^i}}, & \text{if } q_{atm} \leq q_g \end{cases} \tag{3.7}$$

where β_{soi} ranges from 0 to 1 and represents the molecular diffusion process from the soil pore to the surface within the dry part of the soil [103, 112], and α_k^i is the isotopic kinetic fractionation factor for isotopic species i. For bare ground evaporation, α_k^i is parameterized following M78 with $n = 2/3$.

3.2.2.2 Vegetated fluxes

For each isotopic species, i, a five-way water isotopic mass balance in the vegetation canopy is solved between: (1) ground evaporation (E_g^i), (2) evaporation of canopy-intercepted water (E_c^i), (3 and 4) sunlit and shaded leaf transpiration ($E_{v,sun}^i$ and $E_{v,sha}^i$), and (5) atmospheric water vapor (E^i). This calculation originates from [108], although iCLM4 supports the addition of the evaporation flux of canopy-intercepted water. These fluxes are all formulated in the spirit of [24]. For a given isotopic species, i, the total isotopic ecosystem water flux, E^i (Equation 3.1), and its

constituents are

$$E^i = \rho_{atm} c_a^i \left(R_c^{*i} q_c - R_{atm}^i q_{atm} \right) \tag{3.8}$$

$$E_g^i = \rho_{atm} c_g^i \left(c_{al,0} (f_{s,eq} R_{s,v}^i + (1 - f_{s,eq}) R_c^{*i}) q_g - c_{l,0} R_{leaf}^i q_{sat,l}(T_v) - c_{a,0} R_{atm}^i q_{atm} \right) \tag{3.9}$$

$$E_c^i = \rho_{atm} c_c^i \left(\left(f_{c,eq} \frac{R_{c,w}^i}{\alpha^i(T_v)} + (1 - f_{c,eq}) R_c^{*i} \right) q_{sat,l}(T_v) - R_c^{*i} q_c \right) \tag{3.10}$$

$$E_{v,sun}^i = \rho_{atm} c_{sun}^i \left(\frac{R_{l,sun,s}^i q_{sat,l}(T_v)}{\alpha^i(T_v)} - R_c^{*i} q_c \right) \tag{3.11}$$

$$E_{v,sha}^i = \rho_{atm} c_{sha}^i \left(\frac{R_{l,sha,s}^i q_{sat,l}(T_v)}{\alpha^i(T_v)} - R_c^{*i} q_c \right) \tag{3.12}$$

In Equations 3.8–3.12, R_c^{*i} is the isotope ratio of the canopy water vapor at steady state; $R_{l,sha,s}^i$ and $R_{l,sun,s}^i$ are the isotope ratios of the sunlit and shaded leaf water, respectively, at steady state; R_{atm}^i is the isotope ratio of the atmospheric water vapor used (above-canopy water vapor); $R_{soi,v}^i$ is the isotope ratio of the evaporation front water vapor (currently taken to be surface soil); $R_{c,w}^i$ is the isotope ratio of the canopy-intercepted water (i.e., water pooling on a leaf); $\alpha^i(T_v)$ is the equilibrium fractionation factor at the temperature of the temperature of the vegetation (T_v) [56]; $f_{c,eq}$ ranges from 0 to 1 and is the fraction of tracer evaporation source water (canopy-intercepted water) which is not in equilibrium with the tracer evaporation destination water (canopy water vapor); q_{atm} is the atmospheric vapor pressure; $q_{sat,l}(T_v)$ is the saturation vapor pressure at the temperature of the transpiring vegetation; q_g is the water vapor pressure at the evaporation front; q_c is the vapor pressure in the canopy air-space. In Equation 3.9, R_{leaf}^i is the average (sunlit/shaded) LAI-weighted leaf water isotope ratio; c_a^i is the water isotopic conductance between the canopy and above-canopy air-spaces; c_g^i is the water isotopic conductance between the evaporating surface and canopy air-spaces; c_c^i is the water isotopic conductance between the canopy-intercepted water and canopy air-spaces; c_{sun}^i and c_{sha}^i are the water isotopic conductances between the sunlit and shaded leaf interiors and the canopy air-space, respectively; $c_{al,0}$ is the sum of the normalized conductances for the light isotopologue through the canopy to above-canopy air-spaces ($c_{a,0}$) and through the leaf air-space ($c_{l,0}$). The parameterization for the isotope ratios of sunlit and shaded leaf water is

from [36]:

$$R_{l,sun,s} = \alpha^i(T_v)\left(\frac{q_{sat,l}(T_v) - q_{l,sun}}{q_{sat,l}(T_v)}\frac{R^i_{xy}}{\alpha^i_{k,s}} + \frac{q_{l,sun} - q_c}{q_{sat,l}(T_v)}\frac{R^i_{xy}}{\alpha^i_{k,l}} + \frac{q_c}{q_{sat,l}(T_v)}R^{*i}_c\right) \tag{3.13}$$

$$R_{l,sha,s} = \alpha^i(T_v)\left(\frac{q_{sat,l}(T_v) - q_{l,sha}}{q_{sat,l}(T_v)}\frac{R^i_{xy}}{\alpha^i_{k,s}} + \frac{q_{l,sha} - q_c}{q_{sat,l}(T_v)}\frac{R^i_{xy}}{\alpha^i_{k,l}} + \frac{q_c}{q_{sat,l}(T_v)}R^{*i}_c\right), \tag{3.14}$$

where R^i_{xy} is the isotope ratio of vegetation xylem water; $q_{l,sun}$ and $q_{l,sha}$ are the water vapor pressures within the sunlit and shaded leaves, respectively; and $\alpha^i_{k,s}$ and $\alpha^i_{k,l}$ are the kinetic fractionation factors for moisture transport through vegetation stomata (M78, $n = 1$) and the leaf boundary layer (M78, $n = 2/3$), respectively [110].

The water isotopic conductances follow the native CLM4 calculation for their bulk water analogs:

$$c^i_a = \frac{f_{veg}}{\frac{r_{aw}}{\alpha^i_{k,a}}}$$

$$c^i_l = \frac{f_{veg}(L+S)}{\frac{r_b}{\alpha^i_{k,b}}}r''$$

$$c^i_g = \begin{cases} \dfrac{f_{veg}}{\frac{r'_{aw}}{\alpha^i_{k,g}} + \frac{r_{litter}}{\alpha^i_{k,litter}}}, & \text{if } q_{atm} > q_g \\ \dfrac{\beta_{soi} f_{veg}}{\frac{r'_{aw}}{\alpha^i_{k,g}} + \frac{r_{litter}}{\alpha^i_{k,litter}}}, & \text{if } q_{atm} \leq q_g \end{cases}$$

where f_{veg} is the fraction of the land surface which is vegetated but not covered in snow; L and S are the leaf and stem area indices, respectively; r_{aw} is the aerodynamic resistance between the canopy air-space and above-canopy (GCM) air-space; r'_{aw} is the aerodynamic resistance between the surface air-space and canopy air-space; r_{litter} is a leaf litter resistance; r_b is the leaf boundary layer resistance; and r'' is the fraction of potential evaporation from transpiration. Further information regarding the parameterization of all non-isotope-specific terms may be found in [103]. $\alpha^i_{k,b}$ is parameterized by M78 with $n = 2/3$ [36]. $\alpha^i_{k,litter}$ is by default equal to 1, representing a null hypothesis of no fractionation as moisture evaporates through the dry litter layer. $\alpha^i_{k,a}$ follows M78 with $n = 0$ because exchange between canopy and above-canopy air-spaces is dominated by turbulence [84]. $\alpha^i_{k,g}$ follows M78 with $n = 2/3$, which is consistent with open water evaporation,

and somewhere between wet and dry soil evaporative conditions [15, 92, 133, 108]. In native CLM4, evaporation is drawn from the top soil layer only, which is akin to open water evaporation or the evaporation of a puddle. iCLM4 preserves this feature, thus $n = 2/3$ is a natural choice for the exponent in M78 for the surface evaporation kinetic fractionation factor.

Given the bulk vegetation transpiration (E_v) and evaporation of canopy-intercepted water (E_c) fluxes of $H_2^{16}O$ calculated, effective conductances for these fluxes may be calculated in a manner consistent with the bulk transpiration and vegetation evaporation fluxes. They are then divided into sunlit and shaded leaf components:

$$c_c = \frac{E_c}{\rho_{atm}(q_{sat,l} - q_c)} \tag{3.15}$$

$$c_t = \frac{E_v}{\rho_{atm}(q_{sat,l} - q_c)} \tag{3.16}$$

$$c_{sun} = f_{sun} c_t \tag{3.17}$$

$$c_{sha} = (1 - f_{sun}) c_t \tag{3.18}$$

Now the effective conductances for isotopic species i are related to the bulk conductances as follows.

$$c^i_{sun} = \frac{c_{sun}}{r''} f_{dry} r_b \left(\frac{L_{sun}}{L_{sun} + L_{sha}} \Big/ \left(\frac{r_b}{\alpha^i_{k,b}} + \frac{r_{s,sun}}{\alpha^i_{k,s}} \right) + \frac{L_{sha}}{L_{sun} + L_{sha}} \Big/ \left(\frac{r_b}{\alpha^i_{k,b}} + \frac{r_{s,sha}}{\alpha^i_{k,s}} \right) \right)$$

$$c^i_{sha} = \frac{c_{sha}}{r''} f_{dry} r_b \left(\frac{L_{sun}}{L_{sun} + L_{sha}} \Big/ \left(\frac{r_b}{\alpha^i_{k,b}} + \frac{v}{\alpha^i_{k,s}} \right) + \frac{L_{sha}}{L_{sun} + L_{sha}} \Big/ \left(\frac{r_b}{\alpha^i_{k,b}} + \frac{r_{s,sha}}{\alpha^i_{k,s}} \right) \right)$$

$$c^i_c = \alpha^i_{k,c} c_c$$

$\alpha^i_{k,b}$ follows M78 with $n = 2/3$ for movement through the laminar leaf boundary layer and $\alpha^i_{k,s}$ follows M78 with $n = 1$ for diffusion through vegetation stomata. r'' is the fraction of potential evaporation from transpiration for $H_2^{16}O$, and given by

$$r'' = f_{dry} r_b \left(\frac{L_{sun}}{L_{sun} + L_{sha}} \Big/ (r_b + r_{s,sun}) + \frac{L_{sha}}{L_{sun} + L_{sha}} \Big/ (r_b + r_{s,sha}) \right) \tag{3.19}$$

Thus, for the tracer conductances c^i_{sun}, c^i_{sha}, and c^i_c, kinetic fractionation effects are simply incorporated into r''.

Substituting Equations 3.8-3.14 into Equation 3.1 permits solving for R^{*i}_c, the isotope ratio of the canopy water vapor at steady state. Algebra reveals

$$\begin{aligned} R^{*i}_c = \Big[& c^i_{sun} \left((q_{sat,l} - q_{l,sun}) \frac{1}{\alpha^i_{k,s}} + (q_{l,sun} - q_c) \frac{1}{\alpha^i_{k,l}}) \right) R^i_{xy} \\ & + c^i_{sha} \left((q_{sat,l} - q_{l,sha}) \frac{1}{\alpha^i_{k,s}} + (q_{l,sha} - q_c) \frac{1}{\alpha^i_{k,l}}) \right) R^i_{xy} \\ & + c^i_g f_{s,eq} R^i_{s,v} q_g + c^i_c \frac{f_{c,eq} R^i_{c,w} q_{sat,l}(T_v)}{\alpha^i(T_v)} + c^i_a R^i_{atm} q_{atm} \Big] \Big/ \\ & \Big[(1 - c^i_{sun} - c^i_{sha}) q_c - c^i_g (1 - f_{s,eq}) q_g - c^i_c (1 - f_{c,eq}) q_{sat,l}(T_v) \Big] \end{aligned} \tag{3.20}$$

Next, Equations 3.13 and 3.14 are used to determine steady state leaf water isotope ratios in the sunlit and shaded leaves ($R^i_{l,sun,s}$ and $R^i_{l,sha,s}$). The isotope ratios of the canopy-intercepted liquid water ($R^i_{c,w}$) and soil water vapor ($R^i_{s,v}$) are determined using R^{*i}_c and $f_{s,eq}$ and $f_{c,eq}$. Finally, Equations 3.8, 3.9, 3.10, 3.11 and 3.12 are used to determine the isotopic fluxes.

At this point, the isotope ratios of the leaf water, canopy-intercepted water, surface water vapor and canopy water vapor are all in isotopic steady state. It has been shown that including the Peclet effect in the calculation of isotope ratios in leaf water leads to better agreement with observations of leaf water isotope ratios [34, 20]. The latter authors also found that their steady state model with Peclet effect approximated the nonsteady state reasonably well [20]. In this spirit, the steady state leaf water isotope ratios are input to a diagnostic calculation of these ratios, accounting for the Peclet effect. In iCLM4, it is left as an option whether or not to use these diagnostic Peclet-included leaf water isotope ratios in the physics calculations or as purely a diagnostic quantity. Additionally, it has been consistently noted that the assumption of isotopic steady state is not always realized in the field [17, 20, 131]. Therefore, iCLM4 incorporates an optional nonsteady treatment of the leaf water isotope ratios, wherein the modeled value $R^i_{l,sun}$ is a weighted average between its value at the previous model time step and the newly calculated value in isotopic steady state, $R^i_{l,sun,s}$, and similarly for the shaded leaf water. This is implemented as

an exponential relaxation towards isotopic steady state.

While numerical calculations are performed with isotope ratios, results are reported in the standard "delta" notation. Delta values (in per mille, ‰) are calculated as

$$\delta_i = \left(\frac{R_i}{R_{SMOW}} - 1 \right) \times 1000‰ \tag{3.21}$$

where R_i is the sample molar ratio of abundances of the heavy isotope ($H_2^{18}O$ or HDO) to the light isotope ($H_2^{16}O$) and R_{SMOW} is this ratio for standard mean ocean water. Deuterium excess, d, is calculated as

$$d = \delta D - 8\delta^{18}O. \tag{3.22}$$

3.3 Validation

3.3.1 Tower Observations

A complete observational dataset for forcing and validation iCLM4 spans 145 days between May and September 2011, collected in an alpine forest northwest of Colorado Springs, Colorado, USA. The observational data consist of hydrological and meteorological data, collected from a 27.1 m tall tower in the Manitou Experimental Forest (MEF, $39^o06'02''$ N, $105^o06'05''$ W, 2286 m elevation). This is a needleleaf evergreen forest with minimal undergrowth, a canopy height of roughly 18.5 m and a site-averaged leaf area index of 1.9 [104, 28, 74]. The MEF site was selected for this study due to the availability of high quality previously validated hydrological and flux data. At the MEF site, air temperature (^{o}C), humidity (%), and pressure (mbar) were measured by a series of Vaisala HMT337 and WXT520 probes located at each inlet. CO_2 and humidity concentrations (μmol mol^{-1} and mmol mol^{-1}, respectively) were measured using a LiCor Li6262. Wind speed (m s^{-1}) was measured using a Gill R3-50 Sonic Anemometer. CO_2 and H_2O fluxes (μmol m^{-2} s^{-1} and mmol m^{-2} s^{-1}, respectively) were measured using a LiCor Li7000 infrared gas analyzer and Campbell CSAT-3 sonic anemometer. Eddy covariance methods were used to determine latent and sensible heat fluxes (W m^{-2}). A suite of Kipp and Zonen® CNR1 radiometers were used to measure upward and downward longwave and shortwave radiation (W m^{-2}). Observations of soil

water (m^3 m^{-3}) and temperature (K) were made at depths of 5, 50, 70, 100 and 150 cm using a Decagon® EC-5 dielectric probe and Campbell Scientific T107 thermistors, respectively. Further information regarding the experimental set-up can be found in [104, 8] and [28].

A second, more extensive observational dataset was collected at Boulder Atmospheric Observatory in Erie, Colorado, USA (BAO, $40^o03'00''$ N, $105^o00'14''$ W, 1584 m elevation). These data span May 2011 to September 2015. This is a semi-arid grassland, a canopy height of roughly 0.5 m. The BAO data were used for this study due to the availability of high quality continuous hydrological, flux and soil moisture isotopic data. At the BAO site, air temperature (^{o}C) and humidity (%) were measured by a series of Vaisala HMP155 probes. Wind speed (m s^{-1}), ambient pressure (hPa) and concentrations of CO_2 (μmol m^{-2} s^{-1}) and H_2O (mmol mol^{-1}) were measured using a Campbell Scientific EC150 open-path analyzer. Eddy covariance methods were used to determine latent and sensible heat fluxes (W m^{-2}). Upward and downward longwave and shortwave radiation (W M^{-2}) were measured using a suite of Kipp and Zonen CNR4 radiometers. Soil temperature and moisture measurements were gathered using Campbell Scientific 108-L and CS616 probes, respectively. Measurements of isotopic ratios of water vapor were made using a Picarro L2120-i water isotopic analyzer. Further details regarding the experimental set-up at BAO can be found in [69].

Between May 2011 and May 2012, isotope ratios of above-canopy water vapor and precipitation were missing from the forcing data. As a proxy, monthly measurements of isotope ratios in precipitation, collected in nearby Boulder, Colorado, USA, were used for this time period [60]. Isotope ratios of atmospheric water vapor were assumed to be in isotopic equilibrium with the precipitation, at the temperature measured by the tower observatory at BAO.

The simulations for MEF and BAO were both initialized using meteorological and hydrological data appropriate to the first date of the model run. Initial soil temperature and moisture profiles were linearly interpolated from the first date of observations (8 May 2011 for MEF and 11 May 2012 for BAO). Initial soil water isotopic profiles for each site were set constant at the deepest observed ratio from the earliest profile, and interpolated linearly to match the shallowest observed ratio from the same profile. For BAO, the May 2011 through May 2012 data is used as a spinup

year, and May 2012 through September 2015 model results and data are used for analysis.

3.3.1.1 Soil Moisture and Temperature

The modeled soil moisture profile and isotope ratios of δ^{18}O and d for MEF and BAO highlight model hydrology shortcomings and strengths (Figures 3.1 and 3.2). Observations of isotope ratios from these two sites are displayed as scatter points with the color of shading corresponding to the colors of the contours, which represent the modeled isotope ratio profiles. For the MEF site, observations of bulk soil moisture are similarly displayed as scatter points overlaid on the contours of the modeled soil moisture, due to the spatial sparseness of the observational data (four layers within the first meter of soil depth). The soil moisture data from BAO are displayed as a contour time series.

The effects of complex versus simple vegetation and landscape have a profound effect on the quality of soil moisture simulated by iCLM4. Note that the modeled bulk soil water profiles are the result of the hydrology native to non-isotopic CLM4, and the isotopic physics introduced in the present work has no impact on those results. Thus, the bulk water profiles provide an upper bound on how well one can reasonably expect the isotopic results to compare with observations. The soil moisture profile modeled at MEF is too dry early season (May through July 2011) by -0.10 mm^3 mm^{-3} on average, then the injection of late summer monsoonal moisture does not penetrate as deeply into the model soil column as seen in the observations, namely around 01 August 2011 (Figure 3.1a). A variety of spinup and initialization experiments were conducted in an effort to improve the control model representation of soil moisture at MEF, including a wide range of sensitivity tests for the moisture content of the initial soil profile, interpolating soil moisture data from the first observation using quadratic and spline fits, and starting the model from a state spun-up by forcing cyclically with the MEF data set for 30 years (with the soil moisture in an equilibrium state). None of these yielded significant improvement over Figure 3.1a, in which the initial model soil moisture state is linearly interpolated from the first set of soil moisture observations, and set equal to the top and bottom of the observations outside of the range of data. The modeled isotope

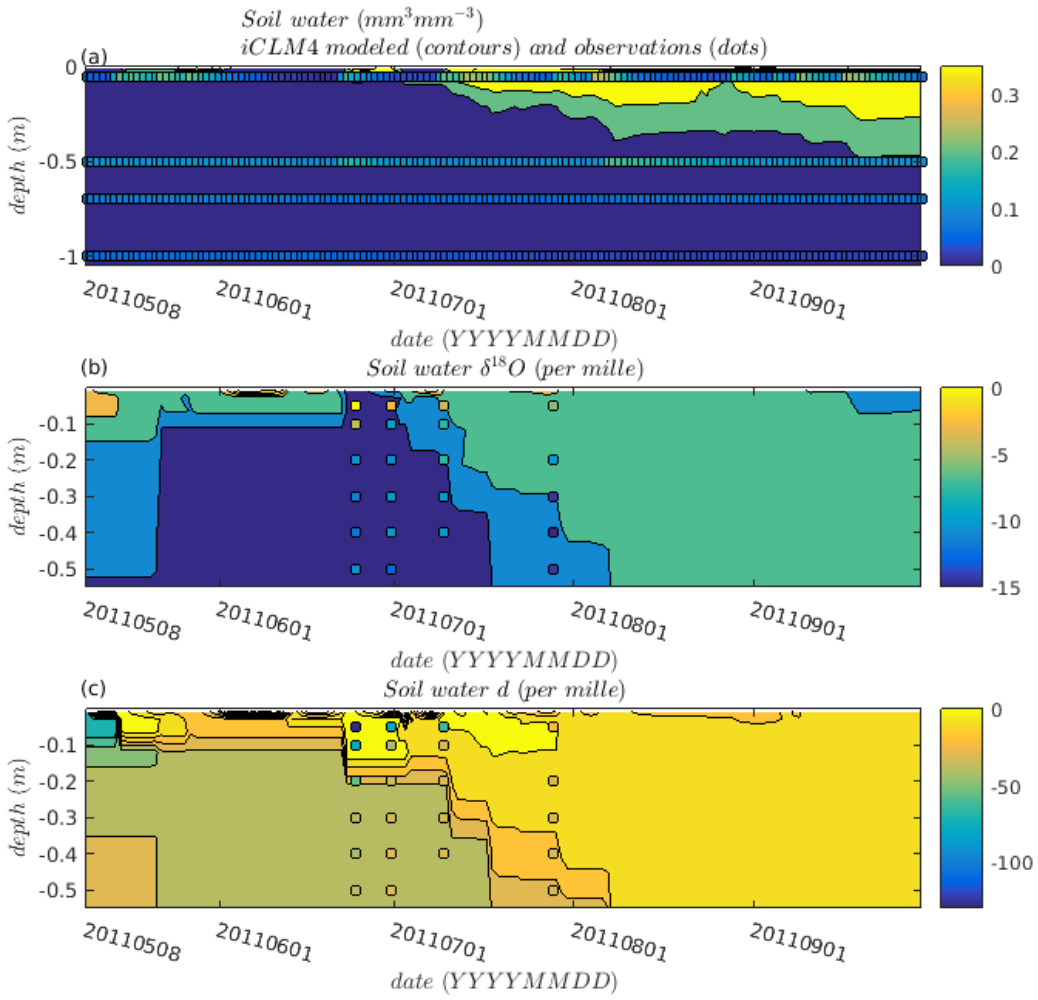

Figure 3.1: Comparison between modeled and observed (a) bulk soil water (mm^3 mm^{-3}) and its (b) isotope ratio $\delta^{18}O$ and (c) deuterium excess (d) for the MEF site.

ratio profiles in soil water at the MEF site are qualitatively good. Surface evaporative enrichment of $\delta^{18}O$ does not extend to 0.05 m depth, which is the depth of evaporative front seen in the observations (Figure 3.1b). This is consistent with the parameterization of evaporation in native CLM4, where evaporation is drawn from the top soil layer only, and an inherent limitation of the CLM4 model.

At BAO, the control modeled soil moisture profile shows much better agreement with the

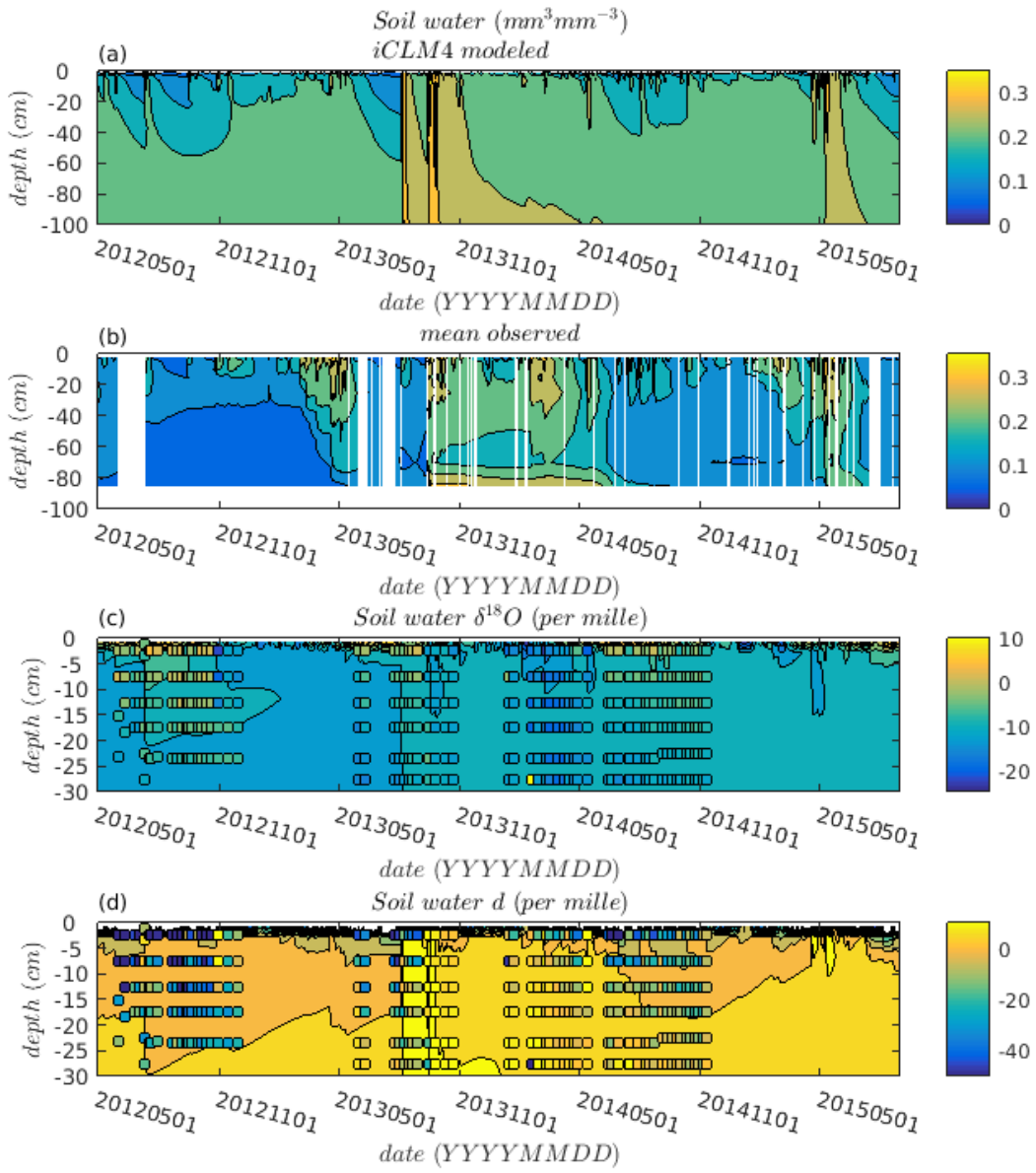

Figure 3.2: Comparison between modeled (a) and observed (b) bulk soil water (mm^3 mm^{-3}) and its isotope ratios of (c) $\delta^{18}O$ and (d) deuterium excess (d) at the BAO site.

observations than at the MEF site (Figure 3.2a and b). During summer and fall 2012, the modeled profile exhibits the summer drying and fall/winter wetting displayed by the observations. A similar pattern is seen in summer and fall 2013, and the injection of a large amount of moisture into

the soil profile is seen in September 2013, properly simulating the flooding event which occurred in the Colorado Front Range region at that time [142]. The modeled flooding event, however, does not inject moisture as deeply into the profile as the observations reflect, demonstrating a key shortcoming in the native CLM4 modeled soil moisture profile: the connectivity of the near-surface soil moisture to the deeper soils is not as strong as seen in the available data. This is consistent with other recent studies which have found that representation of the connectivity of the surface and deep soil moisture is a key feature for accurate soil moisture and flux modeling [43, 58].

MEF is a site with diverse vegetation (bare soil, needleleaf evergreen trees, broadleaf shrubs and C3 grasses) and landscape (large amounts of orographic relief in the foothills of the Rocky Mountains northwest of Colorado Springs, Colorado, USA). By contrast, the simple vegetation (predominantly C3 grasses, crops and bare soil) and landscape (little/no orographic relief) at BAO permit a much better match between modeled and observed soil moisture. The poor match in modeled soil water at MEF relative to the good match at BAO is attributed to these surface and vegetation heterogeneity effects.

That the shallow soil moisture signal does not percolate as deeply into the modeled profiles as seen in the observations is notable in both bulk soil water profiles, thus it is an issue native to non-isotopic CLM4. This issue leads to similar effects on the modeled isotopic moisture profiles. At BAO, summer enrichment and winter depletion of δ^{18}O are present and roughly match the measured isotope ratios in depth, but not in magnitude (Figure 3.2c). The modeled d in soil water at BAO was much too depleted in summers, but simulated winter ratios well (Figure 3.2d). At MEF, sampling of soil moisture isotope ratios was too sparse to yield any conclusive results. From these control simulations at MEF and BAO, it is clear that the modeled soil water isotope ratios are qualitatively accurate, but conclusive statements cannot be made because of the inherent errors in the bulk soil water hydrology in CLM4.

An experiment was conducted to evaluate the extent to which the native CLM4 soil hydrological scheme is to blame for the poor match in modeled soil water isotope ratios with observations. The BAO data set is used for this test because (1) the BAO site displays less heterogeneity than

MEF and (2) the BAO data set spans a wide time range, covering four full years. BAO soil moisture observations were assimilated into the model in the following way. At each model time step and soil layer (j) for which soil water data were available, the current modeled soil water content ($\theta_{old,j}$) value was relaxed exponentially toward the observed value for soil moisture ($\theta_{obs,j}$). At the bottom of the observed soil profile, the data were assimilated using a nudging approach with an e-folding time scale of one model timestep (τ_j = 30 minutes); at the top of the soil profile, the assimilation e-folding time scale was two weeks (τ_j = 14 days). In this way, precipitation is allowed to drive soil moisture dynamics closer to the surface, and additional constraint is provided in the deep soil, where it is most needed. Given the soil moisture content of soil layer j at the beginning of a time step, $\theta_{old,j}$, the observation of soil moisture in layer j at that time step, $\theta_{obs,j}$, the moisture-assimilated soil moisture, $\theta_{new,j}$ is given by

$$\theta_{new,j} = \theta_{obs,j} + (\theta_{old,j} - \theta_{obs,j}) \exp\left[-\frac{dt}{\tau_j}\right] \tag{3.23}$$

The choices for τ_j are motivated by the expected strong hydrological connectivity between surface soil moisture and the overlying atmospheric conditions (forcing data), so little assimilation is needed at the surface to connect it strongly with data. Similarly, weak connectivity between the atmosphere and deeper soils requires stronger assimilation of soil moisture, in the form of a shorter time scale of assimilation.

A zero flux boundary condition was imposed at the bottom of the iCLM4 soil column. Based on the change in water content of each soil layer ($\theta_{new,j} - \theta_{old,j}$), starting with the lowest layer (j_{max}), a flux between layers j and $j-1$ may be calculated. Using the "old" isotopic ratios of each soil layer, the isotopic transport during each assimilation step is calculated, and the water isotopic composition of each soil layer is updated.

As expected, the match between modeled and observed soil water content at BAO is excellent in the assimilation experiment (Figure 3.3a and b). Soil water δ^{18}O shows more seasonality at depth, which is in better agreement with observations, and shows a signal of roughly the correct magnitude (Figure 3.3c). In particular, the injection of summer 2013 monsoonal moisture of ~ -5‰ and the

winter 2013 through winter 2014 year are captured both qualitatively and quantitatively well. The evaporative enrichment during summer 2012 does not percolate as deeply into the soil as seen in the observations, but the duration of this signal is represented well in modeled δ^{18}O. During summer 2012, the modeled soil water d signal is not as depleted as seen in the observations (average high model bias of 19‰), indicative of too weak of a kinetic isotopic effect during soil evaporation, or not enough evapotranspiration (Figure 3.3d). In summer 2014, however, the modeled soil water d is good agreement with observations, with a mean bias of -1.18‰. The moisture-assimilated model simulates the d signal during and shortly after the Colorado Front Range flood event (fall 2013) quite well, injecting highly d-enriched moisture throughout the observed profile. This soil moisture data assimilation experiment demonstrates that a large portion of the errors seen in the soil water isotope ratios in the control model set-up are attributable to errors in the native CLM4 soil hydrology.

The modeled soil temperature profiles at MEF display qualitative agreement with the observed soil temperatures, including gradual warming at depth as the summer progresses into fall (Figure 3.4). The precise daily fluctuations in the deep soil temperatures are not reproduced in the model simulation. The late spring/early summer cooling in the top 50 cm of soil due to melting snow is reflected in the uppermost soil temperatures and marginally in the 50 cm layer temperatures. The modeled summer surface heating matches the observations in both magnitude and duration. At depth, however, the duration of the summer warming is not as long as was observed, and the warming and subsequent cooling is not as gradual. The modeled soil temperature profiles are a feature of native CLM4 and the deep soil mismatch is not attributed to the additional isotopic physics in iCLM4. Despite these quantitative shortcomings, when interpolated linearly to the observation depths, modeled soil temperature has a root-mean-squared error (RMSE) of 4.07 K.

At BAO, the match between modeled and observed soil temperatures is good, with a slightly lower RMSE of 3.03 K (Figure 3.5). More accurate modeling of the soil temperature at BAO than at MEF is attributed to the higher surface heterogeneity at MEF. Observed seasonal variation in soil temperature is reflected in the modeled temperature profiles. Rapid summer warming of the

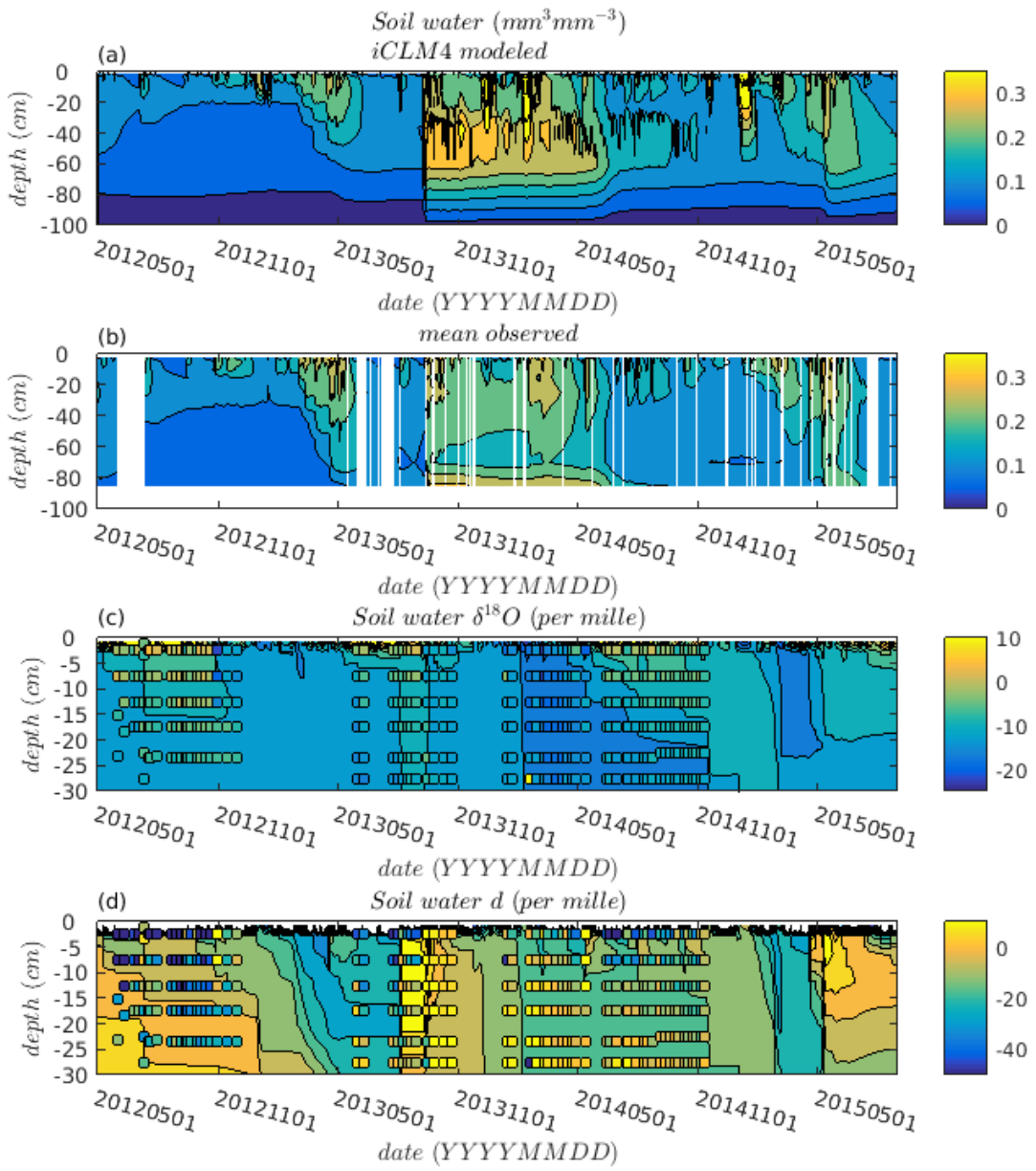

Figure 3.3: Comparison between modeled and observed bulk soil water (mm^3 mm^{-3}, (a) and (b), respectively) and its (c) isotope ratios $\delta^{18}O$ and (d) deuterium excess (d) for BAO, when soil moisture data is assimilated.

soil reaches depths of 60–80 cm, which is in agreement with the observations. Overall, the match is well within the uncertainties inherent in the modeled and observed soil temperatures, as will be

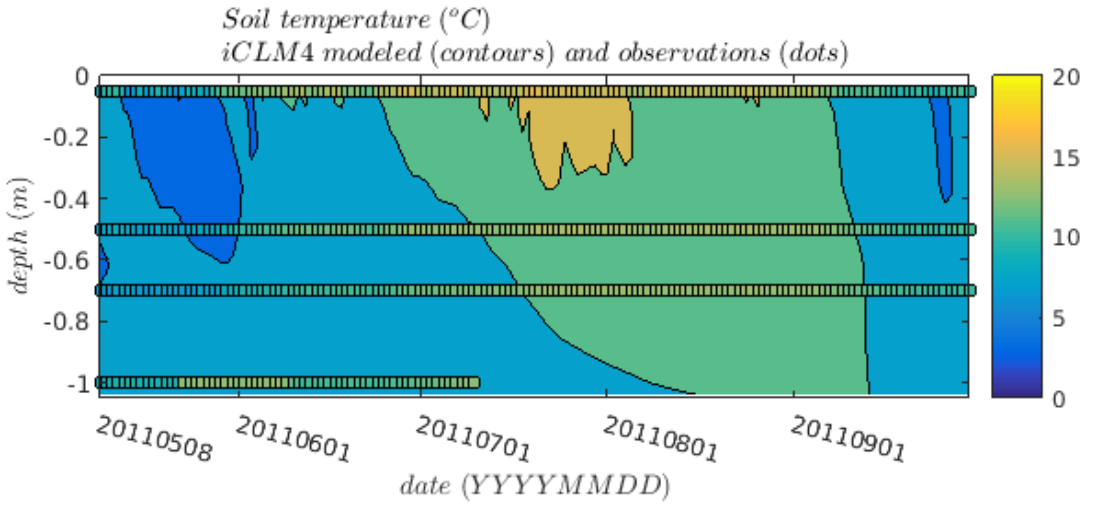

Figure 3.4: Comparison between modeled and observed soil temperature for MEF.

outlined in Section 4.3.2.

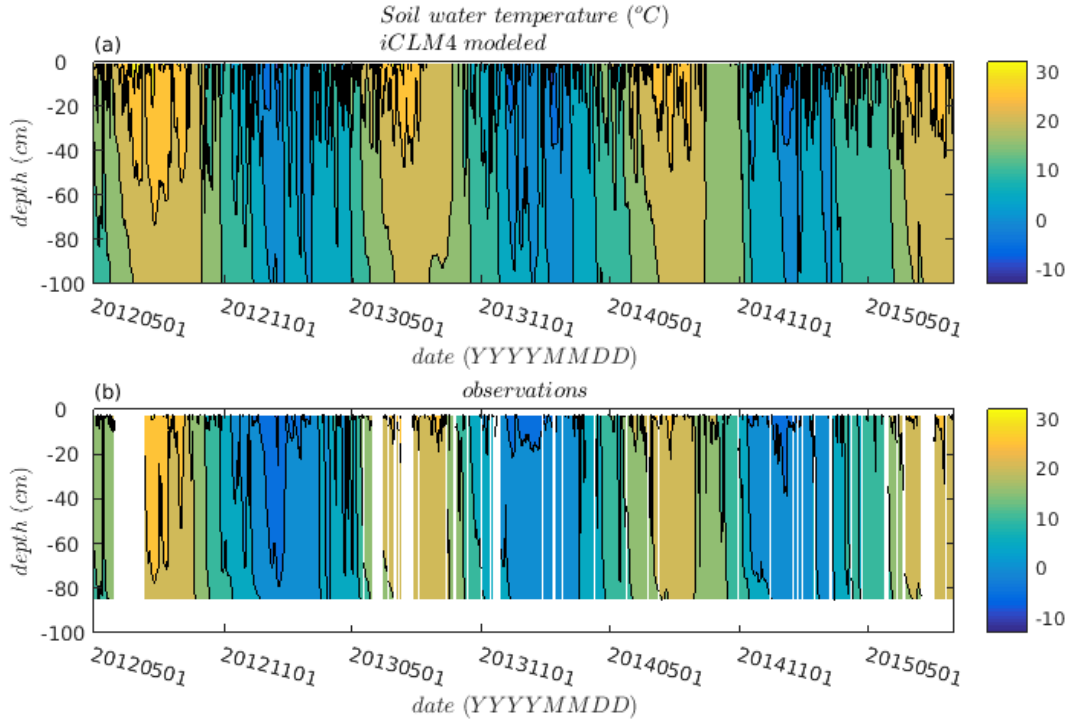

Figure 3.5: Comparison between modeled and observed soil temperature for BAO.

3.3.1.2 Latent and Sensible Heat Fluxes

Figure 3.6 shows the modeled surface latent heat and sensible heat fluxes plotted against the observations of these fluxes from MEF and BAO derived from eddy covariance, averaged on a daily time scale. A low model bias in latent heat flux for both sites is present (Figure 3.6a), with root-mean-squared error (RMSE) 22.6 W m^{-2}. Sensible heat flux displays a large high model bias for BAO and low bias for MEF, with RMSE 48.6 W m^{-2}. These results reflect model biases, or structural errors, which are inherent in the original, non-isotopic, version of CLM4. The incorporation of the stable water isotope hydrology into iCLM4 includes isotopic evapotranspiration terms which one cannot expect to have any less uncertainty than the bulk latent heat flux shown here.

3.3.1.3 Isotopic ET Estimates

While the total latent heat flux displays nontrivial biases for both sites (Figure 3.6), it is useful still to check the isotope ratios of the evapotranspiration (ET) flux against those derived from observations of humidity, isotope ratios of water vapor and Keeling plot techniques [70].

For MEF, the modeled isotope ratio of the ET flux of $H_2^{18}O$ is biased low by about 14‰, whereas at BAO the sign of this bias is reversed and is too high by 6.6‰. The isotope ratio of ET flux of d is biased high by 46‰ at MEF, and biased high at BAO by 11‰. These biases are calculated from daily averages of Keeling plot-derived isotope ratios of ET fluxes for observations and directly from model output (c.f. Section 3.2.2). These biases provide insight into systematic uncertainties in the parameterization of isotopic kinetic effects in iCLM4: The enriched (high) biases at BAO suggest that for this simple, flat, arid scrubgrass site, the kinetic effects of evapotranspiration in iCLM4 are too weak, yielding an ET flux which is too enriched in $\delta^{18}O$ and d. This is consistent with the low latent heat flux bias seen in Figure 3.6: by reducing the amount of ET flux, the isotopic separation experienced during evaporation is reduced, leaving more heavy isotopologues in the ET flux stream. By contrast, in the complicated needleleaf alpine forest at the MEF site, the kinetic effects of ET are too strong. A clear seasonal trend in the biases of the isotopic composition of ET

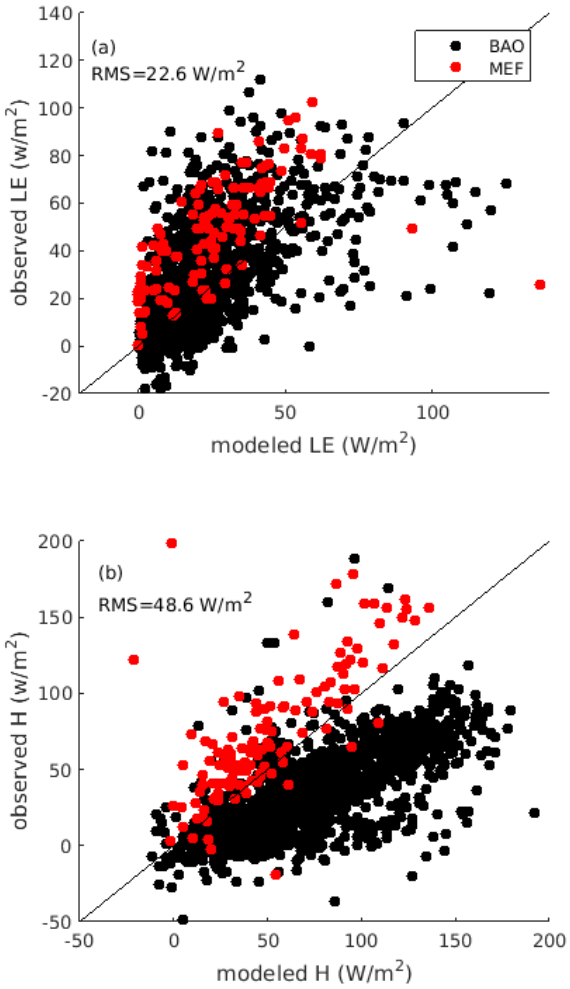

Figure 3.6: Comparison between modeled and observed (a) latent heat flux and (b) sensible heat flux for Manitou Experimental Observatory (MEF, in red) and Boulder Atmospheric Observatory (BAO, in black).

flux in iCLM4: The model is biased much higher relative to Keeling plot estimates of δ_{ET} in the winters than in the summer, spring or fall (Figure 3.8). The mean biases of all DJF results for $\delta^{18}O$ at BAO are +13.0‰, compared to a mean JJA bias of +1.50‰. This effect is reversed for deuterium excess, with a mean DJF bias of +9.50‰ and a mean JJA bias of +19.5‰. This is explained by low ET in DJF, thus the deuterium excess – which is strongly influenced by evapotranspiration and the

associated isotopic kinetic effects – is less influenced by the too strong kinetic effects in iCLM4 at BAO. The large biases present in the MEF simulation are attributable to the fact that the strong surface kinetic effect modeled by iCLM4 affects the quality of the simulation the most during the summer, when there is a large amount of total ET flux. For a single isotopic species, these results suggest that the summer season is better represented by iCLM4. There must be winter processes (e.g., snow melt or sublimation) which are not well-simulated during the winter, which leads to these errors in the isotope ratios of ET flux. These errors must be associated with poor model representation of these frozen snow and soil processes, the isotopic physics associated with them, or both. That the biases are opposite in sign for the two sites is indicative of uncertainty in the precise parameterization most appropriate for each site.

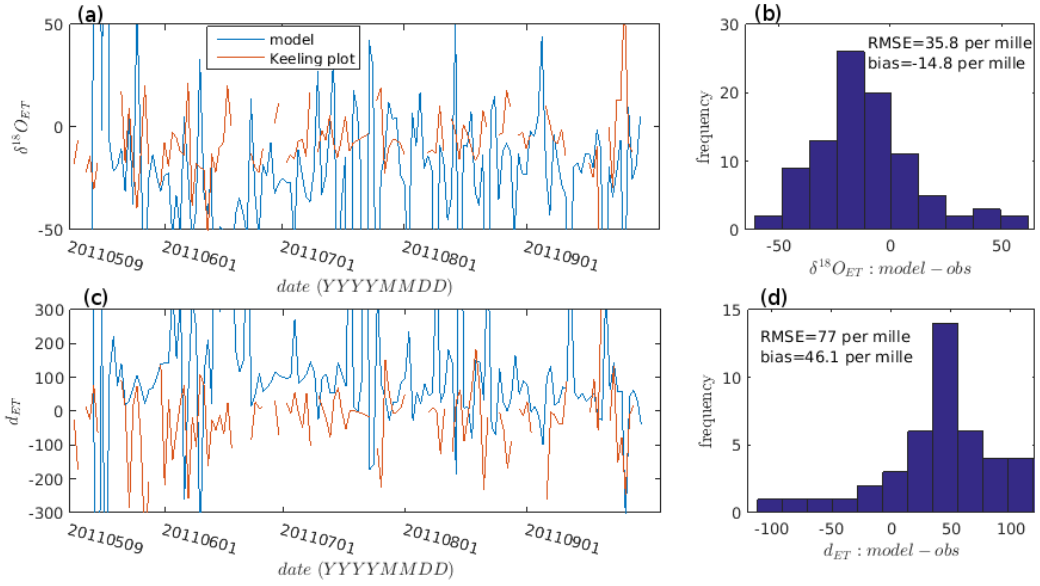

Figure 3.7: Time series ((a) δ^{18}O and (c) d) of modeled and Keeling plot estimates of the isotope ratio of ET source water for MEF, and histograms of the errors ((a) δ^{18}O and (c) d).

A network of ecosystem aerodynamic conductances effectively controls the net isotopic kinetic effect of evaporation and transpiration in iCLM4 (c.f. Section 3.2.2). Therefore, an examination of how best to optimize the parameterizations of these ecosystem conductances is of interest. This optimization is undertaken in Chapter 4, using the parameter calibration framework outlined and

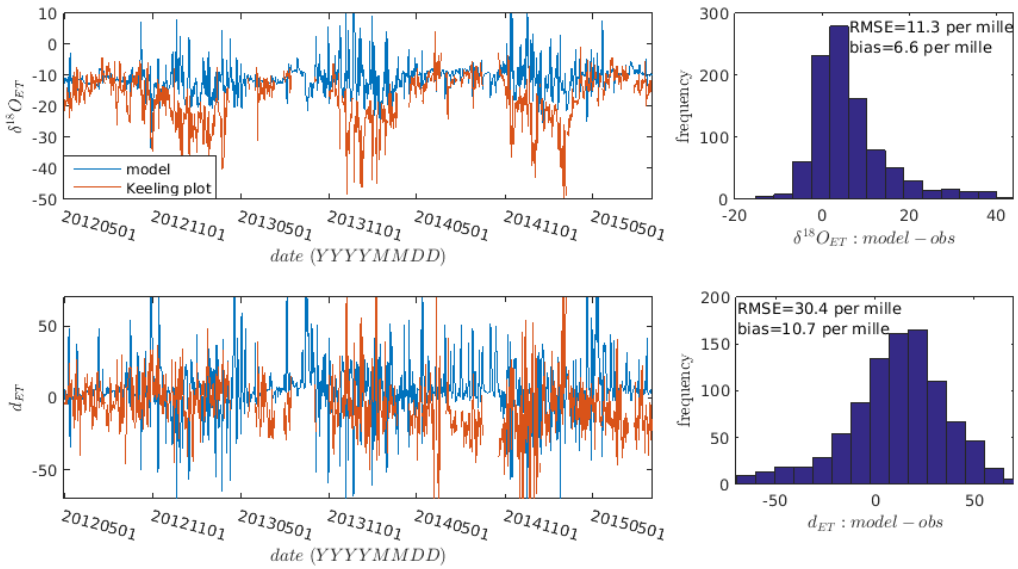

Figure 3.8: Time series of (a) δ^{18}O and (c) d of modeled and Keeling plot estimates of the isotope ratio of ET source water for BAO, and histograms of the errors ((b) δ^{18}O and (d) d).

demonstrated in Chapter 2 and the extensive site-level data set from BAO. Of interest at present, however, is a global investigation of the model sensitivity to individual isotopic kinetic effects' parameterizations used.

3.3.2 Global Comparisons

In a coupled model framework, the surface and subsurface runoff in CLM4 flows into the river model component of CESM, River Transport Model (RTM). Evapotranspiration from the land surface is transported into the atmospheric component of CESM, the Community Atmosphere Model, Version 5 (CAM5), and precipitates back to the land surface as rain or snow, and impacts the land surface through humidity connectivity with the vegetation canopy air-space as well. The isotopic land surface model detailed in the present work was coupled to isotope-enabled versions of RTM (iRTM) and the Community Atmosphere Model (iCAM5) [102]. iRTM is structured such that river outflow from iCLM4 is transported to oceans, preserving water isotope ratios. In the present work, the coupled land-river-atmosphere model is hereafter referred to as "iCESM," although it

should be noted there are CESM model components (ocean, sea ice and glaciers) which are not isotopically-enabled in this set-up. A control simulation for iCLM4, coupled to iRTM and iCAM5, ran from 1850 to 1975, with water pool isotope ratios initialized at values derived from long-term averages from the Global Network of Isotopes in Precipitation (GNIP) [60]. This control simulation was conducted using the parameterizations outlined in Section 3.2, at 2-degree resolution. A control sensitivity experiment was conducted using the same land surface kinetic fractionation set-up as the spinup simulation, including M78 for surface evaporation, non-steady-state transpiration and leaf water isotope ratios, and accounting for the Peclet effect. This control sensitivity experiment ran from 1975 to 2015 and is hereafter be referred to as "EC."

A series of experiments to investigate the sensitivity of the modeled climate system to the particular land surface isotope scheme used is desribed below, and summarized in Table 3.1. Each of the following simulations was branched from the spinup simulation at year 1975 and ran for 40 years with the modifications specified. The first 20 years of each experiment were discarded as spin-up from the control run; the last 20 years of each experiment were used for analysis, serving as an estimate of long-term average climate behavior. In the first experiment, all isotopic fractionation factors - both equilibrium and kinetic effects - were neglected (E00). In the second experiment, the kinetic fractionation factor associated with land surface evaporation was changed from M78 (the control) to follow the parameterization of MJ79 (ES). Finally, in light of the important role of the leaf litter layer resistance (Figure 3.3), an experiment is conducted in which this litter resistance is assigned a kinetic fractionation factor following M78 with $n = 1$ (ELI).

A pair of experiments were also conducted to evaluate the importance of including non-steady state leaf water isotopic processes and the Peclet effect. The Peclet effect describes the opposing tendencies within leaves, between evaporatively enriched water at evaporation sites within leaves and inflowing unenriched xylem water [34]. In one experiment here, the Peclet effect is neglected, and in the other, both the Peclet effect is neglected and only steady state leaf water isotope ratios were used in model physics (Equations 3.13 and 3.14). These experiments demonstrated little deviation from EC (which includes both non-steady state leaf effects and the Peclet effect) when

Table 3.1: Global Isotope-enabled Model Experiments.

	Equil. Frac.	Surf. Evap.	Canopy Evap.	Tran.	Non-steady Leaf	Peclet Effect	Leaf Litter
EC	yes	M78	M78	Eqs. 3.11-3.12	yes	yes	no
E00	no	no	no	steady	no	no	no
ES	yes	MJ79	M78	Eqs. 3.11-3.12	yes	yes	no
ELI	yes	M78	M78	steady	no	no	M78

considering long-term averages of isotope ratios. Therefore results for these leaf process sensitivity experiments are not shown. On shorter time scales (for example, analysis of a single monthly average of model output), however, it is likely that non-steady state leaf water isotope ratios and the Peclet effect play a greater role.

3.3.2.1 Global Network of Isotopes in Precipitation

In iCESM, modeled isotope ratios in precipitation may be compared to isotope ratios from the Global Network of Isotopes in Precipitation (GNIP) [60]. Additional stations were added from studies in the Maritime Continent [96, 80] region as well, in order to improve the spatial coverage of isotopic precipitation stations globally. Raw GNIP data were processed as in [17] to obtain a global climatology. Due to errors and biases in the atmospheric scheme (iCAM5), it is not expected that changing the land surface scheme for isotopic fractionation alone will remove errors relative to global isotope ratio data sets. These experiments do, however, allow for the evaluation of the importance of the land surface parameterizations by analyzing the coupled climate model response.

In its control sensitivity experiment, iCESM finds isotope ratios in precipitation which are too enriched in northern high latitudes and the Himalayas and too depleted in mid-latitudes and sourthern hemisphere (Figure 3.9). Neither weakening (ES) nor strengthening (ELI) the surface kinetic effects (EC) improve the low δ^{18}O bias; in fact, both experiments cause the bias to increase. By removing all surface kinetic effects, only minor improvements (positive effects) are made over Africa and Asia (Figure 3.9b). Note that in Figures 3.9 and 3.10, panel (a) shows the control model (EC) bias relative to GNIP, while panels (b), (c) and (d) show the sensitivity test results relative

to the control model. Control model deuterium excess tends to be biased low in high latitudes (both northern and southern) and biased high in the tropics and sub-tropics (Figure 3.10). Both experiments weakening the surface kinetic effect (E00 and ES) improve this negative d bias, and strengthening the surface kinetic effect has mixed effects. These biases result from the control model experimental setup (EC) and long-term averages from each GNIP station for which multiple observations are present. In Figures 3.9 and 3.10, the locations of GNIP observation sites are denoted with a diamond ($\diamond$).

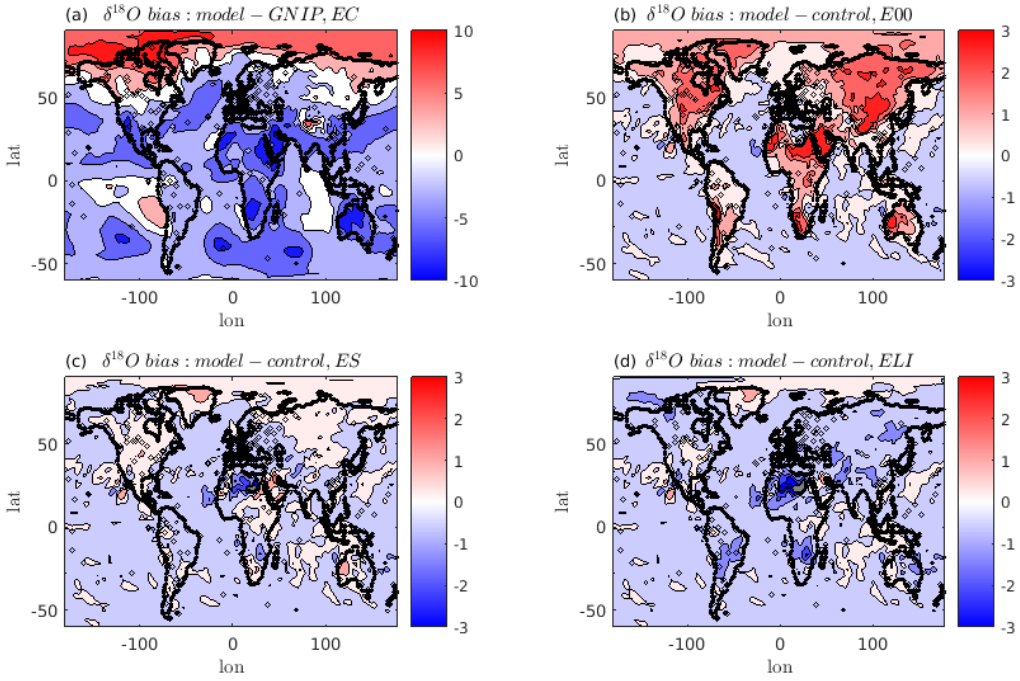

Figure 3.9: Biases of iCESM-modeled δ^{18}O of precipitation (a) relative to GNIP observations for EC, and relative to the control experiment for the sensitivity experiments (b) E00, (c) ES, and (d) ELI. Modeled values are from the 1975-2015 iCESM control run, averaging the isotope ratios from 2005-2015. Observed isotope ratios are the mean of all GNIP data for each observation site for which multiple observations are present. Locations of GNIP observation sites are denoted with a diamond ($\diamond$).

The global maps show a general trend of too depleted δ^{18}O in the northern high latitudes and too enriched δ^{18}O in the midlatitudes and tropics, as well as a high bias in d over land. Some of these biases and errors are associated with biases in atmospheric processes and evaporation over

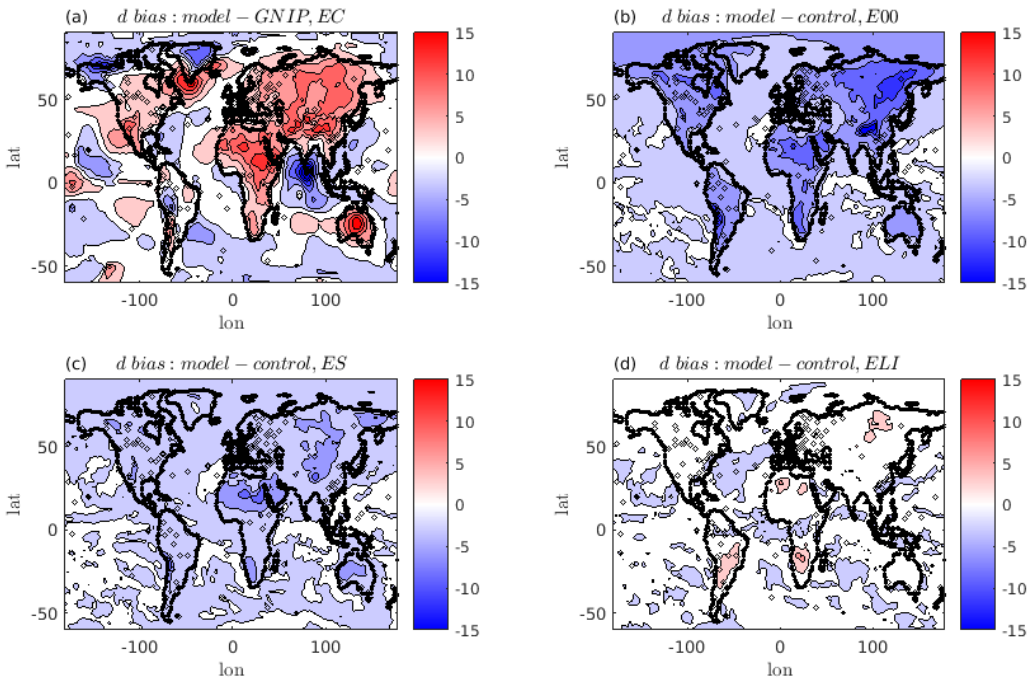

Figure 3.10: Biases of iCESM-modeled d of precipitation (a) relative to GNIP observations for EC, and relative to the control experiment for the sensitivity experiments (b) E00, (c) ES, and (d) ELI. Modeled values are from the 1975-2015 iCESM control run, averaging the isotope ratios from 2005-2015. Observed isotope ratios are the mean of all GNIP data for each observation site for which multiple observations are present. Locations of GNIP observation sites are denoted with a diamond ($\diamond$).

the ocean, and are not beyond the focus of the present work. By reducing the strength of the land surface isotopic effects, which in turn lowered the biases and RMSE relative to GNIP data, experiments E00 and ES appear to be optimal. It can be seen from Figure 3.11, however, that by completely neglecting all isotopic fractionations due to land surface processes, the d bias switches sign (E00, Figure 3.11). Therefore, the land surface isotopic parameterizations may be partially responsible for the iCESM model bias in precipitation isotope ratio relative to GNIP. Experiment E00 neglects physical processes (any isotopic fractionation at all) to compensate for a bias which must be present in the isotopic processes in the atmospheric model, iCAM5. Furthermore, the RMSE for E00 is only slightly reduced relative to a present, but weak, surface kinetic effect and full isotopic equilibrium fractionation effects considered (ES). Thus, it is unlikely that the specific

formulation of land surface isotopic processes is the sole cause of this d bias in precipitation.

The site-level experiments at MEF and BAO both showed high biases in modeled d_{ET} relative to Keeling plot estimates (Figures 3.7 and 3.8). Taken with the site-level results, these GNIP biases suggest that the surface evaporation kinetic effect modeled by M78 is too strong, and perhaps the weaker kinetic fractionation factor of MJ79 is more appropriate. At BAO, the soil moisture data assimilation experiment (Figure 3.3) resulted in a much lower soil water d than when the soil water was free-running. A lower soil moisture d would be consistent with a reduction in the d signal in ET flux to iCAM5, which would serve to reduce the positive d bias in precipitation isotope ratios. A set of model simulations similar to the experiments conducted here, but which assimilates global soil moisture data, is a necessary next step in order to assess how much of the precipitation d bias is due to innaccuracies in the soil hydrology of CLM4. It is clear from the BAO assimilation experiment, though, that errors in the bulk water not due to the isotopic parameterizations of iCAM5 and iCLM4 are to blame for some portion of this high d bias.

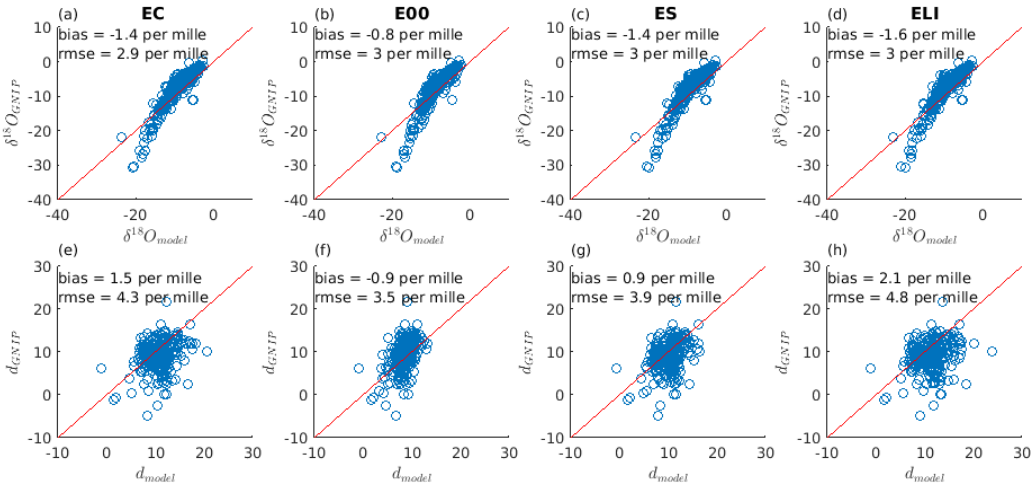

Figure 3.11: Comparison between iCESM-modeled and GNIP-observed δ^{18}O (top row) and deuterium excess, d (bottom row) for each sensitivity test: (a, e) EC, (b, f) E00, (c, g) ES, (d, h) ELI. Modeled values are from the 1850-2015 iCESM control run, averaging the 2005-2015 isotope ratios. Observed isotope ratios are the mean of all GNIP data for each observation site.

Despite this uncertainty, the fact that removing the isotopic kinetic separation due to evap-

oration entirely does not remove this precipitation isotope ratio bias relative to GNIP observations indicates an atmospheric process is at least partially the cause, in addition to the over-estimate of the surface kinetic separation. The surface kinetic effect is serving as a positive feedback on whatever process is leading to this high d bias is. At present, the root cause of this bias is unclear.

3.3.2.2 Global Network of Isotopes in Rivers

The control simulation yields iRTM output for isotope ratios of river flow throughout river basins, as well as inflow to oceans. The modeled river isotope ratios from iRTM represent an integrated ratio, incorporating iCLM4 surface and subsurface runoff along the flow path. This is commensurate with the isotope ratios measured by the Global Network of Isotopes in Rivers (GNIR) [62, 129]. The GNIR data span 1967-2015. Figure 3.12 shows the isotope ratios from the control simulation plotted against the GNIR data for δ^{18}O (top row) and deuterium excess, d (bottom row). Model output from 2005-2015 for each sensitivity test was averaged for each gridcell, and all available GNIR data were averaged for each observation site. The modeled ratios presented here have had the mean iCESM/GNIP precipitation isotope ratio bias subtracted out, to remove this potential source of systematic error (c.f., Figures 3.9 and 3.10). RMSE and mean iCESM bias are given in each panel of Figure 3.12. For both δ^{18}O and d, experiment E00 optimized RMSE by neglecting all isotopic fractionating effects. This supports the site results from BAO and GNIP, which indicated the surface kinetic isotopic effects from iCLM4 are too strong. Experiment ELI supplements the isotopic separation experienced during surface evaporation through the surface-to-canopy aerodynamic resistance with a kinetic separation through the leaf litter layer, which effectively raises the surface evaporative kinetic fractionation factor's strength. This experiment, however, produces river output isotope ratios which match GNIR worse than the control model, supporting the conclusion that stronger surface isotopic kinetic effects degrade model performance, while weaker kinetic effects enhance it.

The global maps of GNIR data superimposed on modeled river isotope ratios suggest that (1) there is little sensitivity on a global scale to the specific parameterizations for the kinetic effects used

in iCLM4, but (2) isotopic processes must not be discounted (Figures 3.13 and 3.14). Figures 3.13 and 3.14 have masked out numerous GNIR observation sites in North America, particular in the United State, due to their density covering all of the contour map below. The first point arises from the fact that, with the exception of E00, the rest of the sensitivity tests yield river isotope ratios which are similar on a macroscopic scale. The second point is based primarily on the GNIR site in northeastern Russia (approximately latitude 60^o N by longitude 130^o E). In experiment E00, this site is surrounded by a region where iCESM models river outflow as being too depleted relative to this station's observations. In the other experiments, with more realistic representations of the isotopic fractionations, while iCESM models the specific site of the GNIR station as too depleted, the macroscopic features are sensitive enough to the isotopic processes being altered that the adjacent gridcells are in agreement with these GNIR data. While the experiments which accounted for isotopic surface processes performed better than those that did not (E00), it is important to note that there is little sensitivity of modeled isotope ratios of river outflow to the specific parameterization used. This is due to river outflow being primarily controlled by deep soil water isotope ratios (subsurface runoff into rivers), which are largely insensitive to changes in the above-ground parameterizations. These isotope ratios are, however, sensitive to uncertainty in the bulk water (native CLM4) soil hydrology (c.f. Figure 3.3) [54].

3.3.2.3 Moisture Isotopes in the Biosphere and Atmosphere

Observations of isotope ratios of leaf and xylem water from the network of Moisture Isotopes in the Biosphere and Atmosphere (MIBA) offer constraint on the parameterizations of isotopic surface processes [61, 127]. Raw MIBA data for isotope ratios in xylem water and leaf water were averaged for each site to obtain a long-term average climatology. In instances where a site data set for a given country was missing latitude and longitude data, these isotope ratios were averaged in with the nearest site, as could be determined from the information given (i.e., type of vegetation or nearest municipal area). For modeled steady-state leaf water δ^{18}O, RMSE is optimized by the control model set-up (EC); for d, bias is also optimized by EC (Figure 3.15). That E00 yields

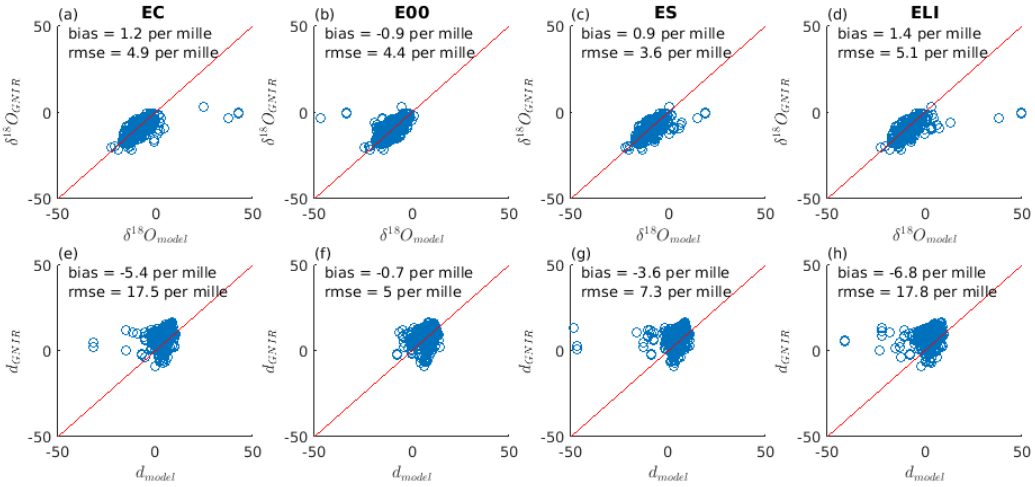

Figure 3.12: Comparison between iCESM-modeled and GNIR-observed δ^{18}O (top row) and deuterium excess, d (bottom row) for each sensitivity test: (a, e) EC, (b, f) E00, (c, g) ES, (d, h) ELI. Modeled values are from the 1850-2015 iCESM control run, averaging the 2005-2015 isotope ratios. Observed isotope ratios are the mean of all GNIR data for each observation site.

outstandingly poor match with MIBA leaf water isotope ratios demonstrates the importance of including isotopic processes within vegetation (non-steady state conditions and Peclet effect). That ES performs slightly worse than EC for δ^{18}O bias and RMSE in leaf water and d bias is in contrast to the GNIR and GNIP results, which suggests the surface evaporation kinetic fractionation factor in EC is too strong. The notion that this surface kinetic effect is parameterized reasonably in EC is further supported by experiment ELI, in which this kinetic factor is effectively strengthened by the leaf litter resistance, outperforming ES, according to model bias in leaf water isotope ratios relative to MIBA.

For xylem water δ^{18}O, both bias and RMSE are optimized by ELI (Figure 3.16). This would suggest a stronger kinetic effect for surface evaporation is required. On the other hand, xylem water d is optimized by experiment ES, which is in support of a weaker surface evaporative kinetic effect. This apparent conflict may be settled by noting in Figurethat experiments EC and ELI yield highly depleted d in desert and mountain regions, whereas the global d representation in ES is much more likely. ELI leads to an overly depleted representation of the Australian MIBA grid

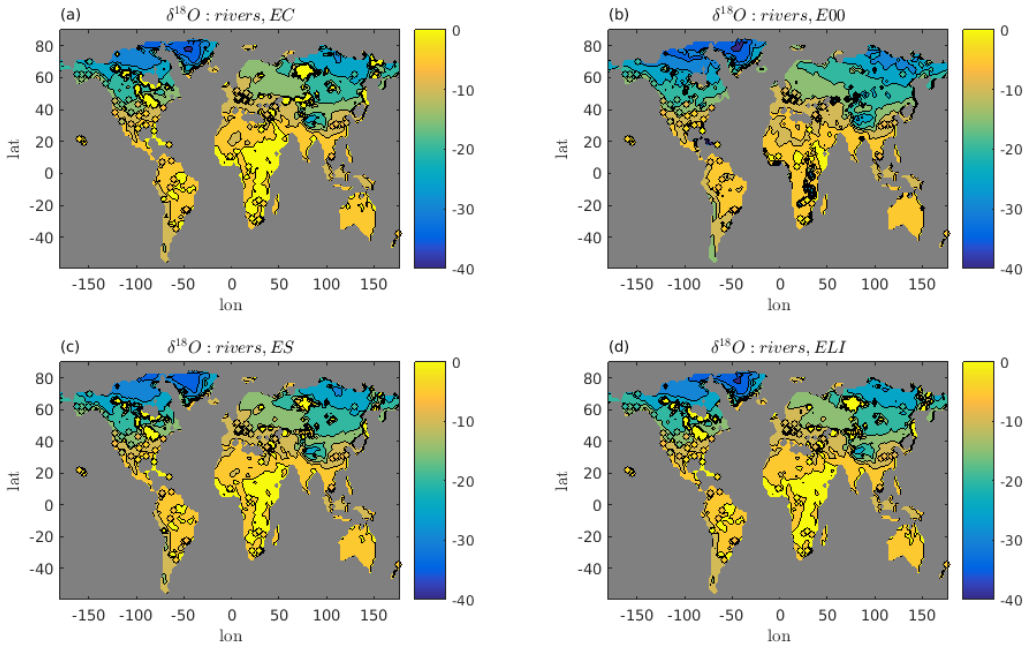

Figure 3.13: Comparison between iCESM-modeled and GNIR-observed δ^{18}O in river outflow for the sensitivity experiments: (a) EC, (b) E00, (c) ES, (d) ELI. Modeled values are from the 1975-2015 iCESM control run, averaging the isotope ratios from 2005-2015. Shaded dots represent observed isotope ratios, which are the mean of all GNIR data for each observation site.

point, so of the former four model set-ups, EC is the preferable choice. Furthermore, on the basis of these comparisons with MIBA data, it cannot be concluded that the model parameterizations in EC are inferior to ES; the allegedly overly-depleted d signal in mountain and desert areas in EC is not coincident with any actual MIBA data sites. These are regions with little vegetation, therefore vegetation isotope ratios provide little constraint. Indeed, river outflow and precipitation isotope ratios in these regions are also lacking, highlighting a need for additional data in desert and mountain regions, namely: northern Africa, western United States, central Australia, the Middle East, and the Himalayas.

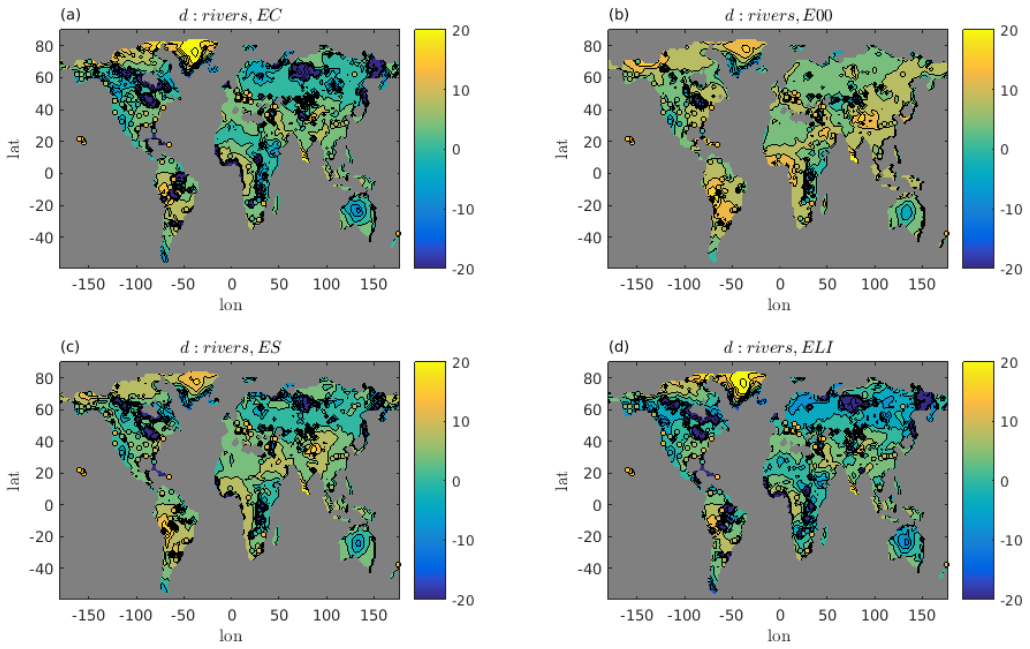

Figure 3.14: Comparison between iCESM-modeled and GNIR-observed deuterium excess in river outflow for the sensitivity experiments: (a) EC, (b) E00, (c) ES, (d) ELI. Modeled values are from the 1975-2015 iCESM control run, averaging the isotope ratios from 2005-2015. Shaded dots represent observed isotope ratios, which are the mean of all GNIR data for each observation site.

3.4 Summary and conclusions

We have outlined and implemented a tracer scheme, with an application in stable water isotope hydrology, in the Community Land Model version 4 (iCLM4). The iCLM4 model has been forced and validated with site-level observations from central Colorado, USA, as well as run in a coupled, isotope-enabled modeling framework (iCESM), and validated against global networks of observations of isotope ratios in precipitation, river outflow, and vegetation water.

The soil moisture validation simulations presented here using data from the Manitou Experimental Forest (needleleaf evergreen forest, MEF) and Boulder Atmospheric Observatory (semiarid grassland, BAO) demonstrated that CLM4 does not inject surface water deep enough into the soil column, which leads to errors in the isotope ratios of soil water. These, in turn, lead to inaccuracies in the xylem water which vegetation takes up through roots and later transpires. When soil mois-

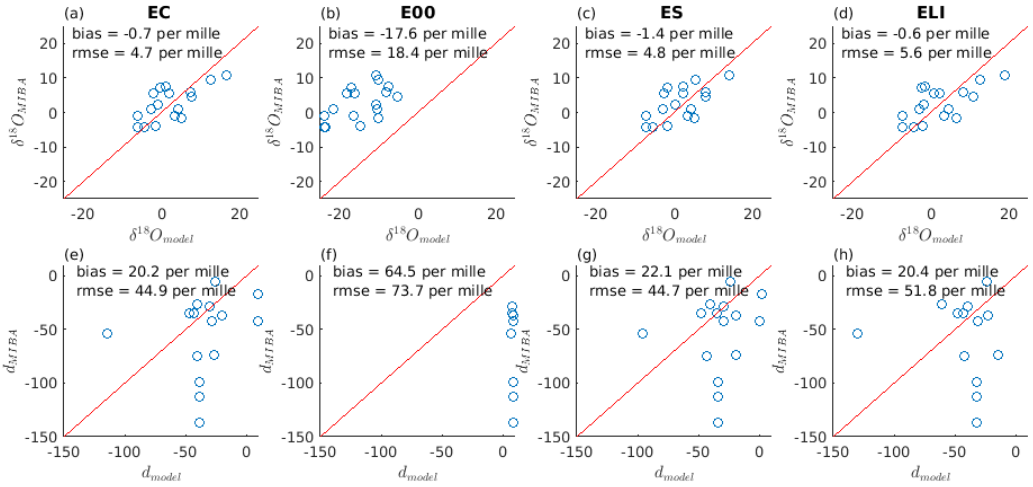

Figure 3.15: Comparison between iCESM-modeled and MIBA-observed leaf water δ^{18}O (top row) and deuterium excess, d (bottom row) for each sensitivity test: (a, e) EC, (b, f) E00, (c, g) ES, (d, h) ELI. Modeled values are from the 1850-2015 iCESM control run, averaging the 2005-2015 isotope ratios. Observed isotope ratios are the mean of all MIBA data for each observation site.

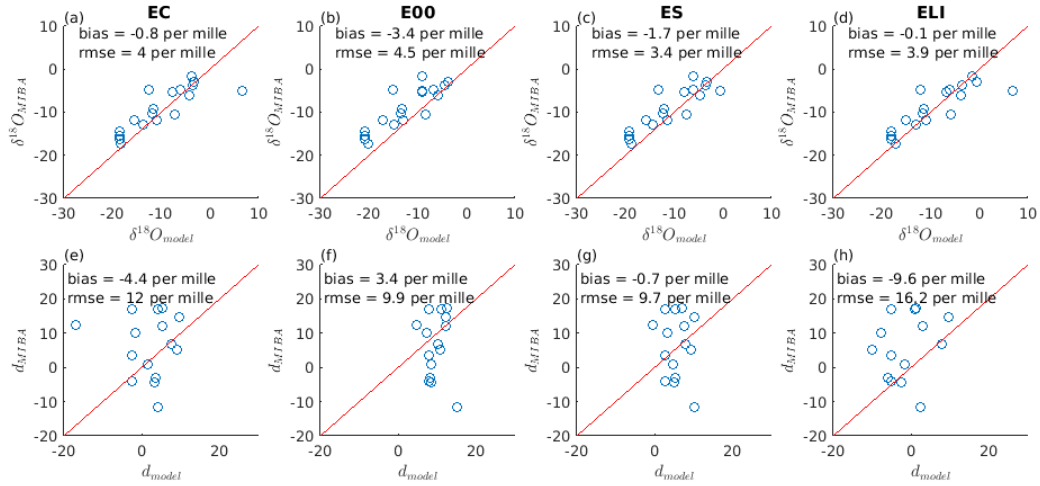

Figure 3.16: Comparison between iCESM-modeled and MIBA-observed xylem water δ^{18}O (top row) and deuterium excess, d (bottom row) for each sensitivity test: (a, e) EC, (b, f) E00, (c, g) ES, (d, h) ELI. Modeled values are from the 1850-2015 iCESM control run, averaging the 2005-2015 isotope ratios. Observed isotope ratios are the mean of all MIBA data for each observation site.

ture data from the BAO site were assimilated in the model simulation, nudging the native CLM4 soil hydrology into better agreement with observations, the modeled isotope ratios in soil water

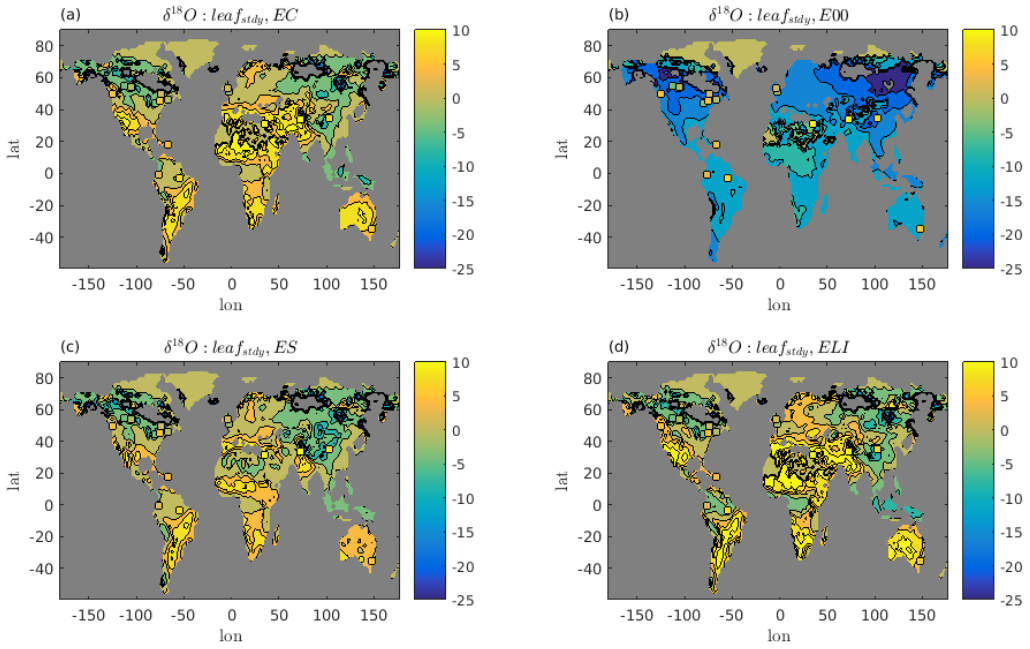

Figure 3.17: Comparison between iCESM-modeled and MIBA-observed leaf water δ^{18}O for the sensitivity experiments: (a) EC, (b) E00, (c) ES, (d) ELI. Modeled values are from the 1975-2015 iCESM control run, averaging the isotope ratios from 2005-2015. Shaded dots represent observed isotope ratios, which are the mean of all MIBA data for each observation site.

matched observations well. These experiments demonstrate level of accuracy the native hydrological scheme in CLM4 may reasonably attain, and show that a large portion of the error in iCLM4 estimates of soil water isotopic ratios stems from errors in original CLM4 bulk soil hydrological scheme. This conclusion is consistent with the findings of the model intercomparison study of [54], who found that variations in model soil hydrological scheme were a large source of intermodel variability. Data assimilation methods, such as the nudged forcing implemented in Section 3.3 or the statistical calibration method of Chapter 2, are viable options to improve model performance. Furthermore, the present work has demonstrated the ability of both of these methods to constrain models to more accurately represent observations of model state variables. Advantages of the nudging method include more reasonable model simulation at each time step, and direct assertion of a model-data match as opposed to the stochastic element of the statistical calibration method. Ad-

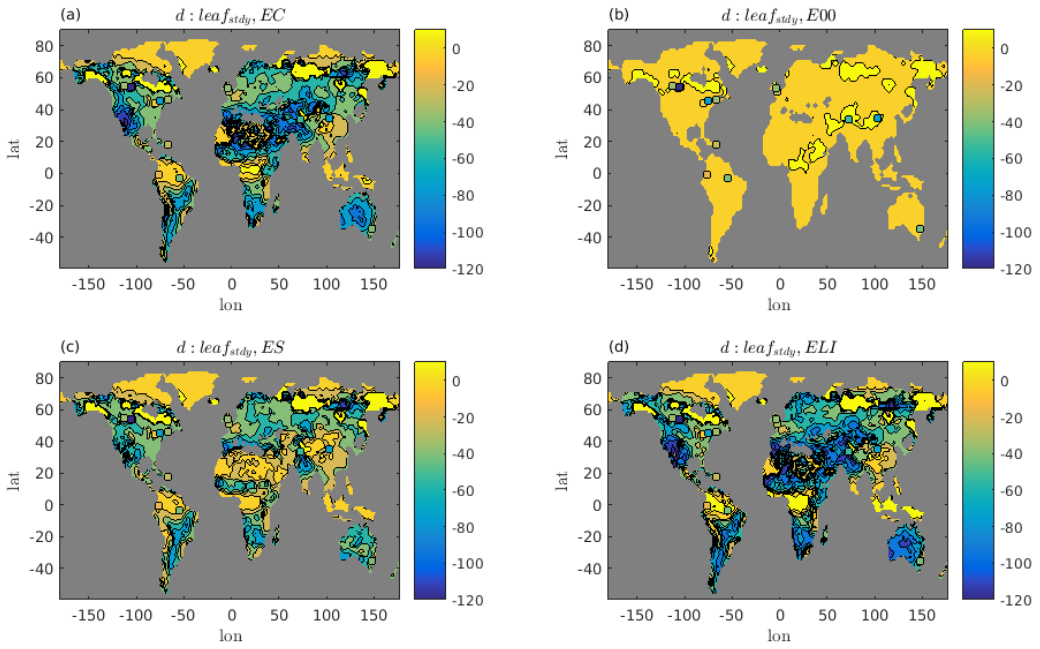

Figure 3.18: Comparison between iCESM-modeled and MIBA-observed leaf water deuterium excess for the sensitivity experiments: (a) EC, (b) E00, (c) ES, (d) ELI. Modeled values are from the 1975-2015 iCESM control run, averaging the isotope ratios from 2005-2015. Shaded dots represent observed isotope ratios, which are the mean of all MIBA data for each observation site.

vantages of the statistical calibration framework include flexibility and only enforcing a model-data match to within the uncertainty inherent in each.

These findings regarding the native CLM4 soil hydrology may be attributed to the manner in which modeled evaporation is removed from the soil. In CLM4, soil evaporation is removed from the top soil layer only, whereas recent studies have demonstrated that hydrological connectivity extends to $\sim$ 30 cm deep into the soil column [130, 43, 69]. Improvement in the CLM4 hydrology to better account for rapid water movement in upper soil layers (such in association with sub-surface vapor transport in arid and semi-arid environments) will likely result from setting the isotope ratio of evaporation source water equal to a mass-weighted average of the top $\sim$ 30 cm of soil moisture, as opposed to the top soil layer, as is done currently [92]. In this case, the isotopic kinetic fractionation factor from [92] would then be most appropriate for soil evaporation, and

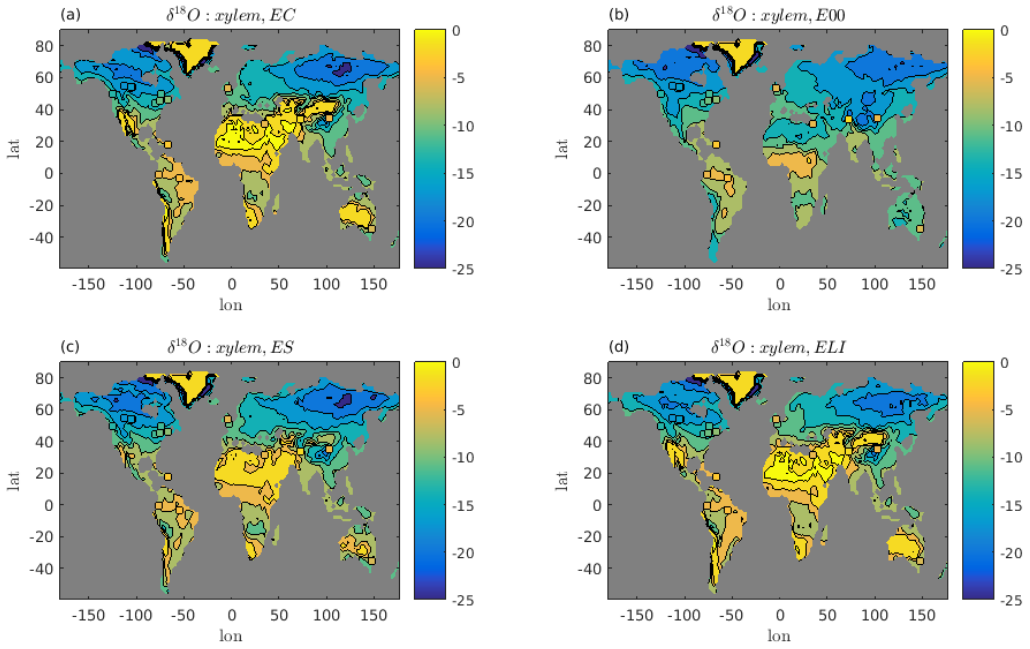

Figure 3.19: Comparison between iCESM-modeled and MIBA-observed xylem water δ^{18}O for the sensitivity experiments: (a) EC, (b) E00, (c) ES, (d) ELI. Modeled values are from the 1975-2015 iCESM control run, averaging the isotope ratios from 2005-2015. Shaded dots represent observed isotope ratios, which are the mean of all MIBA data for each observation site.

yield further improvement in the representation of land surface isotopic processes. Including model parameterizations for soil vapor diffusion will also yield a more realistic simulation of moisture transport through soils [120, 69].

From comparisons against long-term GNIP average isotope ratios in precipitation, the isotopically-enabled global climate system model (iCESM) simulates the isotopic composition of precipitation with a slightly low bias in δ^{18}O and slightly high bias in deuterium excess, d (-1.4‰ and 1.5‰, respectively; Figure 3.11). When surface evaporation kinetic effects were reduced (ES), or neglected entirely (E00), these biases were reduced. Comparisons against long-term river outflow isotope ratios (GNIR) showed a similar pattern, where the best match between model and observations was attained by reducing the strength of the isotopic kinetic fractionation factor associated with soil evaporation (Figure 3.12). The soil moisture data assimilation experiment using the BAO data set

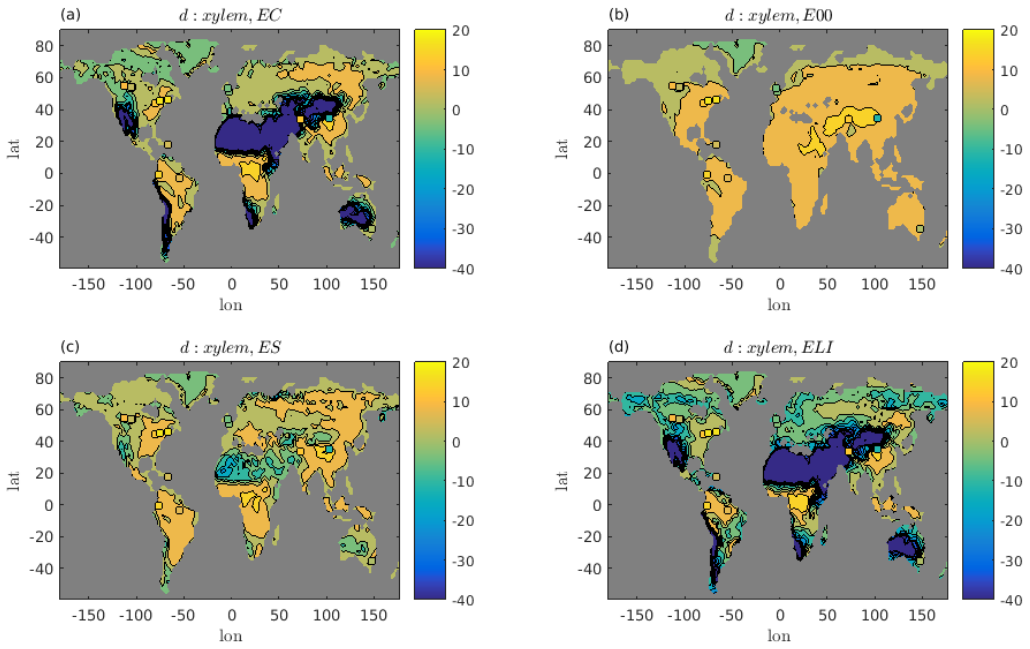

Figure 3.20: Comparison between iCESM-modeled and MIBA-observed xylem water deuterium excess for the sensitivity experiments: (a) EC, (b) E00, (c) ES, (d) ELI. Modeled values are from the 1975-2015 iCESM control run, averaging the isotope ratios from 2005-2015. Shaded dots represent observed isotope ratios, which are the mean of all MIBA data for each observation site.

demonstrated that errors in the modeled bulk soil hydrology lead to nontrivial errors in the isotopic signature of soil water (Figure 3.3). Soil water serves as ET source water, and excess soil water flows into rivers. Therefore, errors in the isotopic composition of soil water propagate into biases in the isotopic composition of precipitation and river outflow. Thus, there are two main components of uncertainty leading to the persistent biases in modeled isotope ratios of precipiation and river outflow: uncertainty in bulk soil water hydrology and uncertainty in the isotopic parameterizations used by iCLM4 and iCAM5. An opportunity to evaluate the non-linear dependence of soil water transport on the mean soil water state exists through assimilation of newly available global soil moisture remote sensing data products. These experiments would reduce uncertainty in the bulk soil water hydrological scheme as well as reduce the propagation of this uncertainty through the isotopic parameterizations in iCLM4 and iCAM5. Satellite-based soil moisture data products such

as the European Space Agency's Soil Moisture and Ocean Salinity (SMOS, [73]) and the National Aeronautics and Space Administration's Soil Moisture Active Passive (SMAP, [32]) programs offer viable options for assimilation data.

Leaf water isotope ratios compared favorably with vegetation data from the MIBA network in the control model set-up (EC, Figure 3.15). Xylem water δ^{18}O best matched MIBA observations in experiment ELI (bias = -0.1‰), but d was optimized by experiment ES (bias = -0.7‰). In spite of this apparent mismatch, it is clear that (1) iCESM is capable of reliably reproducing isotopic signals of δ^{18}O in vegetation moisture data, and (2) the experiment which neglected all isotopic fractionation factors (E00) matches leaf water data outstandingly poorly (Figures 3.17 and 3.18). The precise strength of the kinetic fractionation factor and imprecise native CLM4 soil hydrology (discussed above) are the causes of the conflicting optimal isotopic parameterizations. Imprecise soil hydrology leads to an isotopic signal in plant uptake which is biased, leading to inherent biases in xylem water isotope ratios. We conclude from these comparisons that the worst errors are incurred by failing to account for key land surface isotopic processes (E00, Figure 3.15), but the precise strengths of these processes remains unclear.

That the discrepency between model isotopic parameterizations which yield the best match with vegetation isotope ratio data is at least partially attributed to uncertainty in the strength of the kinetic fractionation factor is due to poor knowledge of the precise pathways by which moisture is transferred from surface, through the leaf litter layer, surface-to-canopy aerodynamic layer, and through the canopy air-space. While the canopy-scale kinetic effect was parameterized by [84], and implemented in iCLM4 as a kinetic fractionation factor for each individual ecosystem resistance term, the leaf litter resistance kinetic fractionation factor remains poorly known. For this reason, a study of these ecosystem resistance terms, in the manner of Chapter 2, should be conducted, but with the addition of stable water isotopic information. In this way, the strength of the isotopic kinetic effect may be constrained, as well as the soil hydrological performance, yielding a more accurate model representation of physical processes.

Chapter 4

The Impact of Water Isotopic Information in Partitioning Evapotranspiration in a Semiarid Grassland

4.1 Introduction

The partitioning of total evapotranspiration (ET) into contributions from surface evaporation (E) and plant transpiration (T) provides useful information regarding the hydrological and biogeochemical behaviors of ecosystems, but is notoriously difficult to constraint (see Chapter 2 for a more detailed discussion).

While no model is perfect, it has been shown that by utilizing observations of multiple land surface fluxes and at least one state variable, it is possible to achieve better-constrained and physically plausible parameter sets, as well as more reasonable model performance [90, 46, 47]. These data assimilation techniques have been successfully applied to land surface models to improve representation of snowmelt processes [105] and the carbon cycle [51, 138], as well as in the hydrological literature to optimize soil moisture parameters in a soil-vegetation-atmosphere-transfer model [25] and improve streamflow predictions and better explore hydrological parameter-spaces [97]. Recently, these model calibration methods have been used to successfully calibrate ecosystem resistances in a land surface model [135]. Chapter 2 and these examples point to statistical calibration as a desirable method for optimizing the exchanges of water and energy between land surface and atmosphere in a model, and thereby also optimize the isotopic exchanges and yield more robust estimates of ET partitioning. This calibrated estimate of transpiration fraction of total ET (f_T) was seen in Chapter 2 to be better constrained, as well as simply "better" in the sense that it is

an estimate informed by observational data.

Stable water isotope ratios ($^{18}O/^{16}O$ and $^{2}H/^{1}H$) offer another method to partition ET by leveraging the unique signatures of evaporation and transpiration on the isotopic makeup of ET source water [133, 141, 131, 98]. In this way, the isotope ratios of water pools within the canopy structure offer an instantaneous perspective on the balance of ET between E and T [140]. This partitioning approach is becoming more widespread due to the availability of databases of stable water isotopes and field-deployable laser-based isotope spectrometry instruments, but a number of methodological challenges remain. There are inherent uncertainties in obtaining measurements of water isotope ratios as well as in modeling the isotopic E and T flux streams [119, 44], and in a meta-analysis including both isotopic and non-isotopic partitioning approach, [115] found isotopic approaches to estimate a global average f_T which is higher than estimates from non-isotopic partitioning efforts. Furthermore, there is no standard method for obtaining ET partitioning estimates against which isotope-based partitioning may be compared. The same ecosystem resistances which facilitate the exchange of moisture and heat between land surface and atmosphere control the net ecosystem isotopic kinetic fractionation factor [36, 92, 84]. Thus, it is hypothesized that proper modeling of these resistances is critical for robust isotope-based ET partitioning estimates. The additional parameters required by a water isotopic hydrological scheme do not come without uncertainty (see Chapter 3 for further details), so there is a need to examine whether the benefits of water isotopic information in a modeling framework outweigh the additional parametric costs.

There are several challenges in developing assimilation methods for land surface models due to the large number of parameters, and many of these parameters are not well-constrained. The addition of a water isotope hydrological scheme to a land surface model adds constraint, from knowledge of the water isotope ratios of the various water pools, but also adds considerable complexity due to additional parameters relevant to the water isotopes. Furthermore, the physics captured by the model equations is simplified relative to the true processes at all scales, and may not be representative of the behaviors of the larger region. Similarly, there are distinct limitations in quality and availability of data which can be used to constrain land surface schemes, in particular, soil

water isotopic data. Therefore, there is a need to test the feasibility of using limited data sets with an efficient and scalable calibration scheme, which is easily generalized to a wide class of physical models. In the present study, it is shown that (1) the assimilation of tower meteorological and hydrological data with model output within a Bayesian calibration framework provides constraint on estimates of ecosystem resistances which facilitate the transport of heat and moisture, (2) these benefits are increased as a result of assimilating soil water isotopic data and estimates of ET flux water isotope ratios based on water vapor isotopic data for a single isotopic species, and (3) when a dataset for a second isotopic species is assimilated, the benefits decrease because of the complicated isotopic kinetic fractionating effect. As a consequence of (1), the informed estimates of the network of resistances lead to an estimate of the modeled ET partitioning, and practical estimates of the posterior uncertainties in model parameters as well as transpiration fraction emerge. As a consequence of (2) and (3), the assimilation of a single isotopic species is the optimal set-up to yield robust model-based estimates of isotopic ET partitioning.

For the case of a 4-year (ongoing) field campaign at a site in central Colorado, USA, a statistical approach is used to combine field observations and an isotopically-enabled land surface model to calibrate uncertain model parameters pertaining to the relative pathways by which moisture and heat are exchanged between land and atmosphere. These same parameters control the net ecosystem isotopic kinetic fractionation factor. Experiments are performed to quantify the benefits of calibrating using no isotopic information, as well as adding one or two datasets of stable water isotopic information to the calibration. Section 4.2 describes the calibration data set and stable water isotopically-enabled land surface model. A general statistical calibration framework and adaptive Metropolis-Hastings algorithm are described in Section 4.3.1, and the relevant model and observational uncertainties are reviewed in Section 4.3.2. It is shown in Section 4.4 that calibrating using no water isotopic information is good, calibrating using a single isotopic species is better, but calibrating using two isotopic species is worse. Finally, Section 4.5 discusses the practical implications of these results for future applications in partitioning ecosystem fluxes using water isotopic information.

4.2 Model and observational data

4.2.1 Observational data

The observational data consist of meteorological, hydrological and water isotopic data spanning from May 2011 to September 2015 in Erie, Colorado, USA, approximately 25 miles north of Denver, Colorado. Measurements were made from a 10 m tall tower at the Boulder Atmospheric Observatory site (BAO, $40^o03'00''$ N, $105^o00'14''$ W, 1584 m elevation). This is a semiarid grassland with minimal undergrowth and a canopy height of roughly 0.5 m. The BAO site was selected for this study due to the availability of high volume of stable water isotopic and previously validated hydrological and flux data .

At the BAO site, air temperature (^{o}C) and humidity (%) were measured by a series of Vaisala HMP155 probes. Wind speed (m s^{-1}), ambient pressure (hPa) and concentrations of CO_2 (μmol m^{-2} s^{-1}) and H_2O (mmol mol^{-1}) were measured using a Campbell Scientific EC150 open-path analyzer. Eddy covariance methods were used to determine latent and sensible heat fluxes (W m^{-2}). Upward and downward longwave and shortwave radiation (W M^{-2}) were measured using a suite of Kipp and Zonen CNR4 radiometers. Soil temperature and moisture measurements were gathered using Campbell Scientific 108-L and CS616 probes, respectively. Measurements of isotopic ratios of water vapor were made using a Picarro L2120-i water isotopic analyzer. Further details regarding the experimental set-up at BAO can be found in [69].

4.2.2 Land surface model

The model used is an isotopically-enabled version of the National Center for Atmospheric Research Community Land Model 4.0 (iCLM4) [136, 103]. CLM4 is a one-dimensional land surface model of the energy, momentum, water, and CO_2 exchanges between land and atmosphere, and it accounts for ecosystem dynamics, biophysical processes, hydrological processes, and biogeochemical processes. The Community Land Model is the land component of the Community Earth System Model (CESM) [59]. A brief overview of the physical parameterizations and water isotopic processes

which are relevant to the current study is given below, but the interested reader is directed to [103] for further details regarding CLM4 and to Chapter 3 and [136] for a more detailed overview of the stable water isotopic modifications in iCLM4.

Data fields needed as inputs to force iCLM4 include incident solar and longwave radiation, incident precipitation and its isotope ratios, atmospheric humidity and its isotope ratios, wind speed, and pressure and temperature at the surface. Surface data configured for the BAO site are soil texture, soil color, monthly leaf area index (LAI) and stem area index (SAI), vegetation composition, and albedo [128]. Previous studies suggest that using land surface fluxes and at least one state variable, it is possible to achieve better-constrained and physically plausible parameter sets, as well as more physically reasonable model performance [90, 46, 47]. Following this example, data used for the calibration included daily averages of latent heat flux, sensible heat flux, soil temperature and moisture. Additional water isotopic data used for calibration included the isotopic ratio of ET flux source water, calculated via a "Keeling plot" method [70], and observations of soil water isotopic ratios. Latent and sensible heat flux are key quantities in the exchange of moisture and heat between the land surface and atmosphere, and are readily observable by eddy covariance techniques [4]. Soil temperature and moisture are widely observed state variables, and characterize the energy and hydrological states of the ecosystem, offering attractive options to calibrate against.

Between May 2011 and May 2012, isotope ratios of above-canopy water vapor and precipitation were missing from the forcing data. As a proxy, monthly measurements of isotope ratios in precipitation, collected in nearby Boulder, Colorado, USA, were used for this time period [60]. Isotope ratios of atmospheric water vapor were assumed to be in isotopic equilibrium with the precipitation, at the temperature measured by the tower observatory at BAO. The simulations were initialized using meteorological and hydrological data appropriate to the first date of the model run (11 May 2011). Initial soil temperature and moisture profiles were linearly interpolated from the first date of observations. Initial soil water isotopic profiles for each site were set constant at the deepest observed ratio from the earliest profile, and interpolated linearly to match the shallowest observed ratio from the same profile. The May 2011 through May 2012 time period is used as a

spin-up year, and May 2012 through September 2015 model results and data are used for analysis.

To account for uncertainty in ecosystem turbulence characteristics, parameters selected for calibration are the aerodynamic resistances to moisture and heat transport between surface and vegetation air (f_g), and between vegetation and above-canopy air (f_a), through vegetation stomata (f_s), and through the leaf boundary layer (f_b). The calibration parameters are applied as multiplicative factors in the default resistance parameterizations. Stomatal resistance (m^2 s μmol) is calculated as

$$r_s = f_s \left(m \frac{A}{c_s} \frac{e_s}{e_i} P_{atm} + b \right)^{-1}, \tag{4.1}$$

where m is a parameter which depends on vegetation type, A is leaf photosynthesis (μmol CO_2 m^{-2} s^{-1}), c_s is the CO_2 partial pressure at the leaf surface (Pa), e_s is the vapor pressure at the leaf surface (Pa), e_i is the saturation vapor pressure (Pa) inside the leaf at the temperature of the vegetation, P_{atm} is the atmospheric pressure (Pa), and $b = 2000$ is the minimum stomatal conductance (μmol m^{-2} s^{-1}) when $A = 0$ [23, 103]. CLM4 separates leaves into sunlit and shaded portions, and Equation 4.1 applies to both $r_{s,sun}$ and $r_{s,sha}$. While the factors A, c_s, e_s and e_i are all modeled by CLM4, P_{atm} is given as atmospheric forcing and m and b are parameters which depend on vegetation type, and all have associated uncertainties. m and b, in particular, are known from laboratory experiments for various leaf types [5], though it remains less clear how these parameters scale up to the ecosystem scale considered by CLM4. From [23], Figure 2, it can be seen that the overall match is reasonable between measured and modeled stomatal conductance (the inverse of r_s), but parametric uncertainty in Equation 4.1 persists at the leaf scale, which will aggregate when integrated to ecosystem scale.

Leaf boundary layer resistance (m^2 s μmol) is parameterized as

$$r_b = f_b \frac{1}{C_v} \left(U / d_{leaf} \right)^{-1/2}, \tag{4.2}$$

where $C_v = 0.01$ m $s^{-1/2}$ is the turbulent transfer coefficient between the vegetation surface and canopy air, U (m s^{-1}) is the magnitude of the wind velocity incident on the leaves at a reference level, and d_{leaf} is the characteristic dimension of the leaves in the direction of the wind flow (taken

throughout CLM4 to be 0.04 m) [103]. U is modeled by CLM4 and C_v and d_{leaf} are parameters which CLM4 prescribes to all vegetation types, thus it is likely they do not describe any specific plant form particularly well, including those present at MEF.

The aerodynamic resistance to moisture and heat transfer between ground and canopy air (s m^{-1}) is as follows:

$$r'_{aw} = f_g \frac{1}{C_s U}, \tag{4.3}$$

where C_s is the turbulent transfer coefficient between the underlying soil and the canopy air, which is interpolated between values for bare soil and for dense canopy [143, 103]. While the formulations from [143] agree with observational data, these authors note that there are few measurements available which can constrain these values.

The aerodynamic resistance between the vegetation canopy and above-canopy air-spaces (s m^{-1}) is given by

$$r_{aw} = f_a \frac{q_{atm} - q_s}{q_* u_*}, \tag{4.4}$$

where u_* (m s^{-1}) is the friction velocity, q_* (kg kg^{-1}) is the moisture scale, q_{atm} (kg kg^{-1}) is the atmospheric specific humidity, and q_s (kg kg^{-1}) is the surface specific humidity [103]. u_* and q_* are derived from Monin-Obukhov similarity theory, and as noted by [144], their parameterizations were developed by separate groups using different data in different parameter regimes, and are intended for global modeling studies, with typical grid spacing much larger than the extent of the BAO tower footprint. Therefore it is not expected that these gridcell-scale parameters will compare favorably with the site-level data at the BAO site, further suggesting some tuning or calibration should be done.

These resistances are exchange parameters which define the way in which the energy and water balances at the surface behave, and determine the isotopic kinetic fractionation factor, yet the theory behind them is not well-established [92, 84]. [89] showed that realistic errors in the wind speed used to determine the aerodynamic resistances can lead to errors as large as 22% in modeled surface fluxes. Additionally, the isotopic kinetic fractionation factor – and therefore the

entire modeled water isotopic budget – depends critically on these ecosystem resistances. Therefore, estimating these parameters is important to accurately model the transfer processes. Simulation using calibrated parameters led to iCLM4 simulations which more closely match observations of latent heat flux, sensible heat flux, soil temperature and moisture, the isotopic ratio of the ET flux and soil water isotopic ratios as measured by the root-mean-squared error (RMSE). Therefore, this parameter set provides an illustrative demonstration of the benefits of this calibration approach but is by no means an exhaustive calibration of iCLM4.

4.2.3 ET partitioning

The portion of total ET which is attributable to transpiration, f_T, is a quantity which characterizes the hydrological and biogeochemical behaviors of an ecosystem, and the resistance parameters selected here partly control the balance of two critical moisture fluxes, evaporation and transpiration, in the model. Furthermore, the stable water isotopic approach to ET partitioning has in recent years been made feasible by the advent of field deployable isotopic analyzers. Each stable water isotopic species therefore yields an independent estimate of ET partitioning, which is denoted by $f_{T,^{18}O}$ or $f_{T,D}$. Therefore, the effects of the calibration on the modeled seasonal average transpiration fraction are analyzed. Here, a brief overview of the water isotopic method of ET partitioning is given.

The isotope partitioning approach uses a two end-member (evaporation and transpiration) mixing model, where R is the ratio of heavy to light isotope ($^{18}\mathrm{O}/^{16}\mathrm{O}$ or $^{2}\mathrm{H}/^{1}\mathrm{H}$) [140]:

$$f_{T,i} = \frac{R^i_{ET} - R^i_E}{R^i_T - R^i_E} \tag{4.5}$$

In Equation 4.5, i refers to isotopic species, R^i_{ET} is the isotopic ratio of the total ET flux, and R^i_E and R^i_T are the isotopic ratios of the individual evaporation and transpiration streams, respectively. These may be obtained directly from iCLM4 as model output [136], but in practice are rarely measured directly and when they are measured, there is no agreed upon standardized method. It is more illuminating, then, to use model output for water pool isotope ratios in conjunction with

a common offline ET partitioning model. Model output is internally consistent, so if this offline partitioning approach is robust, then using Equation 4.5 and model output as synthetic observations to obtain estimates of R^i_E, R^i_T and R^i_{ET} should yield results for $f_{T,i}$ which are in agreement with the direct model partitioning, f_T. The interested reader is referred to Chapter 3 for a detailed account of the physical and isotopic parameterizations which lead to iCLM4's estimates of R^i_E, R^i_T and R^i_{ET}.

4.2.3.1 ET partitioning using synthetic observations

In an offline setting, iCLM4 model output may be used as synthetic observations to obtain isotopic partitioning estimates ($f_{T,D}$ and $f_{T,^{18}O}$) in a manner analogous to what would be done in an field campaign. Using Equation 4.5, R^i_{ET} is calculated directly from model output for the ET flux and its isotope ratios (Section 3.2.2). This controls for a large portion of uncertainty in the ET partitioning estimates [44]. It might be argued that this method will therefore yield an unrealistically low uncertainty in estimates of isotope-based partitioning, but the focus of the present work is to quantify the value of isotopic information, not to quantify uncertainty in R^i_{ET}, which was solved by [44]. Indeed, as Section 4.3.2 will show, the isotope-based estimates of $f_{T,i}$ derived in the present work fully account for uncertainty in R^i_{ET}.

The isotope ratios of the evaporation and transpiration fluxes may be estimated following equations from [24] as

$$R^i_{E\ or\ T} = \alpha^i_k \left(\frac{\frac{1}{\alpha^i(T_{source})} R^i_{source} q_{sat}(T_{source}) - R^i_c q_c}{q_{sat}(T_{source}) - q_c} \right) . \tag{4.6}$$

In Equation 4.6, T_{source} is the temperature of the surface for evaporation or the vegetation temperature for transpiration; α^i is the temperature-dependent equilibrium fractionation factor [56]; R^i_{source} is the isotope ratio of source water, surface water for evaporation or leaf water for transpiration; q_{sat} is the saturation vapor pressure at the temperature of the source water; q_c is the canopy vapor pressure; α^i_k is the canopy-scale kinetic fractionation factor [36, 92, 84], which may be calculated from iCLM4 output for the ecosystem resistance terms. For the BAO site, this net kinetic effect for

surface evaporation is calculated from the leaf litter layer resistance (r_{litter}), the surface-to-canopy aerodynamic resistance (r'_{aw}), the canopy-to-above canopy aerodynamic resistance (r_{aw}), and their respective kinetic fractionation factors ($\alpha^i_{k,litter}$, $\alpha^i_{k,g}$, and $\alpha^i_{k,a}$) (Equation 4.7). For surface evaporation, these resistances are the most appropriate choice for the resistance-weighting method for determining a net kinetic fractionation factor.

$$\alpha^i_k = \frac{\alpha^i_{k,litter} r_{litter} + \alpha^i_{k,g} r'_{aw} + \alpha^i_{k,a} r_{aw}}{r_{litter} + r'_{aw} + r_{aw}} \tag{4.7}$$

It should be noted that Equation 4.6 makes the common assumption that relative humidity $h \approx q_c/q_{sat}(T_{source})$, whereas it is not necessarily true that the humidities of the source water and canopy vapor are commensurate. It is also important to note that this experiment in using iCLM4 model output as synthetic observations to assess the fidelity with which Equations 4.5 and 4.6 leverage stable water isotopic ratios to partitioning ET also makes the common assumption that evaporation of canopy-intercepted water plays a negligible role in total ET and the isotope ratios of its component fluxes. Examining the validity of this assumption is beyond the scope of the present work, because the focus here is on whether common field practices, when synthesized with "perfect observations," have the capacity to yield results which match the known partitioning f_T, the directly modeled, isotope-independent partitioning. The validity of the assumption of negligible canopy evaporation will be the subject of a follow-up study, however.

While numerical calculations are performed with isotope ratios, results are reported in the standard "delta" notation. Delta values (in per mille, ‰) are calculated as

$$\delta_i = \left(\frac{R_i}{R_{SMOW}} - 1 \right) \times 1000‰ \tag{4.8}$$

where R_i is the sample molar ratio of abundances of the heavy isotope ($H_2^{18}O$ or HDO) to the light isotope ($H_2^{16}O$) and R_{SMOW} is this ratio for standard mean ocean water. Deuterium excess, d, is calculated as

$$d = \delta D - 8\delta^{18}O. \tag{4.9}$$

4.2.3.2 Model experimental design

In this study, we compare several estimates of transpiration fraction, in several model calibration data scenarios. The focus of this study is to evaluate the additional constraint offered by assimilating water isotopic information. Therefore, this study consists of a set of three experiments. In the first, only latent heat flux, sensible heat flux, soil temperature and soil moisture data are assimilated; no isotopic information is used in the calibration. This experiment is hereafter referred to as "E1." In the second experiment (E2), data from a single water isotopic species (HDO) is introduced to the calibration. In the final experiment (E3), data from a second species ($H_2^{18}O$) is also assimilated. The Kullback-Leibler (KL) divergence between two distributions P and Q is defined to be

$$D_{KL}(P\|Q) = \sum_i p_i \log\left(p_i/q_i\right) \tag{4.10}$$

with units of nats when using the natural logarithm [78].

In the context of KL divergence, let $\Pi^j_{E_i}$ denote the joint posterior distribution of the model parameters and f_T for experiment E1, E2, or E3, where $j \in 1, 2, \ldots, 5$ indexes the four model parameters and f_T. Also, let $\mathcal{E}^k_{E_i}$ denote the joint distribution of errors in the modeled calibration data fields relative to the observations, where $k \in 1, 2, \ldots, 8$ indexes the eight calibration data fields, and $i \in \{1, 2, 3, control\}$ denotes the calibration experiment or the control simulation. We define the total KL divergence of the posterior model parameters and f_T of experiment Ei_2 from Ei_1 as

$$D_{KL}\left(\Pi_{E_{i_1}}\|\Pi_{E_{i_2}}\right) = \sum_j D_{KL}\left(\Pi^j_{E_{i_1}}\|\Pi^j_{E_{i_2}}\right) \ , \tag{4.11}$$

where $i_1, i_2 \in \{1, 2, 3\}$. This provides a metric to measure the relative entropy of the posterior distributions of model parameters and f_T between the calibration experiments performed here. Similarly, the total KL divergence based on the distributions of errors in the modeled calibration data fields of experiment Ei_2 from Ei_1 is defined as

$$D_{KL}\left(\mathcal{E}_{E_{i_1}}\|\mathcal{E}_{E_{i_2}}\right) = \sum_k D_{KL}\left(\mathcal{E}^k_{E_{i_1}}\|\mathcal{E}^k_{E_{i_2}}\right) \ , \tag{4.12}$$

where $i_1, i_2 \in \{1, 2, 3, control\}$. While $D_{KL}\left(\Pi_{E_{i_1}} \| \Pi_{E_{i_2}}\right) = \sum_j D_{KL}\left(\Pi^j_{E_{i_1}} \| \Pi^j_{E_{i_2}}\right)$ is a good metric to quantify the constraint offered by the data on model parameters and quantities of interest, $D_{KL}\left(\mathcal{E}_{E_{i_1}} \| \mathcal{E}_{E_{i_2}}\right)$ serves to quantify the reduction in uncertainty of model output for the calibration data fields, which is also desirable. The KL divergence was selected as the measure of information content for the present work in light of its widespread use in previous studies of model intercomparisons [75, 121], model-data comparisons [14], and quantification of information content in models and data [99, 137].

For a given set of calibration data, there are three model-derived estimates of transpiration fraction: (1) directly modeled, non-isotopic transpiration fraction (f_T); (2) transpiration fraction from Equation 4.5 using HDO ($f_{T,D}$) and (3) $H_2^{18}O$ ($f_{T,^{18}O}$). If the isotopic parameterizations in iCLM4 and Section 4.2.3.1 were perfect, then $f_T = f_{T,D} = f_{T,^{18}O}$. It should be noted that iCLM4 model output is all internally consistent, so using iCLM4 output as synthetic observations, input into the partitioning method of Section 4.2.3.1, is akin to having perfect observations. Furthermore, in the model simulation, only f_T is the "true" partitioning; all iCLM4 output is consistent with this value, and if the method of Section 4.2.3.1 yields $f_{T,i}$ which do not match f_T, the issue lies in the simplifications in the isotopic parameterizations of Section 4.2.3.1, relative to those of [136]. The latter implements a more detailed accounting of isotopic processes because it is simpler to account for these in a model than it is to measure their effects in the field. It is hypothesized that the isotopic kinetic fractionation factor is the largest source of uncertainty in the isotope-based partitioning method, and consequently that calibration of the ecosystem resistances will lead to a more realistic simulation of isotope ratios of ecosystem water pools, which will in turn yield isotope-based partitioning estimates which agree better with directly modeled partitioning.

4.2.4 Model performance and the need for a statistical approach

Figures 4.1 and 4.2 compare CLM4 output for latent heat flux, sensible heat flux, soil temperature, soil moisture, water isotope ratios of ET flux and soil water isotope ratios to observational data, averaged on a daily time scale. The gray shaded regions denote a ± 1 observational uncer-

tainty region around the observations. The model represents these physical processes qualitatively well, as peaks and troughs in the data are present in the modeled values. Latent heat flux is simulated well in the control model set-up, with a mean bias of -2.00 W m^{-2}. Soil water $\delta^{18}O$ is also simulated accurately, on average, with a mean bias of -0.439 ‰. However, the error histograms are not all centered at zero, indicative of model bias, or structural errors (Figure 4.3). The distribution of sensible heat flux errors is centered around 26.1 W m^{-2}; soil temperature errors are centered at a warm model bias of 2.10 K; and soil moisture errors are biased high by 0.0485 mm^3 mm^{-3}. Large biases are present in the model output of the isotope ratios of ET flux and soil water isotope ratios, with the exception of soil water $\delta^{18}O$. Isotope ratios of $H_2^{18}O$ and HDO in ET flux are biased high by 6.78 ‰ and 61.0 ‰, respectively. In soil water, δD is biased slightly high, by 14.8 ‰. That the model biases in soil water isotope ratios are much lower than the biases in the isotope ratios of ET flux indicates that the isotopic processes responsible for transferring soil moisture to ET flux are the cause of this discrepancy. It is unclear that these biases are attributable to model parameter choice, or are an inherent limitation of iCLM4 that stems from the use of approximate equations, thus motivating the need to account for these model biases. RMSE for the uncalibrated modeled latent heat flux, sensible heat flux, soil temperature and soil moisture are 21.3 W m^{-2}, 36.2 W m^{-2}, 2.94 K and 0.0745 mm^3 mm^{-3}, respectively. RMSE for the uncalibrated water isotopic ratios of ET flux are 11.8 ‰ for $H_2^{18}O$ and 84.4 ‰ for HDO, and RMSE for the uncalibrated isotopic ratios of soil water are 5.11 ‰ for $H_2^{18}O$ and 33.1 ‰ for HDO.

4.3 Calibration framework

4.3.1 Model calibration

Within a statistical framework, the iCLM4 model output is related to various types of observational data. Using a Bayesian approach, prior distributions on the model parameters are joined with the iCLM4 solution and assimilated field data, leading to posterior distributions that represent uncertainty in the parameters. The calibration algorithm proceeds by seeking to maximize

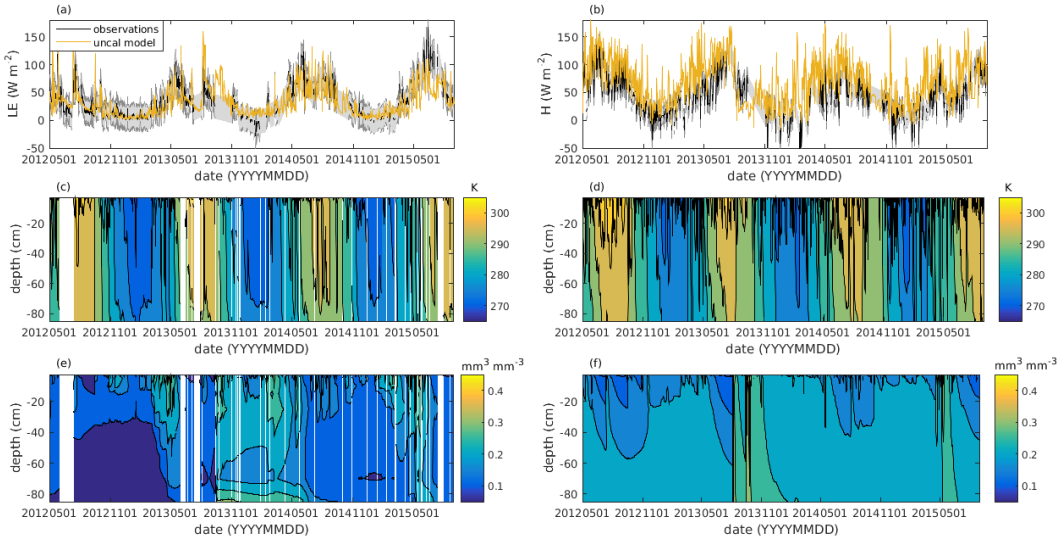

Figure 4.1: Uncalibrated model results, compared to observational data. Time series of (a) latent heat flux, (b) sensible heat flux, (c, d) soil temperature, and (e, f) soil moisture. The gray shaded region denotes ±1 observational uncertainty around the observations.

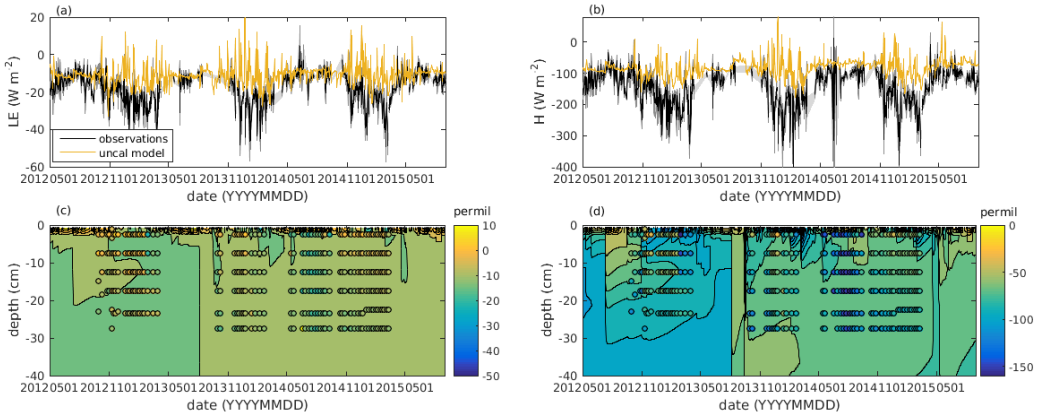

Figure 4.2: Uncalibrated model results, compared to observational data. Time series of (a) δ^{18}O of ET flux, (b) δD of ET flux, (c) δ^{18}O of soil water, and (d) δD of soil water. In (a) and (b), the gray shaded region denotes ±1 observational uncertainty around the observations. In (c) and (d), the observed isotope ratios are plotted as dots superimposed on the contours, with commensurate color scheme.

the likelihood that the model simulation results match the observational data in light of the model biases and other errors.

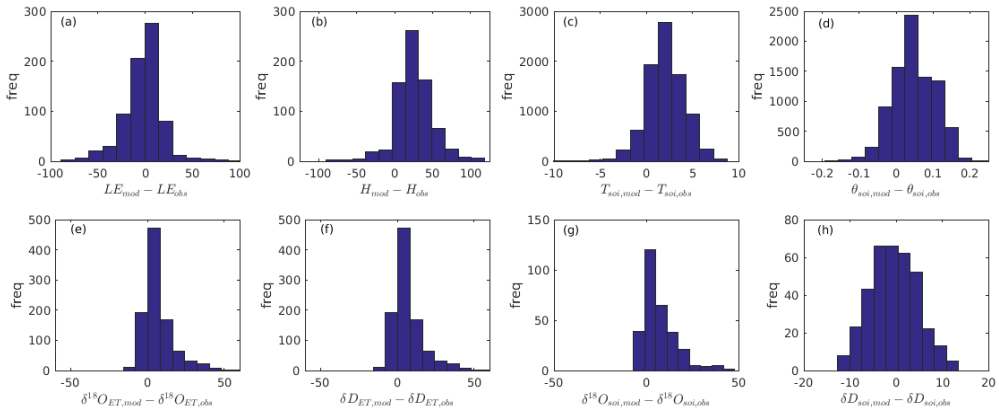

Figure 4.3: Histograms of errors in uncalibrated model results relative to observational data. (a) latent heat flux, (b) sensible heat flux, (c) soil temperature, (d) soil moisture, (e) δ^{18}O of ET flux, (f) δD of ET flux, (g) δ^{18}O of soil water, and (h) δD of soil water.

Let $\eta(t, \theta)$ refer to the vector of model output for the calibration fields (latent heat flux, sensible heat flux, soil temperature and moisture, isotope ratios of ET flux and isotope ratios of soil water) at calibration parameter values $\theta = (f_g, f_s, f_a, f_b)^T$ on day t and let $y(t)$ be the corresponding observations of these fields. In preliminary experiments, the biases in the modeled calibration fields were treated as calibration hyperparameters in the same manner as the resistance parameters [55]. It was determined that this was not necessary, so the biases were treated as structural errors, thereby reducing the size of the parameter-space the calibration approach must explore. Denote the optimal, unknown, model parameters by θ^* and let α^* be the additive model bias which optimizes the match between modeled and observed fluxes and soil temperature. The statistical model is

$$y(t) = \eta(t, \theta^*) + \epsilon(t). \tag{4.13}$$

It is simple to generalize (4.13) to include additive and multiplicative bias terms as well, and in Chapter 2 of the present work, the success and importance of the additive bias (structural error) term was demonstrated. Based on exploratory analyses, however, such flexibility is neither required nor considered in the present application.

It is convenient to think of $\zeta(t) = \eta(t, \theta^*)$ as representing the physical process the model η

seeks to capture. In (4.13), $\epsilon(t) \in \mathbb{R}^3$ accounts for model and observational errors and is modeled as a multivariate mean zero Gaussian process that is independent between components and across time points. Denote by Σ the covariance matrix of $\epsilon(t)$. It is assumed $\Sigma = \text{diag}(\sigma_1^2, \sigma_2^2, \sigma_3^2)$, where σ_k is the empirical standard deviation of the set of observations of field k, $k =$ LE, H, T_{soi}, θ_{soi}, $\delta^{18}\text{O}_{ET}$, δD_{ET}, $\delta^{18}\text{O}_{soi}$ and δD_{soi} for latent heat flux, sensible heat flux, soil temperature, soil moisture, isotope ratios of ET flux and isotope ratios of soil water, respectively. The specific form of Σ is addressed in Section 4.3.2.

The likelihood function $L(y|\theta)$ of $y = (y(1), \ldots, y(1218))^T$ (where there are 1218 days of data) is then a product of univariate normal likelihoods. Given a joint prior distribution $\pi(\theta)$ on the calibration parameters and biases, the joint posterior probability is

$$\pi(\theta|y) \propto L(y|\theta)\pi(\theta). \tag{4.14}$$

This posterior density contains all uncertainty information regarding the model parameters, and optimal values can be derived directly from the posterior (e.g., a posterior median minimizes absolute Bayes loss).

Prior distributions are required for the model parameters and bias parameters, and are assumed to be independent between parameters. Each individual component of θ is given a uniform prior with bounds $[1/100, 100]$. These hyperparameters are chosen to allow two orders of magnitude deviation above or below the control model behavior and prevent non-physical negative parameter values.

A Markov chain of draws from the joint posterior distribution of θ (Equation 4.14) is constructed using the Metropolis-Hastings algorithm [95, 53]. This approach follows the detailed outline presented by [55] for model calibration, and a brief overview of the algorithm is given here.

(1) Initial values for the Monte Carlo iteration are selected (θ_0).

(2) The Metropolis-Hastings algorithm (below) is iterated for $j = 2, \ldots, N$:

   (a) θ_{new} is drawn from a normal distribution with mean θ_{j-1} and variance s_θ^2.

(b) The posterior probability of these new iterates, $\pi(\theta_{new}|y)$, is calculated according to Equation 4.14.

(c) The acceptance probability, p, is calculated as $p = \min\left(1, \frac{\pi(\theta_j|y)}{\pi(\theta_{new}|y)}\right)$.

(d) Select the next MCMC iterate:

$$\theta_{j+1} = \begin{cases} \theta_{new}, & \text{with probability } p \\ \theta_j, & \text{with probability } 1-p \end{cases} \tag{4.15}$$

The proposal density variances are initialized at $s_\theta^2 = 1$. After 500 iterations, the adaptive Metropolis algorithm described by [49] is implemented. The covariance matrix used to propose new calibration parameters is the covariance matrix of the previous iterates, scaled by $s_d = 2.38/\sqrt{N}$ to optimally explore the parameter-space, where $N = 4$ is the dimension of the parameter-space [40].

The above Markov chain model generates samples from the posterior distribution of model parameters θ. Model parameters are initialized are $\theta_0 = 1$, representing an a priori belief that the model's default behavior is correct. Initial testing showed little deterioration in convergence performance (speed or quality) when these initial values were used, as opposed to dispersed initial conditions or those highlighted by a preliminary Latin hypercube analysis. Furthermore, convergence implies that the convergent Markov chain behavior is independent of their initial conditions. Three parallel runs of the adaptive Metropolis-Hastings algorithm outlined above are each iterated 15,000 times. The first half of each run is discarded for burn-in and the remaining values are used for analysis. No thinning is done [86].

4.3.2 Error Covariance

Following [72], four distinct error terms compose the total uncertainty: $\sigma_k^2 = \sigma_{str,k}^2 + \sigma_{par,k}^2 + \sigma_{obs,k}^2 + \sigma_{rep,k}^2$. Each of these component uncertainties is described below.

Structural uncertainty ($\sigma_{str,k}$) is the inherent disagreement between any physical model and the process it seeks to model, due to the use of approximate equations of nature. We formally define this as the difference between the model response at the true values of the calibration parameters

and the mean of the physical process being modeled [72]. For each of the calibration data fields, $\sigma_{str,k}$ is taken as the seasonal means (DJF, MAM, JJA, and SON) of the uncalibrated errors in each field (Figures 4.1 and 4.2).

Observational uncertainty ($\sigma_{obs,k}$) is error due to imperfect measurement systems. The values used are $\sigma_{obs,LE} = 22$ W m^{-2} and $\sigma_{obs,H} = 15$ W m^{-2} [126]; $\sigma_{obs,T_{soi}} = 1.5$ K and $\sigma_{obs,W_{soi}} = 0.041$ mm^{3}mm^{-3} (supplied by manufacturer); $\sigma_{obs,\delta^{18}O_{soi}} = 0.1‰$ and $\sigma_{obs,\delta D_{soi}} = 0.5‰$ [48]; $\sigma_{obs,\delta^{18}O_{ET}}$ and $\sigma_{obs,\delta^{18}O_{ET}}$ are calculated following the methods of [44], in which we incorporate both observational and representation uncertainty into the uncertainty estimate (described below). Eddy covariance methods rely on measurements of wind speed, temperature and humidity originating from a MEF tower observatory, which represents the entire tower footprint. Thus, defining the spatial scale of interest to be that represented by eddy covariance fluxes, $\sigma_{obs,H}$ and $\sigma_{obs,LE}$ incorporate representation uncertainty as well.

Representation uncertainty ($\sigma_{rep,k}$) results from heterogeneity in the site or region selected to model. Based on the estimates of sub-grid scale variability in surface temperature found from high-resolution modeling, we set the representation uncertainty for the top soil layer temperature at $\sigma_{rep,T_{soi}} = 2$ K [33]. Variability in measured soil moisture between two soil pits dug on opposite sides of the BAO site yield $\sigma_{rep,W_{soi}} = 0.0824$ mm^{3}mm^{-3}. Based on variability in long-term averages of samples of precipitation collected at a network of middle schools throughout the Colorado Front Range region (representing an area approximately the same size as the BAO footprint in CLM4), $\sigma_{rep,\delta^{18}O_{soi}} = 0.43‰$ and $\sigma_{rep,\delta D_{soi}} = 2.70‰$ [68]. $\sigma_{rep,LE}$ and $\sigma_{rep,H}$ are incorporated into $\sigma_{obs,LE}$ and $\sigma_{obs,H}$.

Similarly, it is reasonable to expect the representation uncertainty in Keeling plot-derived estimates of δ_{ET} to be incorporated into the observational uncertainty. However, this is only a valid assumption for the upper-most inlet on the tower observatory. The representation uncertainty in isotope ratios measured at or near the surface is much larger, and is estimated to be equal to $\sigma_{rep,\delta^{18}O_{soi}}$ and $\sigma_{rep,\delta D_{soi}}$. The uncertainty associated with the water vapor isotopic ratios at a given inlet height is estimated by fitting for each isotopic species i an exponentially decreasing function

of the form

$$\sigma_{vap,i}(h) = A_i + B_i \; e^{-h/h_{max}} \tag{4.16}$$

where A_i and B_i are parameters determined by forcing this function to fit the requirements $\sigma_{vap,^{18}O}(0) = 0.43‰$ and $\sigma_{vap,D}(0) = 2.70‰$, and $\sigma_{vap,i}(h_{max}) = 0$, where h_{max} is the height of the uppermost inlet. We add to this representation uncertainty the observational uncertainty (accuracy and precision) associated with each vapor isotopic measurement. The later is estimated from [132] (c.f., their Table 6), who made repeated measurements of known standard samples on two different Picarro L2120-i machines: accuracies are 0.075‰ and 0.550‰ for δ^{18}O and HDO, respectively, and precisions are 0.04‰ and 0.40‰ for δ^{18}O and HDO, respectively. The total uncertainty at any given inlet, which is factored into the calculations from [44] to determine the observational and representation uncertainty associated with $\delta^{18}O_{ET}$ and δD_{ET}, is then $\sqrt{\sigma_{vap,i}(h)^2 + \sigma^2_{accuracy,i} + \sigma^2_{precision,i}}$.

Parametric uncertainty ($\sigma_{par,k}$) results from uncertainty in model parameters. While the purpose of this assimilation calculation is to reduce parametric uncertainty (that associated with the ecosystem resistance terms), iCLM4 has many other parameters which attempt to best represent the physical attributes and ecosystem behavior of the observation site. Among these parameters are surface albedo, leaf area index (LAI), soil texture (percentage of soil which is sand, silt or clay), percentages of the vegetation which is bare soil, trees, grass or shrubs, the strength of the isotopic kinetic fractionation factors, and the B exponent from [22] which is a sensitive quantity in the parameterization of hydraulic conductivity [103, 57]. Following [25], a sensitivity analysis is performed to inform an estimate of parametric error. First, a series of 15 model simulations are produced: (1) a control run; (2-3) ±20% sand fraction, in estimating soil hydraulic conductivity; (4-5) ±20% LAI; (6-7) ±20% albedo; (8-11) +20% bare soil, trees, grass, shrubs, individually; (12-13) ±20% Clapp and Hornberger B; (14) no isotopic kinetic separation; and (15) +20% in the strength of all isotopic kinetic fractionation factors. For each simulation, the RMS deviations between the control modeled and the experiment modeled calibration data fields are calculated. For each of these fields, the parametric uncertainty of the quantity in question is estimated as the Euclidean distance

of the 14-dimensional RMS deviation point from the sensitivity tests to the origin. These result in parametric uncertainty estimates of $\sigma_{par,LE} = 5.60$ W m^{-2}, $\sigma_{par,H} = 7.74$ W m^{-2}, $\sigma_{par,T_{soi}} = 0.56$ K, $\sigma_{par,W_{soi}} = 0.039$ mm^{3}mm^{-3}, $\sigma_{par,\delta^{18}O_{ET}} = 3.54$‰, $\sigma_{par,\delta D_{ET}} = 8.01$‰, $\sigma_{par,\delta^{18}O_{soi}} = 1.52$‰, and $\sigma_{par,\delta D_{soi}} = 4.34$‰. These estimates are the maximum deviation considering fairly large (20%) perturbations on each parameter. Thus, the true uncertainty due to these parameters is likely lower than these estimates. Conversely, uncertainty due to feedbacks when multiple parameters are perturbed simulataneously and uncertainty due to parameters not considered here conspire to increase the parametric uncertainty beyond this estimate. While iCLM4 has other parameters and parameterizations which would need to be accounted for to fully quantify parametric uncertainty, these experiments provide a sufficient estimate of $\sigma_{par,k}$. Furthermore, the contribution of $\sigma_{obs,k}$ to σ_k is much larger than any reasonable estimate of $\sigma_{par,k}$.

The experiments presented here incorporate the full uncertainty accounting outlined above, thus the entries of the error covariance matrix Σ are given by $\sigma^2_{obs,k} + \sigma^2_{rep,k} + \sigma^2_{str,k} + \sigma^2_{par,k}$.

4.4 Results

4.4.1 Posterior inference

The calibration yields well-constrained posterior estimates of the model parameters, as well as site growing season-average transpiration fraction, f_T, for the four years of data assimilated (Figures 4.4 and 4.5). The 95% credible intervals and posterior medians of the constrained distributions are given in Table 4.1. The uncalibrated modeled average transpiration fraction is given by the vertical red line in Figure 4.5. All three experiments find that the modeled site-average f_T is too low (61%) when uninformed by observational data. That the a priori (uncalibrated) estimate of f_T does not fall within the 95% credible interval in any of the experiments presented here highlights the need for statistical calibration, regardless of whether stable water isotopic information is considered. When only HDO data is assimilated (E2), there is agreement between the posterior parameter and f_T estimates and the posterior estimates from the isotope-independent experiment (E1), but

the posterior widths are slightly narrower (Table 4.1). This is consistent with our hypothesis that assimilation of data from one isotopic species is feasible, and provides additional constraint.

The distribution of posterior f_T estimates using data from two isotopic species (E3) is wider than from a single isotopic species (E2), and the model parameters suggested by integrating two isotopic data sets are somewhat different from integrating only one species (Figures 4.4 and 4.5). In particular, the leaf boundary layer resistance must be much larger ($\sim 13.5\times$) the control modeled value, in order to match two isotopic data sets. This indicates that two isotopic data sets were necessary to better inform the estimate of isotopic kinetic effect. Namely, that the leaf boundary layer resistance must be stronger suggests a stronger isotopic kinetic effect through the leaf boundary layer is required to match both isotopic species' data sets.

The bimodel nature of the E3 posterior estimates of f_a, the canopy-to-GCM air space aerodynamic resistance parameter, best illustrates the difficulty in assimilating data concerning two isotopic species (Figure 4.4j), although the surface-to-canopy air space aerodynamic resistance also displays this bimodal behavior (Figure 4.4). The primary mode at $f_a \approx 0.5$ is consistent with the E1 and E2 posterior modes for f_a. This indicates that $f_a \approx 0.5$ is consistent with the isotope-independent data and the HDO data used for calibration. When $H_2^{18}O$ is incorporated, a second mode emerges at $f_a \approx 0.6$. The precise treatment of the isotopic kinetic effects within iCLM4 is likely the source for this bimodal behavior. These experiments highlight the difficulty in leveraging observations of multiple isotopic species in a practical setting. Despite this difficulty, it is the distribution of transpiration fraction which is of interest, and these distributions are unimodal (Figure 4.5), suggesting that the bimodality of the resistance parameters when two isotopic species are used in the calibration data is not necessarily a practical concern.

In experiment E3, the parameters for stomatal resistance and leaf boundary layer resistance were strongly negatively correlated ($r = -0.92$, $p < 10^{-5}$, Figure 4.6h). This negative correlation is expected from the physical interpretation of these parameters. If total transpiration is fixed, then the net ecosystem conductance through vegetation must also be fixed. This net conductance is the sum of the stomatal and leaf boundary layer components, so if the stomatal conductance were

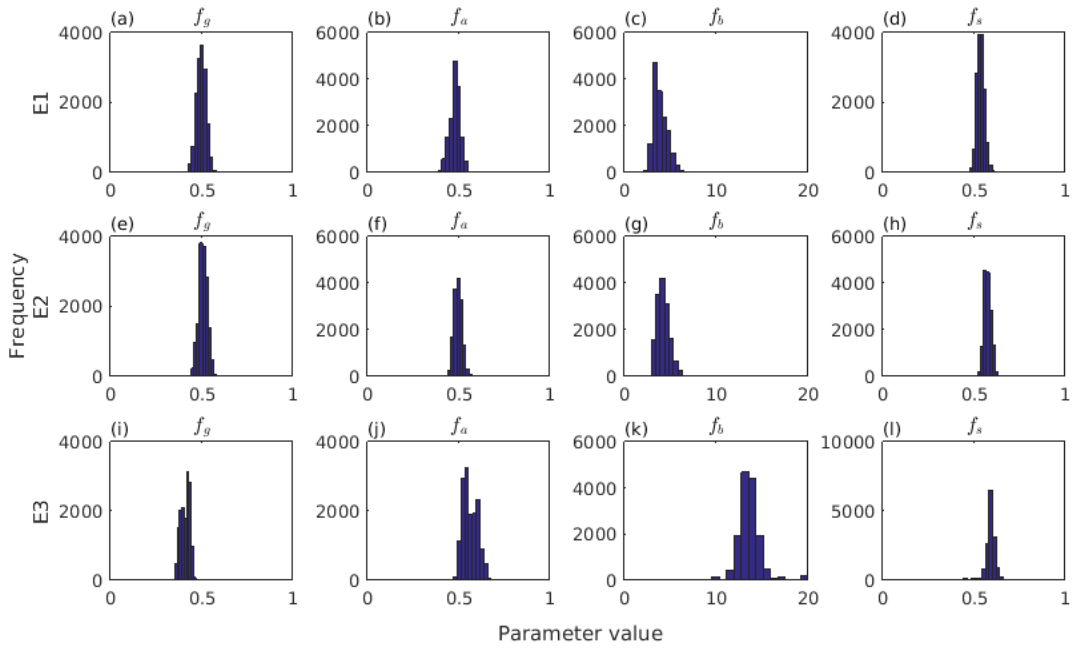

Figure 4.4: Posterior histograms of the calibrated model parameters. Top row (a-d): results for E1; middle row (e-h): results for E2; bottom row (i-l): results for E3.

Table 4.1: 95% Credible Intervals

	E1			E2			E3		
	P2.5	**Median**	**P97.5**	**P2.5**	**Median**	**P97.5**	**P2.5**	**Median**	**P97.5**
f_g	0.45	0.50	0.55	0.46	0.51	0.56	0.36	0.42	0.45
f_a	0.43	0.48	0.53	0.46	0.50	0.54	0.50	0.55	0.65
f_b	2.83	3.74	5.64	3.21	4.17	5.74	11.26	13.55	20.06
f_s	0.50	0.54	0.58	0.54	0.57	0.61	0.49	0.59	0.63
f_T	69.1	69.7	70.3%	68.7	69.2	69.8%	65.4	66.3	67.0%

to decrease, for example, then the leaf boundary layer conductance must show a corresponding increase. The transpiration flux is indeed well known because total ET is constrained through the assimilation of observations of latent heat flux, and the transpiration fraction is well constrained (Figure 4.5). No other significant correlations among the parameters and f_T, for any of the three experiments, were present. It is important to note that this correlation only emerged when both HDO and $H_2^{18}O$ data were assimilated in the calibration, which suggests the intuitive physical relationship between f_s and f_b can only be resolved by two water isotopic data sets. That the leaf

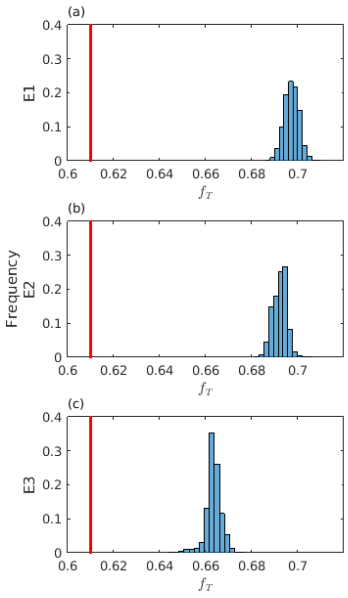

Figure 4.5: Posterior histograms of the calibrated modeled growing season average transpiration fraction, f_T, results for (a) E1; (b) E2; and (c) E3. The red vertical line indicates the a priori (uncalibrated) f_T.

boundary layer resistance in experiment E3 is altered by a factor of 3× the calibration parameter values from E1 and E2, and yet the modeled posterior median f_T changes by less than 1% demonstrates the relatively weak influence of the leaf boundary layer resistance on ET partitioning, compared to the stomatal resistance and aerodynamic resistances. The reader is cautioned that these results are derived from a semiarid grassland site, with a canopy height of roughly 0.5 m and dominantly scrubgrass vegetation, and should not be taken as representative of the global land surface.

4.4.2 Isotope-based ET partitioning using synthetic observations

A posterior ensemble of model realizations was generated by drawing 100 random samples from the posterior estimates of the resistance parameters. 100 posterior samples were drawn for each of E1, E2 and E3 yielding 300 simulations total (Figure 4.4). Using the methods of Section 4.2.3.1 and output from these model ensembles as synthetic observations, modeled isotope-based estimates

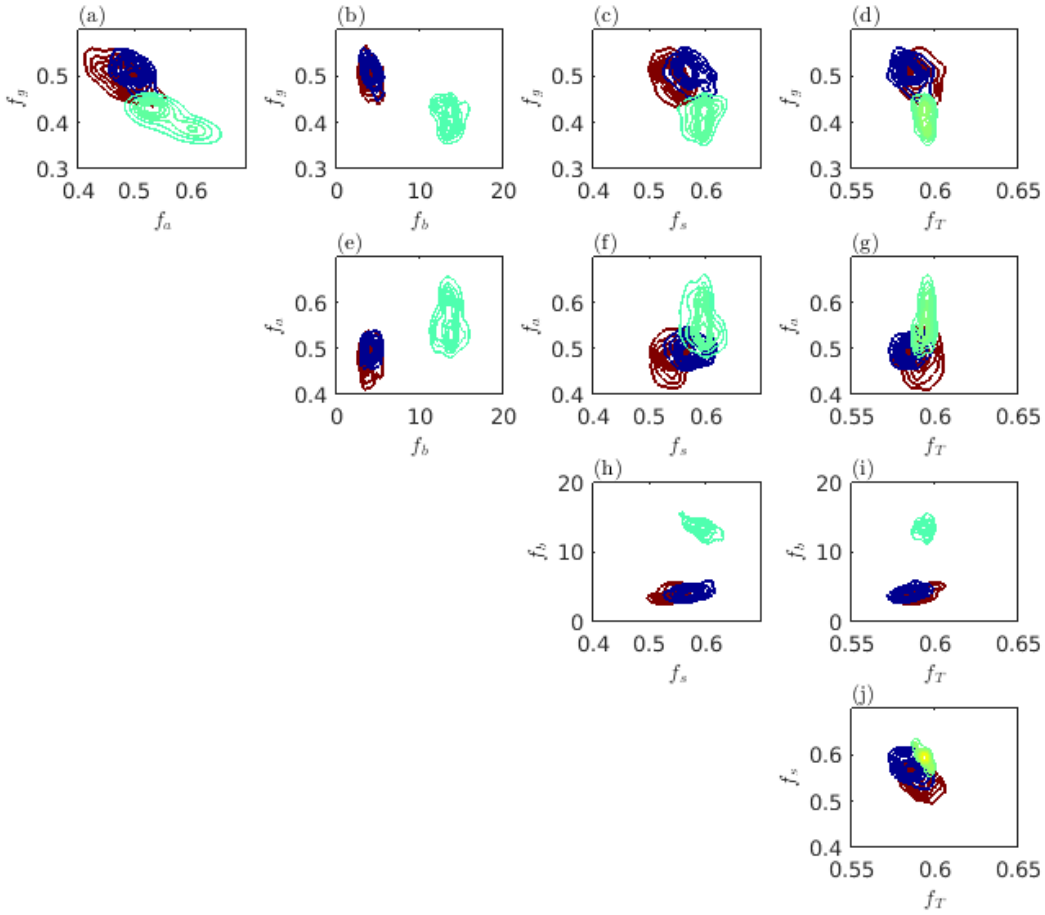

Figure 4.6: Pairwise posterior estimates between calibration parameters and transpiration fraction. These two-dimensional Gaussian kernel density estimates were generated using the results from the E1 (red contours), E2 (teal contours) and E3 (blue contours) simulations.

of ET partitioning, $f_{T,D}$ and $f_{T,^{18}O}$ were calculated and compared to directly modeled (isotope-independent) partitioning, f_T.

The time series of isotopically-derived partitioning displays a high bias relative to the true, directly modeled partitioning (Figure 4.7). In Figure 4.7, the blue, red and black time series' are composed of each of the 100 ensemble members' transpiration fractions, derived from δ^{18}O, δD and directly modeled fluxes, respectively, giving rise to a range of credible partitioning realizations. The gray shaded regions indicate growing seasons (May–October). The superimposed scatter points for

$f_{T,^{18}O}$ and $f_{T,D}$ were calculated directly from observational data from the BAO site [69]. Generally, the two isotope-based partitioning estimates agree well, although when disagreement exists $f_{T,D}$ is biased high relative to $f_{T,^{18}O}$ (Figure 4.7c). This trend is reflected in the isotopic observations-based partitioning at some points during the 2012 and 2014 growing seasons, but the observations more generally reflect the opposite bias as is seen in the modeled isotope ratio-based partitioning. During the growing seasons, the modeled isotope-based estimates for $f_{T,^{18}O}$ and $f_{T,D}$ were frequently found to be outside of the 0–1 range, which is seen in Figure 4.7 as gaps in the time series lines. This affects $f_{T,^{18}O}$ more than $f_{T,D}$, suggesting poor knowledge of the net isotopic kinetic effect is to blame, because as a heavier isotope, $H_2^{18}O$ is more affected by kinetic fractionation than HDO. When the modeled $f_{T,^{18}O}$ and $f_{T,D}$ were inside the 0–1 range, the observation-based estimates of $f_{T,^{18}O}$ were frequently biased high and the observation-based estimates of $f_{T,D}$ were often biased low relative to the modeled values. In the 2013 growing season, however, the observations-based estimates of $f_{T,^{18}O}$ were in rough agreement with the modeled values for $f_{T,D}$ (the modeled $f_{T,^{18}O}$ was outside of the $0-1$ range for most of the 2013 growing season). While the two modeled isotope-based partitioning estimates often are in agreement with each other and with the observation-based isotopic partitioning estimates, they generally agree poorly with directly modeled partitioning.

The isotope-based partitioning has a high bias, which is most notable during winter, and suppressed during growing seasons. For the entire period for which BAO observational data are available, the mean bias in $f_{T,^{18}O}$ and $f_{T,D}$ is 0.22–0.24 (in units of f_T, 0–1, Table 4.2). When only growing season data are considered, and the confounding effects of the 2013 flooding event are removed, this mean ensemble bias is reduced to 0.07–0.12 for $f_{T,^{18}O}$ and 0.04–0.07 for $f_{T,D}$. That the 2013 high bias begins coincident with the flooding event (September 2013) demonstrates that there are physical processes which were modeled as a result of the flood which are not accounted for in this isotope-based partitioning method. It is also striking that the biases in isotope-based partitioning increase as isotopic data are assimilated in the calibrated (E2 versus E1, and E3 versus E2, Table 4.2). This suggests that while the calibration improved the model representation of the surface fluxes and state variables, the isotope-based partitioning method relies on physical processes

which were either not considered or not improved.

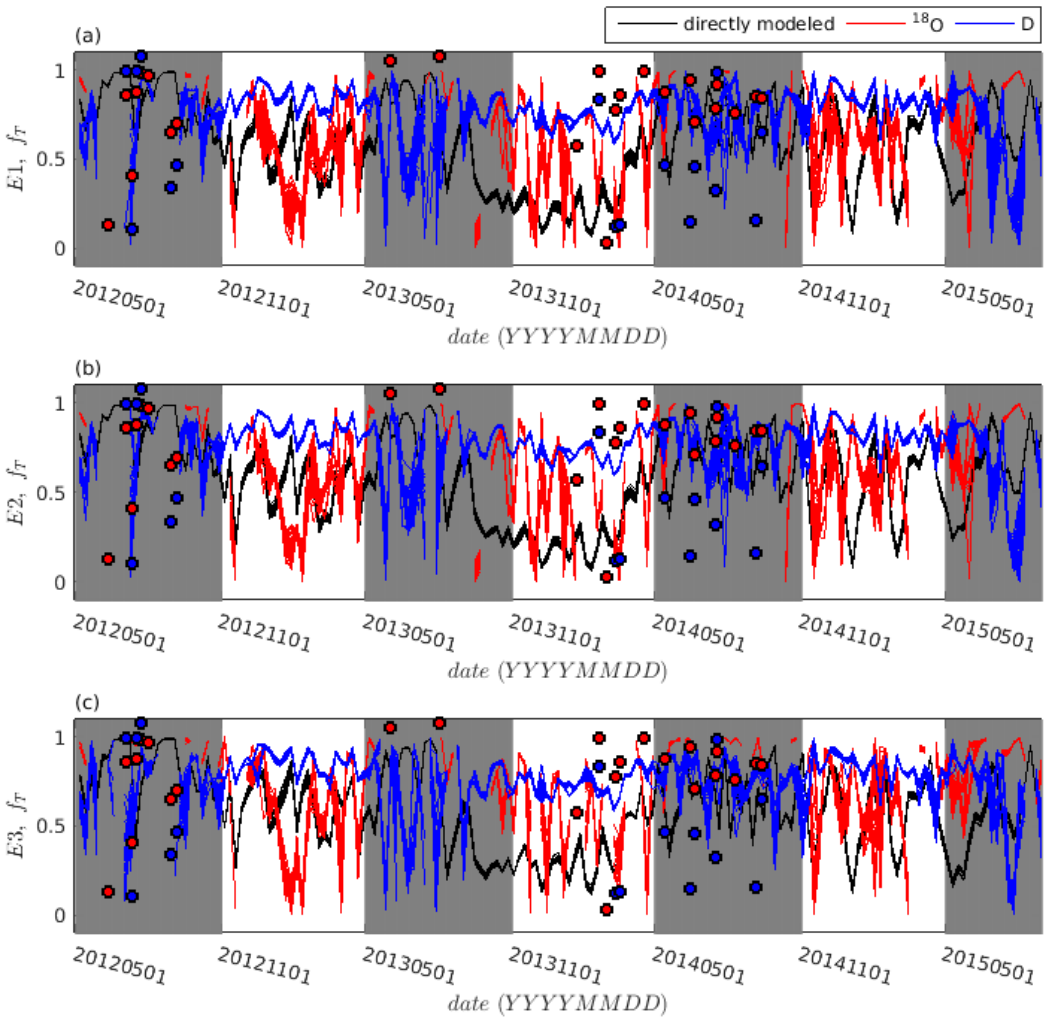

Figure 4.7: Time series of model-based partitioning: true, directly modeled (f_T, black); from δ^{18}O ($f_{T,^{18}O}$, red); from δD ($f_{T,D}$, blue). The gray shaded regions indicate growing seasons (May–October). Gaps in the isotope-based partitioning correspond to periods when the calculation (Section 4.2.3.1) yielded values for $f_{T,i}$ outside of the 0–1 range.

4.4.3 Information content

The Kullback-Leibler (KL) divergence of the posterior distribution of model parameters and f_T from E2 from that of E1 was $D_{KL}\left(\Pi_{E_2} \| \Pi_{E_1}\right) = 3.04$ nats, and the KL divergence of E3 from

Table 4.2: Isotope-based partitioning biases

	^{18}O			D		
	all	growing season	growing season (no 2013)	all	growing season	growing season (no 2013)
E1	0.229	0.113	0.073	0.229	0.084	0.046
E2	0.234	0.116	0.074	0.234	0.086	0.047
E3	0.236	0.173	0.113	0.223	0.103	0.065

E2 was $D_{KL}\left(\Pi_{E_3} \| \Pi_{E_2}\right) = 1.79$ nats (c.f., Equation 4.11). Thus, the marginal gain in information concent by incorporating a second isotopic species into the calibration data set (E3) is less (by a factor of 0.59) than the information gained by incorporating data from a single isotopic species (E2). This reduction in the efficacy of isotopic information suggests that when a second isotopic species is assimilated (E3), the difficulty in properly modeling the isotopic kinetic effect leads to difficulty in simulataneously simulating both isotope ratios accurately.

Error histograms were produced for the three ensembles of calibrated simulations, analogous to the control (uncalibrated) simulation, and all four sets of error histograms were normalized to sum to one across all bins, yielding probability distributions (Figures 4.8 and 4.9). The KL divergences between the control and ensembles, and among the ensembles, was calculated as the sum of the individual relative entropies between all eight calibration data field error distributions (c.f., Equation 4.12). $D_{KL}\left(\mathcal{E}_{E_1} \| \mathcal{E}_{control}\right) = 1.26$ nats, indicating a baseline gain in information content through incorporating the non-isotopic data fields into the calibration data set. If a surface flux-state variable pair is considered as one constraint, then 1.26 nats is the value of two constraints ((a) latent heat flux and soil moisture, and (b) sensible heat flux and soil temperature). When the surface flux-state variable pair δD_{ET} and δD_{soi} is incorporated into the calibration data (E2), the KL divergence from the non-isotopic data set (E1) is $D_{KL}\left(\mathcal{E}_{E_2} \| \mathcal{E}_{E_1}\right) = 0.177$ nats. According to the baseline calcuation ($D_{KL}\left(\mathcal{E}_{E_1} \| \mathcal{E}_{control}\right) = 1.26$ nats), one constraint should contain approximately 0.63 nats of information, so the HDO data added significantly less than a full constraint of information. When both HDO and $H_2^{18}O$ isotope ratios of ET flux and soil water are added to the calibration, however, the information added relative to the non-isotopic data set is

$D_{KL}\left(\mathcal{E}_{E_3} \| \mathcal{E}_{E_1}\right) = 0.626$ nats. Thus, calibration data from one isotopic species provides minimal additional information, as was noted from little change in the distributions of errors in the calibration data fields and posterior model parameter estimates, whereas including two isotopic species provides considerably more information, adding up to one full constraint.

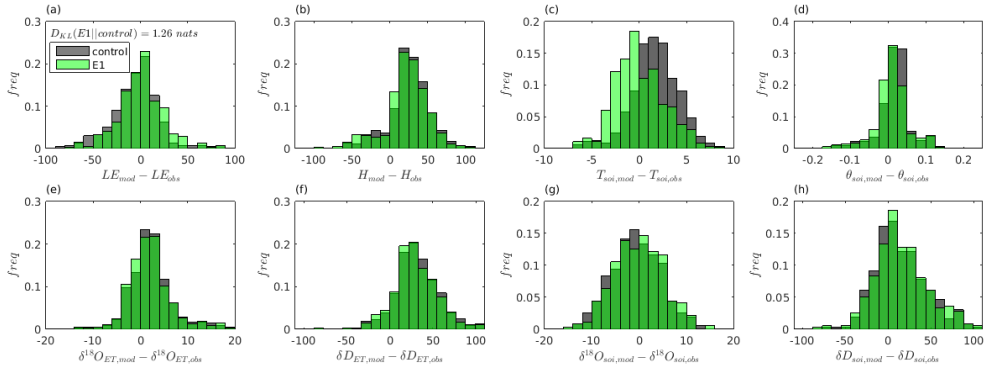

Figure 4.8: Distributions of errors in calibration data fields between the control simulation (black shading) and the E1 calibrated ensemble (green shading).

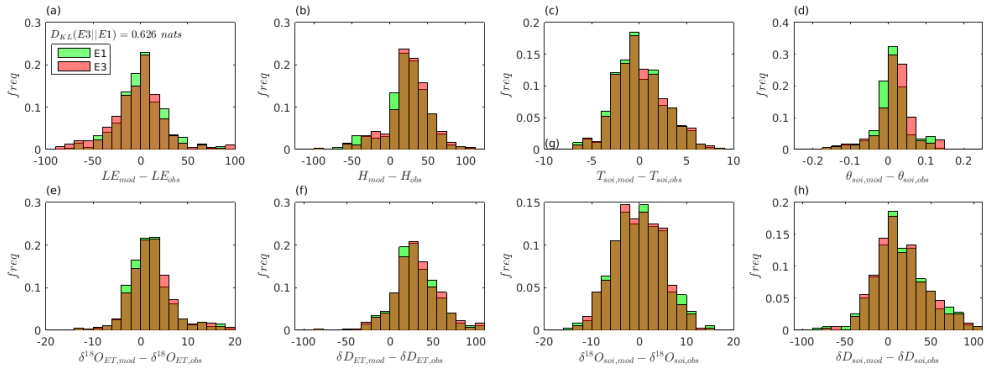

Figure 4.9: Distributions of errors in calibration data fields between the E1 calibrated ensemble (green shading) and the E3 calibrated ensemble (red shading). Brown shading indicates overlap between the two distributions.

4.5 Summary and conclusions

We have developed and implemented a Bayesian approach for the calibration of land surface model parameters. The calibration scheme has been applied to an isotopically-enabled land surface

model (iCLM4), using data sets for calibration consisting of no isotopic information (E1), isotopic information concerning one isotopic species (E2) and two isotopic species (E3). This calculation was undertaken with the goal of quantifying (1) the benefits of adding observations of one isotopic species to the calibration data set, and (2) the benefits of adding a second isotopic species to the data set. The approach focused on the goal of improving the model representation of the isotopic kinetic fractionation effect, and ultimately improving isotope-based estimates of the transpiration fraction, and therefore emphasized calibration of aerodynamic and vegetation resistances for heat and moisture which control the exchange between soils, leaves and the overlying atmosphere. These goals were made possible only by integrating a statistical calibration scheme (Section 4.3.1) with an isotopically-enabled land surface model (Section 4.2.2). This is because in this model experimental setting, a directly modeled transpiration fraction, f_T, serves as the true ET partitioning, and directly modeled isotope ratios and environmental conditions (e.g., vegetation temperature) serve as synthetic observations. All direct model output is internaly consistent within the iCLM4 model framework, therefore any discrepancies between the isotope-based partitioning ($f_{T,i}$) and the isotope-independent, direct model partitioning (f_T) are due to simplifications made in the offline isotope-based partitioning method, commonly used in field campaigns (Section 4.2.3.1). We have demonstrated the ability of this calibration approach to constrain the posterior distributions of aerodynamic and vegetation resistance parameters in iCLM4, and shown that the incorporation of water isotopic data into the calibration data set yields significant improvement in the modeled isotope-based partitioning, particularly in summer months.

The experiments presented here found that implementing the calibration procedure actually increased the magnitude of the bias in isotope-based partitioning by incorporating observational data from a single isotopic species (E1 versus E2 and E3, Table 4.2). By separating the errors in $f_{T,i}$ into a growing season component (May through October), it was found that growing season biases in isotope-based partitioning ($< 12\%$) are much lower than winter biases ($> 20\%$). That iCLM4 has difficulty partitioning fluxes and modeling winter freezing and snow pack is consistent with results from both [82] and Section 2.4.2 of the present work, modeling snow cover fraction in

native CLM4, as well as previous work partitioning fluxes over snow pack [101]. Possible avenues to fix this issue include incorporation of snow depth or cover fraction data into the calibration data set, or explicit assimilation (as in Section 3.3). The match seen in Figure 4.7 and biases in Table 4.2 indicate that isotope-based ET partitioning estimates from May through mid-October may yield partitioning estimates consistent with isotope-independent approaches for a growing season average value, but will not provide robust estimates of partitioning on shorter time scales. When the model was informed by all calibration data, including water isotopic data, the partitioning based directly on water isotopic observations was in agreement with the modeled isotope-based partitioning, but both were biased higher than the directly modeled partitioning (Figure 4.7c). This high bias in the isotope-based estimates is consistent with a recent meta-analysis by [115], who found that isotopic approaches for ET partitioning generally displayed a high bias relative to ET partitioning estimates based on both isotope-independent models and observations.

This directly modeled partitioning the the best estimate for f_T at the BAO site, so these biases in the modeled and observed isotope-based partitioning both strongly suggest a bias is present in the water isotope ratio-based method for ET partitioning (Section 4.2.3.1). The isotope-independent model-based estimate of f_T ($65.4 - 67.0\%$, Table 4.1) is close to the estimate of $f_{T,^{18}O} = 68 - 78\%$ obtained by [35], who used an observational isotopic approach analogous to the one of Section 4.2.3.1 to partition ET for a shortgrass steppe region of northeastern Colorado, USA. That these authors' isotope-based estimate is in good agreement with our modeled isotope-based estimates for similar ecosystem sites is of no surprise (accounting for the $7 - 11\%$ high bias in $f_{T,^{18}O}$ (Table 4.2). This bias may be overcome by one or more of the following: (1) include evaporation of canopy-intercepted water as a third ET stream in addition to surface evaporation and vegetation transpiration in the isotopic partitioning model of Equation 4.5 [140]; (2) choose a net ecosystem kinetic fractionation factor to bring estimates of $f_{T,^{18}O}$ and $f_{T,D}$ into agreement (possibly through use of the statistical calibration techniques implemented here); or (3) explicitly calibrate to minimize the mismatch between $f_{T,^{18}O}$ and $f_{T,D}$, or between each of $f_{T,^{18}O}$ and $f_{T,D}$, and f_T.

The posterior distributions of the aerodynamic and vegetation resistance calibration parameters were not centered at one, implying model tuning should be performed for iCLM4 to best match observations of surface fluxes, soil temperature and moisture, and isotope ratios of ET flux and soil water. When a single isotopic species was introduced to the calibration data set, the posterior distributions of model parameters became better constrained (95% credible intervals were narrower, Figure 4.4, E2 versus E1). When a second isotopic species was introduced, however, some of the distributions became bimodal, and others more poorly constrained (Figure 4.4i, j, k and Figure 4.5c). Furthermore, the estimates of ET partitioning based on isotope ratios δ^{18}O displayed worse biases when δ^{18}O was included in the calibration data set than when only δD was used for calibration (Table 4.2, E3 versus E2). These discrepancies are attributable to one or more of: (1) the model representation of the isotopic kinetic effect is confounding the efficacy of including a second isotopic species in the calibration data set; (2) observations of δ^{18}O and δD simultaneously are too uncertain to yield significant benefits in the calibration procedure (it may be possible to match observations of one, but not both); or (3) the formulation of the net ecosystem kinetic effect used in the offline partitioning approach is in error. The kinetic effect from (3) is parameterized in a resistance-weighting scheme from [84], and is analogous to the manner in which iCLM4 implements each individual kinetic fractionation factor (Section 3.2.2). An a posteriori sensitivity test was conducted, in which the strength of this ecosystem-scale kinetic effect was varied across a range of reasonable values ($\pm$20%). This yielded only minor improvements. Thus, the cause of these issues is unlikely to be the canopy-scale isotopic kinetic fractionation factor (3).

The information content of the two isotopic sets of data was shown to be about half of the information content of the two non-isotopic data sets: $D_{KL}\left(\mathcal{E}_{E_3} \| \mathcal{E}_{E_1}\right) = 0.626$ nats, versus $D_{KL}\left(\mathcal{E}_{E_1} \| \mathcal{E}_{control}\right) = 1.26$ nats. This was found by analyzing the distributions of errors in the calibration data fields. The additional constraint on the posterior distributions of model parameters and growing season average transpiration fraction when data from one species (HDO) was found to be $D_{KL}\left(\Pi_{E_2} \| \Pi_{E_1}\right) = 3.04$ nats. When a second species was introduced, the marginal gain in information content was $D_{KL}\left(\Pi_{E_3} \| \Pi_{E_2}\right) = 1.79$ nats. Thus, there is a decrease in the marginal

benefits to additional isotopic information. Despite this decrease, we have established that the two isotopic data sets, when assimilated simulataneously with the two contraints of the non-isotopic data sets, provide a full additional constraint.

Perhaps the most striking result was that in the control model set-up, only one day (out of 1218) of model output yielded an isotope-based estimate of transpiration fraction which was in the physically meaningful 0–1 range. This highlights that calibration of a physical model is a need, not a luxury. No model is perfect, and iCLM4 is no exception. Even the non-isotopic statistical calibration experiment conducted here (E1) was sufficient to yield a more realistic distribution of isotope-based partitioning realizations (Figure 4.7 and Table 4.2). These results suggest that without any effort put into ensuring a physical model is an accurate representation of the system or site it is meant to simulate, the output from this model is highly questionable, and perhaps even outright unphysical, as seen in the present case. With the calibrated model ensembles, however, a needed evaluation of the fidelity with which stable water isotope ratios may be used to partition total ET into evaporation and transpiration components was possible. When flux and state variable observational data, including water isotopic data, were assimilated in the calibration framework described here, this evaluation concluded that the isotope-based partitioning displays poor agreement during winter months and a high bias of $4 - 12\%$ during the growing season.

Chapter 5

Summary and Conclusions

This work was conducted with several goals:

Goal 1: to develop a model experimental framework to establish the fidelity with which stable water isotope ratios may be leveraged to obtain evapotranspiration (ET) partitioning estimates;

Goal 2: to incorporate into this modeling framework a statistical calibration scheme, in which observational data is synthesized with model output to within the uncertainty in each, thereby improving model performance; and

Goal 3: to quantify the benefits of stable water isotopic information within this statistical calibration scheme, which accounts for numerous sources of uncertainty in model and data.

5.1 Goal 1: A stable water isotopic model experimental framework

Goal 1 was accomplished in Chapter 3, in which a stable water isotopic modeling framework, iCLM4, was developed, implemented, and validated against measurements of isotope ratios in vapor, vegetation and soil water. The sensitivity of the coupled iCESM model (iCLM4+iCAM5+iRTM) to various parameterizations for the fractionating effects of evapotranspiration has been analyzed.

In Chapter 3, among experiments EC, ES and ELI, it is found that the net isotopic kinetic fractionating effect of evapotranspiration can be tuned to improve agreement between the modeled and observed isotope ratios of river outflow, precipitation and vegetation water, but a more detailed and general treatment of the controls on the isotopic kinetic fractionation factor is needed. The

network of aerodynamic resistances controls this isotopic separation, as well as general circulation of moisture and heat throughout the ecosystem, and thus is a natural choice for the parameters of interest in the calibration experiment conducted in Chapter 2 [84]. The E00 experiment provided the key result that failure to account for the water isotopic physics in the land surface component of a global climate model (iCESM) leads to poor agreement with all observational data considered here on a global scale (isotope ratios in precipitation, river outflow and vegetation) [60, 62, 61].

The site-level experiments from the Manitou Experimental Forest (MEF) and Boulder Atmospheric Observatory (BAO) provided the essential result that CLM4 does not inject infiltrated soil water deeply enough into the soil column, suggesting too weak of hydrological connectivity [43]. The soil moisture data assimilation experiment, conducted using the high quality and high temporal resolution data from the BAO site, showed that the modeled soil water isotope ratios are improved when the bulk soil water representation is improved. The improvement in modeled soil water isotope ratios resulted from completely isotope-independent data being assimilated. Thus, errors in the native (non-isotopic) CLM4 soil hydrology lead to errors in the soil water isotope ratios. These, in turn, lead to errors in ET flux and its isotope ratios, which when coupled to isotope-enabled GCM will leak errors into other parts of the global water cycle. Indeed, soil hydrological errors are likely at least partially responsible for the persistant biases in the coupled iCESM model with respect to global databases of isotope ratios in precipitation (GNIP, [60]) and river outflow (GNIR, [62]).

5.2 Goal 2: Statistical model calibration

Chapter 2 outlined and implemented a Bayesian approach for the calibration of land surface model parameters. This calculation demonstrated that the challenges posed by having only data with large total errors and models with large intrinsic biases may be overcome by adequately accounting for all error sources and biases, within the calibration framework. The approach focused on the goal of improving estimates of the transpiration fraction and therefore emphasized calibration of aerodynamic and vegetation resistances for heat and moisture which control the exchange between

soils, leaves and the overlying atmosphere. We have demonstrated the ability of this calibration approach to constrain the posterior distributions of these ecosystem resistance parameters in CLM4. The advantages of this method include (1) quantification of uncertainty in model structure, model parameters and model output (Tables 2.1 and 2.2) and (2) calibrating model parameters such that model output agrees with observational data to within the errors inherent in both the model and observations. In this way, Goal 2 was completed. Furthermore, the posterior distributions for the multiplicative calibration parameters were not all centered at zero; many of the 95% credible intervals for these parameters do not even contain zero. Thus, this experiment demonstrated that while "out-of-the-box" model output may be reasonable, it may also not be credible, highlighting the need for model calibration.

The poor performance of experiment E1 (not accounting for model biases/structural uncertainty) provided the essential result that failing to account for all sources of model and observational uncertainty (in particular, failing to satisfy the assumption of normally distributed errors with mean zero) is detrimental to assimilation techniques [55]. In the application of Chapter 2, it is clear that accounting for structural uncertainty resulted in the most dramatic improvement in the match between model output and observations; model biases must not be neglected.

The experiments presented in Chapter 2 found that implementing the calibration procedure reduced RMSE for all three sets of observational data. While the calibration improved model performance for latent and sensible heat fluxes and top soil layer temperature, model performance for soil moisture deteriorated only for the early season snow melt (DOY 125-155). E2 and E3 improved the match between modeled top soil layer temperature and observations, which required raising the temperature by several degrees. This, in turn, likely caused the precipitation which would have formed this snow pack to fall as rain instead of snow. Additionally, this difficulty in simulating the snow pack at MEF is consistent with the results of CLM4 experiments conducted by [82] (cf. Figures 2 and 6), whose global experiments found that CLM4 underestimated snow cover fraction relative to observations in central USA. Consistent with the results of the BAO soil moisture assimilation experiment from Chapter 3, calibration of the early season snow pack

sublimation and melting, or assimilation of soil moisture data are potential avenues to fix this issue. The need for additional data was further highlighted by the slightly bimodal posterior distribution of the stomatal resistance parameter, f_s. Incorporating soil moisture or water isotopic data into the calibration data set both offer promise for distinguishing between the primary and secondary modes of f_s, and further constraining this parameter.

5.3 Goal 3: On the benefits of stable water isotopic information

Chapter 4 took a lesson from Chapters 2 and 3, and incorporated soil moisture and soil water isotopic data into the calibration data set for the case of a 4-year (ongoing) field campaign at a site in central Colorado, USA. The statistical approach of Chapter 2 was used to combine field observations and the isotopically-enabled land surface model of Chapter 3 to calibrate uncertain model parameters pertaining to the relative pathways by which moisture and heat are exchanged between land and atmosphere. These same parameters control the net ecosystem isotopic kinetic fractionation factor. Experiments were performed to quantify the benefits of calibrating using no isotopic information, as well as adding one or two datasets of stable water isotopic information to the calibration, achieving Goal 3.

Stable water isotopes offer a method to partitioning total ET into evaporation and transpiration components, but lacks a standard approach against which individual partitioning efforts may be compared. Using iCLM4, however, model output for environmental conditions and water isotope ratios can be used as synthetic observations to derive a commonly used isotope-based partitioning estimate (Section 4.2.3.1. These synthetic observations are consistent with all model output, including the directly modeled transpiration fraction, f_T. Therefore, this model experimental framework (which resulted from Goal 1) was used to test the fidelity with which isotope-based estimates of ET partitioning reproduce direct model partitioning, which in the modeling framework is known to be the "truth." Furthermore, implementing this model experiment in the context of the calibration scheme (from Goal 2) permits a range of plausible partitioning realizations, both directly modeled and resulting from leveraging stable water isotope ratios. It was found that the

isotope-based transpiration fraction displayed little ($< 12\%$) bias during the growing season (May through October), but large biases during winter months ($> 20\%$). This match was only found on a growing season average time scale, and the time series match between directly modeled and modeled isotope ratio-based partitioning displayed little or no predictive power in the isotope-based partitioning (Figure 4.7). The errors and biases in winter isotope-based ET partitioning estimates highlights the need for improvements in snow and soil water representation in models, as well as a need for high quality soil moisture observational data.

When the Kullback-Leibler (KL) divergence was used to quantify the additional benefits yielded by incorporating additional data, including water isotopic data, into the calibration data set in constraining posterior distributions of model parameters and transpiration fraction. These metrics showed that these marginal benefits (1.79 nats) were reduced relative to when the first isotopic species was introduced to the data set (3.04 nats). By assessing the distributions of errors in the calibration data fields for the three calibration experiments, the information content of the two isotopic sets of data was shown to be about half of the information content of the two non-isotopic data sets: $D_{KL}\left(\mathcal{E}_{E_3} \| \mathcal{E}_{E_1}\right) = 0.626$ nats, versus $D_{KL}\left(\mathcal{E}_{E_1} \| \mathcal{E}_{control}\right) = 1.26$ nats. Despite the demonstrated decrease in the marginal benefits of isotopic information, we have established that the two isotopic data sets, when assimilated simulataneously with the two contraints of the non-isotopic data sets, provide a full additional constraint. When only one isotopic data set was assimilated, however, only modest gains in information content were achieved (0.177 nats). Additionally, the biases in isotope-based transpiration fraction worsened when data from an additional isotopic species was introduced to the calibration data set (experiment E3 versus E2, Table 4.2). These results point to the large amount of uncertainty in isotopic data, and particularly the deuterium excess which depends on poorly understood kinetic fractionation processes, serving as a hindrance to its practical use.

Similarly to the calibration experiments from Chapter 2, the posterior distributions for model parameters were not centered at one, and none contained one in their 95% credible intervals. Even more striking was the fact that out of 1218 days of data and two isotopic species, in the

control model configuration only a single day for one isotopic species' model output yielded a physically reasonable isotope-based partitioning estimate ($0 \leq f_{T,i} \leq 1$). By contrast, in the posterior ensemble experiments, nearly all of the daily averages for both isotopic species for all ensemble members produced plausible isotope-based transpiration fractions. While this was not the intention of the ensemble experiments, this result underscores the fact that no model is perfect, and iCLM4 is no exception. Therefore some form of calibration to observational data is not a luxury, but rather a necessity for any physical model. Despite the fact that the control model behavior yielded nearly complete nonsense, through the model calibration framework implemented here, the isotope-based model partitioning and direct (true) model partitioning were reconciled for summer (growing season) months.

5.4 Summary and critical points

The poor performance of the calibrated CLM4 model simulating early season snowmelt at MEF (Chapter 2), BAO soil moisture data assimilation experiment and coupled global sensitivity experiments (Chapter 3) revealed that soil hydrological modeling is critical for accurate model representation not only of the land surface and its water pool isotope ratios, but of the global climate system as well. Errors in modeled soil moisture leak into all other model compartments through evaporation, root uptake and transpiration, and runoff. This is an area ripe with opportunity for land surface model improvement, which will positively affect the global climate system, as seen in the comparisons of Section 3.3.2. The BAO soil moisture data assimilation experiment indicated that a potential avenue to fix these errors and biases is a global soil moisture data assimilation experiment. Satellite-based soil moisture data products such as the European Space Agency's Soil Moisture and Ocean Salinity (SMOS, [73]) and the National Aeronautics and Space Administration's Soil Moisture Active Passive (SMAP, [32]) programs offer viable options for assimilation data. Other possible model modifications which are likely to yield improvements include the incorporation of below-ground soil vapor diffusion and/or setting the evaporation source water as the top 20–30 cm of soil water, and the isotope ratio of evaporation source water to an integrated isotope ratio,

representative of this evaporation front [130, 92]. While CLM4 draws evaporation from the top soil layer only, it is well-documented that this is not true in nature [43, 130, 92].

The single column land surface model calibration experiment presented in Chapters 2 and 4 highlighted the fact that improved calibration procedures for physical models is a need, not a luxury. Chapter 2 demonstrated that if biases and errors are not properly accounted for, they will be detrimental to model performance, and confound posterior estimates of model parameters and physical quantities of interest (i.e., transpiration fraction, f_T). Chapter 4 showed that without calibration, the model output would have yielded almost entirely unphysical results for the isotope-based f_T estimates. After calibration, however, a posterior ensemble of model simulations produced isotope-based partitioning which agreed well with direct model partitioning for the central Colorado growing season. Whereas no observational campaign will ever have a known true value for f_T against which to compare partitioning derived from water isotope ratios, the experiments presented here compared modeled water isotope ratio-based ET partitioning estimates to the directly modeled partitioning, which is the known truth within the model realization. In this way, the present work has shown that on a growing season time scale, at the semiarid grassland BAO site, stable water isotope ratios provide robust estimates of ET partitioning.

While the simple landscape at the BAO site may not be representative of the global landscape as a whole, these experiments may be reproduced for a representative network of sites scattered on a regional scale, to create calibrated regional surface data sets and calibrated model predictions. With the advent of widely available high quality tower data for validation and calibration of land surface models [71], as well as the proliferation of field-deployable laser spectroscopic instruments for obtaining high-quality and high-frequency measurements of stable water isotope ratios, there are increasing opportunities for assimilating models and hydrological, meteorological and isotopic data. Tower data, collected at a network of sites representative of the larger regional or global landscape, would permit a large spatial scale model calibration approach at a lower computational cost. It will undoubtedly remain critical to utilize both quality observations and advanced modeling frameworks to the fullest extent of their abilities.

Bibliography

[1] F Aemisegger, JK Spiegel, S Pfahl, H Sodemann, W Eugster, and H Wernli. Isotope meteorology of cold front passages: A case study combining observations and modeling. Geophysical Research Letters, 42(13):5652–5660, 2015.

[2] Amy T Austin, Laura Yahdjian, John M Stark, Jayne Belnap, Amilcare Porporato, Urszula Norton, Damián A Ravetta, and Sean M Schaeffer. Water pulses and biogeochemical cycles in arid and semiarid ecosystems. Oecologia, 141(2):221–235, 2004.

[3] Dennis D Baldocchi, Bruce B Hicks, and Pamela Camara. A canopy stomatal resistance model for gaseous deposition to vegetated surfaces. Atmos. Environ. (1967), 21(1):91–101, 1987.

[4] Dennis D Baldocchi, Bruce B Hicks, and Tilden P Meyers. Measuring biosphere-atmosphere exchanges of biologically related gases with micrometeorological methods. Ecology, pages 1331–1340, 1988.

[5] JT Ball and JA Berry. An analysis and concise description of stomatal responses to multiple environmental factors. Planta, 1991.

[6] CJ Barnes and GB Allison. The distribution of deuterium and ^{18}O in dry soils: 1. theory. J. Hydrol., 60(1):141–156, 1983.

[7] Christian Beer, Markus Reichstein, Enrico Tomelleri, Philippe Ciais, Martin Jung, Nuno Carvalhais, Christian Rödenbeck, M Altaf Arain, Dennis Baldocchi, Gordon B Bonan, et al. Terrestrial gross carbon dioxide uptake: global distribution and covariation with climate. Science, 329(5993):834–838, 2010.

[8] M Berkelhammer, J Hu, A Bailey, DC Noone, CJ Still, H Barnard, D Gochis, GS Hsiao, T Rahn, and A Turnipseed. The nocturnal water cycle in an open-canopy forest. J. Geophys. Res. Atmos., 118(17):10–225, 2013.

[9] Gordon B Bonan. Land surface model (LSM version 1.0) for ecological, hydrological, and atmospheric studies: Technical description and users guide. Technical note. Technical report, National Center for Atmospheric Research, Boulder, CO (United States). Climate and Global Dynamics Div., 1996.

[10] Gordon B Bonan, Peter J Lawrence, Keith W Oleson, Samuel Levis, Martin Jung, Markus Reichstein, David M Lawrence, and Sean C Swenson. Improving canopy processes in the community land model version 4 (clm4) using global flux fields empirically inferred from fluxnet data. Journal of Geophysical Research: Biogeosciences, 116(G2), 2011.

[11] Gordon B Bonan, Keith W Oleson, Rosie A Fisher, Gitta Lasslop, and Markus Reichstein. Reconciling leaf physiological traits and canopy flux data: Use of the TRY and FLUXNET databases in the Community Land Model Version 4. J. Geophys. Res. Biogeo. (2005–2012), 117(G2), 2012.

[12] Isabelle Braud, Thierry Bariac, Jean Paul Gaudet, and Michel Vauclin. Sispat-isotope, a coupled heat, water and stable isotope (hdo and h¡ sub¿ 2¡/sub¿¡ sup¿ 18¡/sup¿ o) transport model for bare soil. part i. model description and first verifications. J. Hydrol., 309(1):277–300, 2005.

[13] David D Breshears. The grassland-forest continuum: trends in ecosystem properties for woody plant mosaics? Front. Ecol. Environ., 4(2):96–104, 2006.

[14] NA Brunsell. A multiscale information theory approach to assess spatial–temporal variability of daily precipitation. Journal of Hydrology, 385(1):165–172, 2010.

[15] Wilfried Brutsaert. A theory for local evaporation (or heat transfer) from rough and smooth surfaces at ground level. Water Resour. Res., 11(4):543–550, 1975.

[16] Wilfried Brutsaert. Evaporation into the atmosphere: theory, history, and applications. Reidel Dordrecht, 1982.

[17] Nikolaus Buenning, David Noone, James Randerson, William J Riley, and Christopher Still. The response of the $^{18}O/^{16}O$ composition of atmospheric CO_2 to changes in environmental conditions. J. Geophys. Res. Biogeosci., 119(1):55–79, 2014.

[18] Christopher D Cappa, Melissa B Hendricks, Donald J DePaolo, and Ronald C Cohen. Isotopic fractionation of water during evaporation. J. Geophys. Res. Atmos. (1984–2012), 108(D16), 2003.

[19] Michelle L Cavanaugh, Shirley A Kurc, and Russell L Scott. Evapotranspiration partitioning in semiarid shrubland ecosystems: a two-site evaluation of soil moisture control on transpiration. Ecohydrology, 4(5):671–681, 2011.

[20] Lucas A Cernusak, Graham D Farquhar, and John S Pate. Environmental and physiological controls over oxygen and carbon isotope composition of tasmanian blue gum, eucalyptus globulus. Tree Physiology, 25(2):129–146, 2005.

[21] Bhaskar J Choudhury and Nicolo E DiGirolamo. A biophysical process-based estimate of global land surface evaporation using satellite and ancillary data i. model description and comparison with observations. J. Hydrol., 205(3):164–185, 1998.

[22] Roger B Clapp and George M Hornberger. Empirical equations for some soil hydraulic properties. Water Resour. Res., 14(4):601–604, 1978.

[23] G James Collatz, J Timothy Ball, Cyril Grivet, and Joseph A Berry. Physiological and environmental regulation of stomatal conductance, photosynthesis and transpiration: a model that includes a laminar boundary layer. Agric. For. Meteorol., 54(2):107–136, 1991.

[24] Harmon Craig and Louis Irwin Gordon. Deuterium and oxygen 18 variations in the ocean and the marine atmosphere. In E. Tongiorgi, editor, Stable Isotopes in Oceanographic Studies and Paleotemperatures, Lischi and Figli, Pisa, Italy, pages 9–130, 1965.

[25] NN Das, BP Mohanty, and EG Njoku. A Markov chain Monte Carlo algorithm for upscaled soil-vegetation-atmosphere-transfer modeling to evaluate satellite-based soil moisture measurements. Water Resour. Res., 44(5), 2008.

[26] Jean Dauzat, Bruno Rapidel, and Andre Berger. Simulation of leaf transpiration and sap flow in virtual plants: Model description and application to a coffee plantation in Costa Rica. Agric. For. Meteorol., 109(2):143–160, 2001.

[27] Todd E Dawson and James R Ehleringer. Streamside trees that do not use stream water. Nature, 350(6316):335–337, 1991.

[28] JP DiGangi, ES Boyle, T Karl, P Harley, A Turnipseed, S Kim, C Cantrell, RL Maudlin III, W Zheng, F Flocke, et al. First direct measurements of formaldehyde flux via eddy covariance: Implications for missing in-canopy formaldehyde sources. Atmos. Chem. Phys., 11(20):10565–10578, 2011.

[29] Paul A Dirmeyer, Xiang Gao, Mei Zhao, Zhichang Guo, Taikan Oki, Naota Hanasaki, et al. The second Global Soil Wetness Project (GSWP-2): Multi-model analysis and implications for our perception of the land surface, volume 185. Center for Ocean-Land-Atmosphere Studies, 2005.

[30] FX Dunin. Extrapolation of point measurements of evaporation: Some issues of scale. In Vegetation and climate interactions in semi-arid regions, pages 39–47. Springer, 1991.

[31] James R Ehleringer, Christopher B Field, et al. Scaling physiological processes: Leaf to globe. Academic Press, 1993.

[32] Dara Entekhabi, Eni G Njoku, Peggy EO Neill, Kent H Kellogg, Wade T Crow, Wendy N Edelstein, Jared K Entin, Shawn D Goodman, Thomas J Jackson, Joel Johnson, et al. The soil moisture active passive (smap) mission. Proceedings of the IEEE, 98(5):704–716, 2010.

[33] RLH Essery, MJ Best, RA Betts, Peter M Cox, and Christopher M Taylor. Explicit representation of subgrid heterogeneity in a GCM land surface scheme. J. Hydrometeorol., 4(3):530–543, 2003.

[34] GD Farquhar and J Lloyd. Carbon and oxygen isotope effects in the exchange of carbon dioxide between terrestrial plants and the atmosphere. Stable isotopes and plant carbon-water relations, 40:47–70, 1993.

[35] DF Ferretti, E Pendall, JA Morgan, JA Nelson, Daniel Lecain, and AR Mosier. Partitioning evapotranspiration fluxes from a Colorado grassland using stable isotopes: seasonal variations and ecosystem implications of elevated atmospheric CO2. Plant and Soil, 254(2):291–303, 2003.

[36] Lawrence B Flanagan, Jonathan P Comstock, and James R Ehleringer. Comparison of modeled and observed environmental influences on the stable oxygen and hydrogen isotope composition of leaf water in phaseolus vulgaris l. Plant Physiol., 96(2):588–596, 1991.

[37] G Flato, Jochem Marotzke, B Abiodun, P Braconnot, S Chan Chou, W Collins, P Cox, F Driouech, S Emori, V Eyring, et al. Evaluation of climate models. In Climate change 2013: the physical science basis. Contribution of Working Group I to the Fifth Assessment Report

of the Intergovernmental Panel on Climate Change, pages 741–866. Cambridge University Press, 2013.

[38] DC Frank, B Poulter, M Saurer, J Esper, C Huntingford, G Helle, K Treydte, NE Zimmermann, GH Schleser, Anders Ahlström, et al. Water-use efficiency and transpiration across european forests during the anthropocene. Nature Climate Change, 5(6):579–583, 2015.

[39] MR Gale and DF Grigal. Vertical root distributions of northern tree species in relation to successional status. Canadian Journal of Forest Research, 17(8):829–834, 1987.

[40] A Gelman, G Roberts, and W Gilks. Efficient Metropolis jumping rules. Bayesian Statistics, 5:599–608, 1996.

[41] Andrew Gelman and Donald B Rubin. Inference from iterative simulation using multiple sequences. Statistical Science, pages 457–472, 1992.

[42] Charles J Geyer. Markov chain Monte Carlo maximum likelihood. 1991.

[43] Stephen P Good, David Noone, Naoyuki Kurita, Marion Benetti, and Gabriel J Bowen. D/H isotope ratios in the global hydrologic cycle. Geophysical Research Letters, 42(12):5042–5050, 2015.

[44] Stephen P Good, Keir Soderberg, Lixin Wang, and Kelly K Caylor. Uncertainties in the assessment of the isotopic composition of surface fluxes: A direct comparison of techniques using laser-based water vapor isotope analyzers. J. Geophys. Res. Atmos. (1984–2012), 117(D15), 2012.

[45] Timothy J Griffis. Tracing the flow of carbon dioxide and water vapor between the biosphere and atmosphere: A review of optical isotope techniques and their application. Agricultural and Forest Meteorology, 174:85–109, 2013.

[46] Hoshin Vijai Gupta, Soroosh Sorooshian, and Patrice Ogou Yapo. Toward improved calibration of hydrologic models: Multiple and noncommensurable measures of information. Water Resour. Res., 34(4):751–763, 1998.

[47] HV Gupta, LA Bastidas, S Sorooshian, WJ Shuttleworth, and ZL Yang. Parameter estimation of a land surface scheme using multicriteria methods. J. Geophys. Res. Atmos. (1984–2012), 104(D16):19491–19503, 1999.

[48] Priya Gupta, David Noone, Joseph Galewsky, Colm Sweeney, and Bruce H Vaughn. Demonstration of high-precision continuous measurements of water vapor isotopologues in laboratory and remote field deployments using wavelength-scanned cavity ring-down spectroscopy (WS-CRDS) technology. Rapid communications in mass spectrometry, 23(16):2534–2542, 2009.

[49] Heikki Haario, Eero Saksman, and Johanna Tamminen. An adaptive Metropolis algorithm. Bernoulli, pages 223–242, 2001.

[50] James Hansen, Larissa Nazarenko, Reto Ruedy, Makiko Sato, Josh Willis, Anthony Del Genio, Dorothy Koch, Andrew Lacis, Ken Lo, Surabi Menon, et al. Earth's energy imbalance: Confirmation and implications. science, 308(5727):1431–1435, 2005.

[51] Oleksandra Hararuk, Jianyang Xia, and Yiqi Luo. Evaluation and improvement of a global land model against soil carbon data using a Bayesian Markov chain Monte Carlo method. J. Geophys. Res. Biogeo., 119(3):403–417, 2014.

[52] Peter Hartmann and Klaus von Wilpert. Fine-root distributions of central european forest soils and their interaction with site and soil properties. Can. J. For. Res., 44(1):71–81, 2013.

[53] W Keith Hastings. Monte Carlo sampling methods using Markov chains and their applications. Biometrika, 57(1):97–109, 1970.

[54] A Henderson-Sellers, M Fischer, I Aleinov, K McGuffie, WJ Riley, GA Schmidt, K Sturm, K Yoshimura, and P Irannejad. Stable water isotope simulation by current land-surface schemes: Results of iPILPS Phase 1. Global and Planetary change, 51(1):34–58, 2006.

[55] Dave Higdon, Marc Kennedy, James C Cavendish, John A Cafeo, and Robert D Ryne. Combining field data and computer simulations for calibration and prediction. SIAM J. Sci. Comput., 26(2):448–466, 2004.

[56] Juske Horita and David J Wesolowski. Liquid-vapor fractionation of oxygen and hydrogen isotopes of water from the freezing to the critical temperature. Geochim. Cosmochim. Acta, 58(16):3425–3437, 1994.

[57] Zhangshuan Hou, Maoyi Huang, L Ruby Leung, Guang Lin, and Daniel M Ricciuto. Sensitivity of surface flux simulations to hydrologic parameters based on an uncertainty quantification framework applied to the Community Land Model. Journal of Geophysical Research: Atmospheres, 117(D15), 2012.

[58] Zhongmin Hu, Xuefa Wen, Xiaomin Sun, Linghao Li, Guirui Yu, Xuhui Lee, and Shenggong Li. Partitioning of evapotranspiration through oxygen isotopic measurements of water pools and fluxes in a temperate grassland. J. Geophys. Res. Biogeo., 119(3):358–372, 2014.

[59] James W Hurrell, Marika M Holland, Peter R Gent, S Ghan, Jennifer E Kay, PJ Kushner, J-F Lamarque, William G Large, D Lawrence, Keith Lindsay, et al. The Community Earth System Model: A framework for collaborative research. Bull. Am. Meteorol. Soc., 94(9):1339–1360, 2013.

[60] IAEA/WMO. International atomic energy agency (iaea). environmental isotope data no. 1-10: World survey of isotope concentration in precipitation, 1994.

[61] IAEA/WMO. Moisture isotopes in the biosphere and atmosphere, the MIBA database. Accessible at: http://www.iaea.org/water, 1994.

[62] IAEA/WMO. Global network of isotopes in rivers, the GNIR database. Accessible at: http://www.iaea.org/water, 2015.

[63] Robert B Jackson, Laurel J Anderson, and William T Pockman. Measuring water availability and uptake in ecosystem studies. Methods in Ecosystem Science, pages 199–214, 2000.

[64] PG Jarvis. Scaling processes and problems. Plant, Cell & Environment, 18(10):1079–1089, 1995.

[65] Scott Jasechko, Zachary D Sharp, John J Gibson, S Jean Birks, Yi Yi, and Peter J Fawcett. Terrestrial water fluxes dominated by transpiration. Nature, 2013.

[66] Martin Jung, Markus Reichstein, Philippe Ciais, Sonia I Seneviratne, Justin Sheffield, Michael L Goulden, Gordon Bonan, Alessandro Cescatti, Jiquan Chen, Richard de Jeu, et al. Recent decline in the global land evapotranspiration trend due to limited moisture supply. Nature, 467(7318):951–954, 2010.

[67] Lisa C Kanner, Nikolaus H Buenning, Lowell D Stott, Axel Timmermann, and David Noone. The role of soil processes in δ^{18}O terrestrial climate proxies. Global Biogeochem. Cycles, 28(3):239–252, 2014.

[68] A Kaushik. private communication, 16 January 2016.

[69] A Kaushik, MB Berkelhammer, M O'Neill, and DC Noone. The importance of sub-surface exchange in refining evapotranspiration fluxes in a semi-arid environment. J. Geophys. Res.: Atm., in prep.

[70] Charles D Keeling. The concentration and isotopic abundances of atmospheric carbon dioxide in rural areas. Geochim. Cosmochim. Acta, 13(4):322–334, 1958.

[71] Michael Keller, David S Schimel, William W Hargrove, and Forrest M Hoffman. A continental strategy for the National Ecological Observatory Network. Frontiers in Ecology and the Environment, 6(5):282–284, 2008.

[72] Marc C Kennedy and Anthony O'Hagan. Bayesian calibration of computer models. J. R. Statist. Soc. B, 63(3):425–464, 2001.

[73] Yann H Kerr, Philippe Waldteufel, Jean-Pierre Wigneron, Steven Delwart, François Ois Cabot, Jacqueline Boutin, Maria-José Escorihuela, Jordi Font, Nicolas Reul, Claire Gruhier, et al. The smos mission: New tool for monitoring key elements ofthe global water cycle. Proceedings of the IEEE, 98(5):666–687, 2010.

[74] S Kim, T Karl, A Guenther, G Tyndall, J Orlando, P Harley, R Rasmussen, and E Apel. Emissions and ambient distributions of biogenic volatile organic compounds (BVOC) in a ponderosa pine ecosystem: interpretation of PTR-MS mass spectra. Atmos. Chem. Phys., 10(4):1759–1771, 2010.

[75] Reto Knutti, David Masson, and Andrew Gettelman. Climate model genealogy: Generation CMIP5 and how we got there. Geophysical Research Letters, 40(6):1194–1199, 2013.

[76] Randal D Koster, Paul A Dirmeyer, Zhichang Guo, Gordon Bonan, Edmond Chan, Peter Cox, CT Gordon, Shinjiro Kanae, Eva Kowalczyk, David Lawrence, et al. Regions of strong coupling between soil moisture and precipitation. Science, 305(5687):1138–1140, 2004.

[77] S Kullback. Statistics and Information Theory, 1959.

[78] Solomon Kullback and Richard A Leibler. On information and sufficiency. The annals of mathematical statistics, 22(1):79–86, 1951.

[79] Shirley A Kurc and Eric E Small. Dynamics of evapotranspiration in semiarid grassland and shrubland ecosystems during the summer monsoon season, central new mexico. Water Resour. Res., 40(9), 2004.

[80] Naoyuki Kurita, Kimpei Ichiyanagi, Jun Matsumoto, Manabu D Yamanaka, and Tetsuo Ohata. The relationship between the isotopic content of precipitation and the precipitation amount in tropical regions. Journal of Geochemical Exploration, 102(3):113–122, 2009.

[81] JJ Landsberg and DBB Powell. Surface exchange characteristics of leaves subject to mutual interference. Agric. Meteorol., 12:169–184, 1973.

[82] David M Lawrence, Keith W Oleson, Mark G Flanner, Peter E Thornton, Sean C Swenson, Peter J Lawrence, Xubin Zeng, Zong-Liang Yang, Samuel Levis, Koichi Sakaguchi, et al. Parameterization improvements and functional and structural advances in version 4 of the Community Land Model. J. Adv. Model. Earth Syst., 3(1), 2011.

[83] David M Lawrence, Peter E Thornton, Keith W Oleson, and Gordon B Bonan. The partitioning of evapotranspiration into transpiration, soil evaporation, and canopy evaporation in a GCM: Impacts on land-atmosphere interaction. J. Hydrometeorol., 8(4):862–880, 2007.

[84] Xuhui Lee, Tim J Griffis, John M Baker, Kaycie A Billmark, Kyounghee Kim, and Lisa R Welp. Canopy-scale kinetic fractionation of atmospheric carbon dioxide and water vapor isotopes. Global Biogeochem. Cycles, 23(1), 2009.

[85] Xuhui Lee, Jianping Huang, and Edward G Patton. A large-eddy simulation study of water vapour and carbon dioxide isotopes in the atmospheric boundary layer. Boundary-layer meteorology, 145(1):229–248, 2012.

[86] William A Link and Mitchell J Eaton. On thinning of chains in MCMC. Methods Ecol. Evol., 3(1):112–115, 2012.

[87] G Lis, L I Wassenaar, and M J Hendry. High-precision laser spectroscopy D/H and $^{18}O/^{16}O$ measurements of microliter natural water samples. Anal. Chem., 80(1):287–293, 2008.

[88] Beiling Liu, Fred Phillips, Susan Hoines, Andrew R Campbell, and Pankaj Sharma. Water movement in desert soil traced by hydrogen and oxygen isotopes, chloride, and chlorine-36, southern arizona. J. Hydrol., 168(1):91–110, 1995.

[89] Shaomin Liu, L Lu, D Mao, L Jia, et al. Evaluating parameterizations of aerodynamic resistance to heat transfer using field measurements. Hydrol. Earth Syst. Sci. Discuss., 11(2):769–783, 2007.

[90] Yuqiong Liu, Hoshin V Gupta, Soroosh Sorooshian, Luis A Bastidas, and William J Shuttleworth. Constraining land surface and atmospheric parameters of a locally coupled model using observational data. J. Hydrometeorol., 6(2):156–172, 2005.

[91] WJ Massman, JM Frank, WD Shepperd, MJ Platten, Philip N Omi, and Linda A Joyce. In situ soil temperature and heat flux measurements during controlled surface burns at a southern Colorado forest site. In Fire, Fuel Treatments, and Ecological Restoration (vp). 16-18 Apr, USDA Forest Service Rocky Mountain Research Station, 2150 Centre Avenue Fort Collins CO 80526 USA, 2002.

[92] Renaud Mathieu and Thierry Bariac. A numerical model for the simulation of stable isotope profiles in drying soils. J. Geophys. Res., 101(D7):12685–12, 1996.

[93] Liliane Merlivat. Molecular diffusivities of $H_2^{16}O$, HDO, and $H_2^{18}O$ in gases. J. Chem. Phys., 69:2864, 1978.

[94] Liliane Merlivat and Jean Jouzel. Global climatic interpretation of the deuterium-oxygen 18 relationship for precipitation. Journal of Geophysical Research: Oceans, 84(C8):5029–5033, 1979.

[95] Nicholas Metropolis, Arianna W Rosenbluth, Marshall N Rosenbluth, Augusta H Teller, and Edward Teller. Equation of state calculations by fast computing machines. J. Chem. Phys., 21:1087, 1953.

[96] Jessica W Moerman, Kim M Cobb, Jess F Adkins, Harald Sodemann, Brian Clark, and Andrew A Tuen. Diurnal to interannual rainfall δ18O variations in northern Borneo driven by regional hydrology. Earth and Planetary Science Letters, 369:108–119, 2013.

[97] Hamid Moradkhani, Caleb M DeChant, and Soroosh Sorooshian. Evolution of ensemble data assimilation for uncertainty quantification using the particle filter-Markov chain Monte Carlo method. Water Resour. Res., 48(12), 2012.

[98] Marcelo Moreira, Leonel Sternberg, Luiz Martinelli, Reynaldo Victoria, Edelcilio Barbosa, Luiz Bonates, and Daniel Nepstad. Contribution of transpiration to forest ambient vapour based on isotopic measurements. Global Change Biol., 3(5):439–450, 1997.

[99] Grey S Nearing and Hoshin V Gupta. The quantity and quality of information in hydrologic models. Water Resources Research, 51(1):524–538, 2015.

[100] D. Noone, W. Riley, C. Still, and J. Randerson. Diagnosing impacts of changes in the biosphere by modeling ^{18}O in atmospheric CO_2 with a general circulation model. In The 6th International CO2 Conference, Sendai, Japan, number LBNL-50311, pages 6–10, 2001.

[101] D Noone, C Risi, A Bailey, M Berkelhammer, DP Brown, N Buenning, S Gregory, J Nusbaumer, D Schneider, J Sykes, et al. Determining water sources in the boundary layer from tall tower profiles of water vapor and surface water isotope ratios after a snowstorm in colorado. Atmos. Chem. Phys. Discuss, 12:16327–16375, 2012.

[102] J Nusbaumer, TE Wong, C Bardeen, and DC Noone. Evaluating hydrological processes in the Community Atmosphere Model Version 5 (CAM5) using stable isotope ratios of water. Journal of Climate, in prep.

[103] K.W. Oleson, D.M. Lawrence, G.B. Bonan, M.G. Flanner, E. Kluzek, P.J. Lawrence, S. Levis, S.C. Swenson, P.E. Thornton, A. Dai, M. Decker, R. Dickinson, J. Feddema, C.L. Heald, F. Hoffman, J.-F. Lamarque, N. Mahowald, G.-Y. Niu, T. Qian, J. Randerson, S. Running, K. Sakaguchi, A. Slater, R. Stockli, A. Wang, Z.-L. Yang, Xi. Zeng, and Xu. Zeng. Coauthors, 2010: Technical description of version 4.0 of the Community Land Model (CLM). Technical report, NCAR Technical Note NCAR/TN-4781STR, 2010.

[104] J Ortega, A Turnipseed, AB Guenther, TG Karl, DA Day, D Gochis, JA Huffman, AJ Prenni, EJT Levin, SM Kreidenweis, et al. Overview of the Manitou Experimental Forest Observatory: site description and selected science results from 2008 to 2013. Atmos. Chem. Phys., 14(12):6345–6367, 2014.

[105] Prajjwal K Panday, Christopher A Williams, Karen E Frey, and Molly E Brown. Application and evaluation of a snowmelt runoff model in the Tamor River basin, Eastern Himalaya using a Markov chain Monte Carlo (MCMC) data assimilation approach. Hydrol. Processes, 28(21):5337–5353, 2014.

[106] Robert W Pearcy, James R Ehleringer, Harold A Mooney, Philip W Rundel, et al. Plant physiological ecology: Field methods and instrumentation. Chapman and Hall Ltd, 1989.

[107] David A Randall, Richard A Wood, Sandrine Bony, Robert Colman, Thierry Fichefet, John Fyfe, Vladimir Kattsov, Andrew Pitman, Jagadish Shukla, Jayaraman Srinivasan, et al. Climate models and their evaluation. In Climate Change 2007: The physical science basis. Contribution of Working Group I to the Fourth Assessment Report of the IPCC (FAR), pages 589–662. Cambridge University Press, 2007.

[108] WJ Riley, CJ Still, MS Torn, and JA Berry. A mechanistic model of $H_2^{18}O$ and $C^{18}OO$ fluxes between ecosystems and the atmosphere: Model description and sensitivity analyses. Global Biogeochem. Cycles, 16(4):1095, 2002.

[109] Johan Rockström, Malin Falkenmark, Louise Karlberg, Holger Hoff, Stefanie Rost, and Dieter Gerten. Future water availability for global food production: the potential of green water for increasing resilience to global change. Water Resour. Res., 45(7), 2009.

[110] John S Roden, Guanghui Lin, and James R Ehleringer. A mechanistic model for interpretation of hydrogen and oxygen isotope ratios in tree-ring cellulose. Geochimica et Cosmochimica Acta, 64(1):21–35, 2000.

[111] Youri Rothfuss, Philippe Biron, Isabelle Braud, Laurent Canale, Jean-Louis Durand, Jean-Paul Gaudet, Patricia Richard, Michel Vauclin, and Thierry Bariac. Partitioning evapotranspiration fluxes into soil evaporation and plant transpiration using water stable isotopes under controlled conditions. Hydrol. Processes, 24(22):3177–3194, 2010.

[112] Koichi Sakaguchi and Xubin Zeng. Effects of soil wetness, plant litter, and under-canopy atmospheric stability on ground evaporation in the Community Land Model (CLM3.5). J. Geophys. Res. Atmos. (1984–2012), 114(D1), 2009.

[113] TW Sammis and LW Gay. Evapotranspiration from an arid zone plant community. J. Arid. Environ., 2(4), 1979.

[114] Sean M Schaeffer, David G Williams, and David C Goodrich. Transpiration of cottonwood/willow forest estimated from sap flux. Agric. For. Meteorol., 105(1):257–270, 2000.

[115] William H Schlesinger and Scott Jasechko. Transpiration in the global water cycle. Agric. For. Meteorol., 189:115–117, 2014.

[116] RJ Scholes and SR Archer. Tree-grass interactions in savannas. Annual review of Ecology and Systematics, pages 517–544, 1997.

[117] U Seibt, L Wingate, JA Berry, and Jon Lloyd. Non-steady state effects in diurnal 18O discrimination by picea sitchensis branches in the field. Plant, Cell & Environment, 29(5):928–939, 2006.

[118] Michael K Stewart. Stable isotope fractionation due to evaporation and isotopic exchange of falling waterdrops: Applications to atmospheric processes and evaporation of lakes. J. Geophys. Res., 80(9):1133–1146, 1975.

[119] SJ Sutanto, B Van den Hurk, PA Dirmeyer, SI Seneviratne, T Rockmann, KE Trenberth, EM Blyth, J Wenninger, and G Hoffmann. HESS opinions: a perspective on isotope versus non-isotope approaches to determine the contribution of transpiration to total evaporation. Hydrology and Earth System Sciences, 18(8):2815–2827, 2014.

[120] JY Tang, WJ Riley, CD Koven, and ZM Subin. CLM4-BeTR, a generic biogeochemical transport and reaction module for CLM4: model development, evaluation, and application. Geoscientific Model Development, 6(1):127–140, 2013.

[121] Thordis L Thorarinsdottir, Tilmann Gneiting, and Nadine Gissibl. Using proper divergence functions to evaluate climate models. SIAM/ASA Journal on Uncertainty Quantification, 1(1):522–534, 2013.

[122] Hanqin Tian, Guangsheng Chen, Mingliang Liu, Chi Zhang, Ge Sun, Chaoqun Lu, Xiaofeng Xu, Wei Ren, Shufen Pan, and Arthur Chappelka. Model estimates of net primary productivity, evapotranspiration, and water use efficiency in the terrestrial ecosystems of the southern united states during 1895–2007. Forest Ecology and Management, 259(7):1311–1327, 2010.

[123] Guillaume Tremoy, Françoise Vimeux, Olivier Cattani, Salla Mayaki, Ide Souley, and Guillaume Favreau. Measurements of water vapor isotope ratios with wavelength-scanned cavity ring-down spectroscopy technology: new insights and important caveats for deuterium excess measurements in tropical areas in comparison with isotope-ratio mass spectrometry. Rapid Communications in Mass Spectrometry, 25(23):3469–3480, 2011.

[124] Kevin E Trenberth, John T Fasullo, and Jessica Mackaro. Atmospheric moisture transports from ocean to land and global energy flows in reanalyses. Journal of Climate, 24(18):4907–4924, 2011.

[125] Kevin E Trenberth and David P Stepaniak. The flow of energy through the earth's climate system. Quarterly Journal of the Royal Meteorological Society, 130(603):2677–2701, 2004.

[126] Tracy E Twine, WP Kustas, JM Norman, DR Cook, PR Houser, TP Meyers, JH Prueger, PJ Starks, and ML Wesely. Correcting eddy-covariance flux underestimates over a grassland. Agric. For. Meteorol., 103(3):279–300, 2000.

[127] J Twining, D Stone, C Tadros, A Henderson-Sellers, and A Williams. Moisture Isotopes in the Biosphere and Atmosphere (MIBA) in Australia: A priori estimates and preliminary observations of stable water isotopes in soil, plant and vapour for the Tumbarumba Field Campaign. Global and Planetary Change, 51(1):59–72, 2006.

[128] M Vertenstein, A Middleton, D Feddema, et al. Community Climate System Model CESM1.0.3 User Guide, available at: http://www.cesm.ucar.edu/models/cesm1.0/cesm/cesm_doc_1_0_4/ug.pdf. National Center of Atmospheric Research, 2010.

[129] Tomas Vitvar, Pradeep K Aggarwal, and Andrew L Herczeg. Global network is launched to monitor isotopes in rivers. Eos, Transactions American Geophysical Union, 88(33):325–326, 2007.

[130] Lixin Wang, Kelly K Caylor, Juan Camilo Villegas, Greg A Barron-Gafford, David D Breshears, and Travis E Huxman. Partitioning evapotranspiration across gradients of woody plant cover: Assessment of a stable isotope technique. Geophys. Res. Lett., 37(9):L09401, 2010.

[131] Xue-Feng Wang and Dan Yakir. Using stable isotopes of water in evapotranspiration studies. Hydrol. Processes, 14(8):1407–1421, 2000.

[132] Leonard I Wassenaar, Tyler B Coplen, and Pradeep K Aggarwal. Approaches for achieving long-term accuracy and precision of δ18o and δ2h for waters analyzed using laser absorption spectrometers. Environmental science & technology, 48(2):1123–1131, 2014.

[133] DG Williams, W Cable, K Hultine, JCB Hoedjes, EA Yepez, V Simonneaux, S Er-Raki, G Boulet, HAR De Bruin, A Chehbouni, et al. Evapotranspiration components determined by stable isotope, sap flow and eddy covariance techniques. Agric. For. Meteorol., 125(3):241–258, 2004.

[134] Kell B Wilson, Paul J Hanson, Patrick J Mulholland, Dennis D Baldocchi, and Stan D Wullschleger. A comparison of methods for determining forest evapotranspiration and its components: sap-flow, soil water budget, eddy covariance and catchment water balance. Agric. For. Meteorol., 106(2):153–168, 2001.

[135] TE Wong, W Kleiber, and DC Noone. A demonstration of the impact of error accounting in a bayesian approach to calibrating modeled turbulent fluxes in an alpine forest. Water Resources Research, in review.

[136] TE Wong, J Nusbaumer, and DC Noone. Evaluation of modeled land-atmosphere exchanges with a comprehensive water isotope fractionation scheme in version 4 of the Community Land Model (CLM4). Journal of Climate, in prep.

[137] Qin Xu. Measuring information content from observations for data assimilation: Relative entropy versus Shannon entropy difference. Tellus A, 59(2):198–209, 2007.

[138] Tao Xu, Luther White, Dafeng Hui, and Yiqi Luo. Probabilistic inversion of a terrestrial ecosystem model: Analysis of uncertainty in parameter estimation and model prediction. Global Biogeochem. Cycles, 20(2), 2006.

[139] Zhen Xu, HB Yang, FD Liu, SQ An, Jun Cui, ZS Wang, and SR Liu. Partitioning evapotranspiration flux components in a subalpine shrubland based on stable isotopic measurements. Botanical Studies, 49(4):351–361, 2008.

[140] Dan Yakir and Lionel Sternberg. The use of stable isotopes to study ecosystem gas exchange. Oecologia, 123(3):297–311, 2000.

[141] Enrico A Yepez, David G Williams, Russell L Scott, and Guanghui Lin. Partitioning overstory and understory evapotranspiration in a semiarid savanna woodland from the isotopic composition of water vapor. Agric. For. Meteorol., 119(1):53–68, 2003.

[142] Steven E Yochum. Colorado Front Range Flood of 2013: Peak Flows and Flood Frequencies. In Proceedings of the 3rd Joint Federal Interagency Conference on Sedimentation and Hydrologic Modeling, Reno, NV, USA, pages 19–23, 2015.

[143] Xubin Zeng, Michael Barlage, Robert E Dickinson, Yongjiu Dai, Guiling Wang, and Keith Oleson. Treatment of undercanopy turbulence in land models. J. Clim., 18(23):5086–5094, 2005.

[144] Xubin Zeng, Ming Zhao, and Robert E Dickinson. Intercomparison of bulk aerodynamic algorithms for the computation of sea surface fluxes using TOGA COARE and TAO data. J. Clim., 11(10):2628–2644, 1998.

[145] Jiang Zhu. Implementation and Evaluation of a Tracer Scheme in the River Transport Model. Journal of Climate, in prep.